NORTHWESTERN UNIVERSITY

Theoretical Studies of Adsorption on Reactive Ionic Surfaces

A DISSERTATION

SUBMITTED TO THE GRADUATE SCHOOL

IN PARTIAL FULFULLMENT OF THE REQUIREMENTS

for the degree

DOCTOR OF PHILOSOPHY

Field of Chemistry

By

Xiaoyan Ma

EVANSTON, ILLINOIS

June 2007

ABSTRACT

Theoretical Studies of Adsorption on Reactive Ionic Surfaces

Xiaoyan Ma

Metal oxide surfaces are generally recognized as active substrates for many catalytic reactions. Density Functional Theory (DFT) has been found as a useful computational tool to investigate the geometry, energy, and electronic structure of reactive oxide surfaces and their interaction with small molecules and fragments. In this thesis, primary efforts have been made on studying adsorptions of some adsorbates, such as $CH_3 \cdot$, H_2O and Vanadium, on Hematite, α-Fe_2O_3, (0001) surfaces.

Methyl radical, $CH_3 \cdot$, is a critical molecular fragment among the intermediates often encountered in hydrocarbon reactions. Knowledge of the detailed mechanism of methyl radical interaction with metal oxides will be very helpful in understanding the initial stages of similar reactions of hydrocarbon compounds with metal oxide catalysts. In this study, first principles band structure and embedded-cluster methods are applied to analyze the relevant geometries, energetics, adsorption sites and electronic structure on various Hematite (0001) terminations, finding that the partially oxidized "ferryl structure" has largest adsorption energy, and that regular surface sites can also adsorb methyl radicals. The results obtained from theoretical work then will be discussed in comparison with the experimental results. Although these two approaches produce large discrepancies, the systematic errors in DFT methodology and drawbacks in experimental techniques keep the

window open for future improvements.

The adsorption of H_2O on a Fe-terminated Hematite (0001) surface is the second hematite research topic presented here. Molecular adsorption and dissociative adsorption in monolayer H_2O coverage are considered as the initial stages of interaction. Molecular adsorption is found to have small effects on the underlying surface structure, while dissociative adsorption, especially, heterolytic dissociation, which produces two types of surface hydroxyls, shows a relatively stronger effect. Although the ferryl site has a remarkable affinity to free radicals, it is found to be fairly weak toward H_2O adsorption, and shows little local reactivity enhancement.

The adsorptions of sub-monolayer/monolayer Vanadium on idealized Hematite (0001) surfaces and subsequent oxidation are also studied by DFT. It is found that in most cases, Vanadium forms three-fold bonds with surface O atoms, inducing a large geometry change at the hematite surface and near surface region. The adsorption geometry and energy are mainly decided by interplay between adsorbed metal atom and subsurface metal interaction. V generally functions as an electron donor, causing nearby Fe to be partially reduced; the Fe and V oxidization state depends very much on the coverage and detailed adsorption configuration.

Hydroxyapatite (HAP) is the second reactive ionic surface studied here. The initial stages of the hydration process are simulated on a single-Ca(I) terminated HAP (0001) surface using DFT. Water adsorption configuration and energetic properties are detected at different H_2O coverage. At low H_2O coverage, surface Ca-O_{ad} bonds are found to form, but

as coverage increases, H_2O tends to loosely float on the already-formed water layer. The hydration process does not cause the decomposition of surface phosphate groups and hydroxyl channel, but does affect the energetics of subsequent Zn substitution and occupation on two metal sites. The Ca(II) vacancy site is found to be energetically more favorable for occupation due to less spatial constraint. This suggested mechanism of preferential occupation is different from previous attempts to explain the site preference in bulk by ionic radius and electronegativity differences.

ACKNOWLEDGEMENTS

First of all, I would like to thank Professor Donald E. Ellis for his instruction and encouragement. Don opened the door of theoretical chemistry for me and guided me through the period of Ph.D. research. His continuous contribution to this work through the stimulating discussions not only helped me solve specific problems, but also lead me to learn how to conduct research in general. Without him, this work would have not been finished.

I would like to thank Dr. Bin Deng for helping me at the beginning of my graduate study and life in Northwestern University. As a good friend, he generously shared many valuable experiences with me so that I could have a soft landing in the US and NU. I would like to give my thanks to Zhen Liu, Jianjian Jin, Shuxia Yin, Li Liu, and Ljubomir Miljacic for many academic and interesting conversations, which expedited my research and made my life happier. I am grateful to Mr. Lewis Gebhardt. I enjoyed the tutorial hours we spent each Wednesday afternoon, which extended our topics to many fields. I benefited a lot from these thought-provoking conversations and his help in improving the English of this thesis. My committee members, Professors Stair and Poeppelmeier gave me valuable advice during discussions. Many thanks to them.

I would also like to acknowledge the Department of Energy and Institute of Environmental Catalysis in Northwestern University for financial support.

I am blessed to have a great family. My Mom and Dad always trust me and give me the

ultimate support all the time. Peng, as my husband, accompanied me throughout this period. I would like to give my wholehearted thanks to them and share this unforgettable moment in my life with them.

TABLE OF CONTENTS

CHAPTER 3

ADSORPTION OF OTHER MOLECULES/ATOMS ON HEMATITE SURFACES .. 69

CHAPTER 4

INITIAL STAGES OF HYDRATION AND ZN OCCUPATION ON

HYDROXYAPATITE (0001) SURFACES

LIST OF TABLES

LIST OF FIGURES

–

CHAPTER 1

INTRODUCTION AND BACKGROUND

1.1 Overview of research on metal oxide surfaces

Metal oxides comprise a very important class of compounds, covering many aspects of material science, physics and chemistry [1]. They are widely used in many fields of applications, such as paint pigments, nonlinear optics, sensors, catalysis, etc. [2]. Due to the diversity of properties and characteristics, they can be classified as covalent bonding for one system and ionic for the other; they can act as superconductors on one hand and insulators on the other hand; in some cases, the bulk properties are important, as in nonlinear optics, while in other cases, the surface properties dominate, as in catalysts [3].

The bulk of simple binary metal oxides are pretty well understood for thermodynamics, structure, mechanical properties, and spectroscopy, as well as for electron transport [4-7]. The surface properties of metal oxides as catalysts and adsorbents in environmental remediation [8-10] have also been investigated to study the adsorption and catalytic reactions of trace elements and other relevant pollutants in air or solution [11]. As an interdisciplinary collaboration, surface science studies adsorbate-surface interactions, structure reactivity, reaction mechanisms, as well as molecular level information about surface structure under environmentally relevant conditions, such as temperature, pressure and relative humidity.

However, the physical and chemical properties of metal oxide surfaces are rather poorly ascertained, mostly due to difficulties in preparation of the surfaces and the defects produced accompanying the preparation process. To obtain an ordered surface is not an easy task, and to determine the structure of that ordered surface is even more difficult. This

is because the surface stoichiometry is often different from the bulk, and non-stoichiometric regions, such as defect regions, often inevitably exist on the surfaces, which offers a big challenge, just as noted in Henrich and Cox's book, "the preparation of each separate crystal face of each different compound is a research program in itself" [12].

Despite all these difficulties, the rapid development of surface preparation techniques and structural characterization equipment help people get more insight into metal oxide surfaces and their interactions with small molecules and radicals [13,14]. Some approaches have been developed to obtain clean oxide surfaces inside an UHV chamber [15,16]. One approach is *in situ* cleavage which has been applied successfully to some orientations of MgO, NiO, and $SrTiO_3$ [17] crystals. This approach is more likely to provide surfaces with a close composition to bulk. Another approach is *ex situ* treatment, which combines cutting, polishing, and then *in situ* sputtering and annealing. The latter method has been extensively used in surface science research, but it generates a large amount of defects at the surface region. These defects complicate identification of the surface configurations, but on the other hand, they can increase the conductivity of the sample so that to be utilized by many charge-based surface science techniques [18]. Another common way to obtain an oxide surface is to use metals as substrates to grow oxide films of various thicknesses [19]. One example is NiO (100) growing on a Ni (100) surface [17]. Less strained layers may be grown by choosing inert metal substrates; the oxidation can be performed during or after deposition. If the lattice constants of the inert substrates are chosen properly, the growing oxide structure may exhibit long-range order of high quality. Alloy surfaces can also be oxidized, in which the physical properties of the alloy may be advantageous in some way

for the preparation process. One application is the growing of an α-Al$_2$O$_3$/metal composite by direct oxidation of molten Al-Mg-Si alloy [20]. It proceeds in stages of melting of the alloy ingot, oxidization of the molten alloy surface, rapid growth of the oxide layers, and finally the external surface of α-Al$_2$O$_3$/metal composite is covered by a thin MgO layer.

Surface structural information can be extracted from measurements of many modern methods which probe the topmost 1-10nm of the surfaces exposed to vacuum. These include X-ray Photoelectron Spectroscopy (XPS), Auger Electron Spectroscopy (AES), Low Energy Electron Diffraction (LEED) [21], Reflection High-energy Electron Diffraction (RHEED) [22], Electron Energy Loss Spectroscopy (EELS) [23], Ion Scattering Spectroscopy (ISS) [24], etc. Scanning Tunneling Microscopy (STM) and Atomic Force Microscopy (AFM) studies on oxide surfaces under ultrahigh vacuum (UHV) conditions, yielding atomically resolved information, increase the ability of scientists to measure the physical structure of many surfaces. Under ambient conditions, a series of oxide surfaces have been studied by STM and AFM techniques [25,26]. A particular example that applies UHV-STM technique to reveal the real-space topology of oxide surfaces is reported by Thornton and coworkers [27]. They used STM to study two different reconstructions of α-Fe$_2$O$_3$ (0001) surfaces. It has been known for quite a long time that a sputtered α-Fe$_2$O$_3$ (0001) surface annealed at about 1100K reveals a complex LEED pattern that has been interpreted as multiple scattering across a Fe$_3$O$_4$/FeO/Fe$_2$O$_3$ interface [28-30]. Upon annealing at temperature slightly below this value, the surface appears to stabilize to another structure, namely Fe$_3$O$_4$ (111). The resulted complicated LEED patterns are compared with the bulk phases predicted on the basis of the Fe-O phase diagram; it turns

out that the surface structures are different from the predicted bulk phases [29,30]. This is as expected for many oxide surfaces.

Figure 1.1 copies a diagram from Grassian's *Surface Science Reports* paper, which summarizes the often used surface science techniques [31].
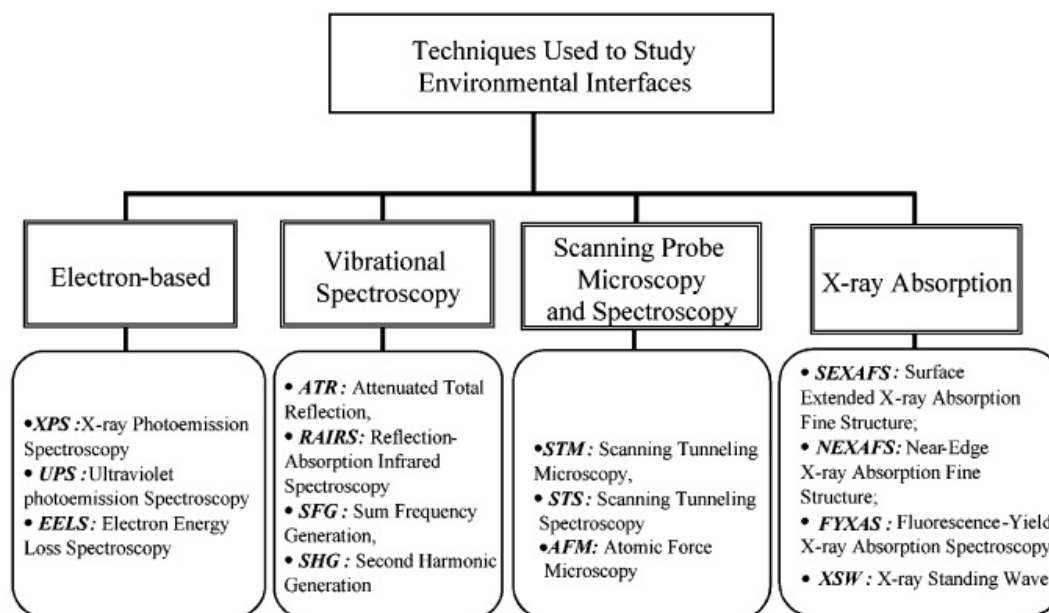
Figure 1.1 A scheme of often used surface techniques in environmental interface studies [31].

Parallel to a large number of experimental investigations on metal oxide surfaces, an increasing number of theoretical explorations of such systems have been published in recent years. The main objective of these studies is to provide detailed information, especially at the molecular level, on the geometric and electronic structure of the surface itself and its interaction with adsorbates, which can be complementary to the results that are obtained experimentally.

The cumulative developments in the methodology of electronic structure calculations and computer technology have popularized computational methods so that they are cheap and reliable as a helpful interpretative tool, even for systems as complex as oxide surfaces. The detailed background will be covered next in this chapter.

1.2 Introduction to Density Functional Theory (DFT)

1.2.1 General background

Research in theoretical chemistry includes the studies of electronic structure, dynamics, statistical mechanics, and mathematical characterization which are invoked to various degrees in the process of solving problems, such as the prediction of chemical reactivity, the study of chemical kinetics and the study of the applicability of recent math developments to the understanding of electronic structure [32]. Computational chemistry is a branch of chemistry that incorporates the results of theoretical chemistry into efficient computer programs to calculate the structures and properties of molecules and solids, and to

provide insight into real chemical problems [33,34]. It uses non-experimental reasoning to explain or predict chemical phenomena, usually with some approximation schemes, such as Hartree-Fock (HF), Density Functional Theory (DFT), semi-empirical methods (e.g., PM3) or force field methods. Some chemical theorists apply statistical mechanics to provide a bridge between the microscopic phenomena of the quantum world and the macroscopic bulk properties of systems [35].

Traditional methods in electronic structure theory, in particular, Hartree-Fock theory and its descendants are based on complicated many-electron wave functions [36,37]. In many-body electronic structure calculations, the nuclei of the treated molecules or clusters are treated as fixed (as in Born-Oppenheimer approximation [38]), generating a static external potential V in which the electrons are moving. A stationary electronic state is then described by a wave function $\psi(\vec{r}_1,...,\vec{r}_N)$ fulfilling the many-electron Schrödinger equation (1),

$$H\psi = [T+V+U]\psi = \left[\sum_i^N -\frac{\hbar^2}{2m}\nabla_i^2 + \sum_i^N V(\vec{r}_i) + \sum_{i<j} U(\vec{r}_i,\vec{r}_j) \right]\psi = E\psi \qquad (1.1)$$

where, H is the electronic molecular Hamiltonian, N is the number of electrons, T and U are so-called universal operators, while V is a system dependent, non-universal operator. U counts electron-electron interaction. There are many sophisticated methods for approximately solving the many-body Schrödinger equation based on the expansion of the wave function in Slater determinants [39]. While the simplest one is the Hartree-Fock method, more sophisticated approaches are usually categorized as post Hartree-Fock

methods. However, the problem with the Hartree-Fock family is the huge computational effort, which makes it virtually impossible to apply them efficiently to more complex systems.

Density Functional Theory (DFT) [40-42] seeks to replace the electronic wave function with the electronic density. Whereas the many-body wave function depends on $3N$ variables, 3 spatial variables for each of N electrons, the density is only a function of three coordinate variables, which is much simpler to deal with, in conceptual and practical point of view.

The predecessor to DFT, the Thomas-Fermi-Dirac model, proposes that the total energy E of an electronic system is a function of electron density $E(\rho)$. So the energy of an atom or molecule can be calculated by representing its kinetic energy, the nuclear-electron and electron-electron interactions as functionals of electron density [43]. This model is rather inaccurate; the largest source of error is in the representation of the kinetic energy, followed by the errors in the exchange energy, and the complete neglect of electron correlation.

Hohenberg and Kohn, in 1964, proposed the Hohenberg-Kohn theorem which states that if N interacting electrons move in an external potential $V_{ext}(r)$, the ground-state electron density minimizes the functional of the total energy, and all other ground state properties of the system (e.g., lattice constants, cohesive energy, etc.) are functionals of the ground state electron density. That is, once the ground state electron density is known, all other ground state properties are all determined [44].

In 1965, W. Kohn and L. Sham [45] proposed the so-called Kohn-Sham equation (2), which is similar in form to the time-independent Schrödinger equation, except that the potential is formally expressed as a functional of electron density (3).

$$\left[-\frac{\hbar^2}{2m}\nabla^2 + V_S(\vec{r}) \right]\phi_i(\vec{r}) = \varepsilon_i\phi_i(\vec{r}) \qquad (1.2)$$

$$V_S = V_{ext} + \int \frac{e^2\rho_S(\vec{r}')}{|\vec{r}-\vec{r}'|}d^3r' + V_{XC}[\rho_S(\vec{r})] \qquad (1.3)$$

The second term in equation (3) describes the electron-electron Coulomb repulsion, while the last term calculates the exchange correlation potential, where V_{XC} includes all the many-particle interactions. Since the Coulomb repulsion and exchange correlation V_{XC} both depend on charge density, $\rho(\vec{r})$, which depends on the wave function ϕ_i, which in turn depends on the potential V_s, the Kohn-Sham equation can be solved in a self-consistent way. Usually one can start with an initial guess for $\rho(\vec{r})$, then calculates the corresponding V_s and solves the Kohn-Sham equations for the ϕ_i. From these one can calculate a new density and start again. This procedure is repeated until convergence is reached.

Unfortunately, for a system more complex than free electron gas, the exchange-correlation potential is generally unknown. However, some approximations are capable of performing the calculation of certain properties quite accurately. One of the most widely used approximations is the local density approximation (LDA) [45], where the functional depends only on the density at the coordinate where the functional is evaluated (4),

$$E_{XC}[\rho] = \int \varepsilon_{XC}(\rho)d^3r \qquad (1.4)$$

The Local Spin Density Approximation (LDSA) was developed to include electron spin in LDA in the early seventies [46,47], and shortly thereafter relativistic corrections were introduced [48] into the formalism. In the spin-polarized Kohn-Sham scheme with LSDA, the exchange- correlation energy is written as,

$$E_{XC}[\rho_\uparrow, \rho_\downarrow] = \int \varepsilon_{XC}(\rho_\uparrow, \rho_\downarrow)d^3r \qquad (1.5)$$

Another widely used approximation is the Generalized Gradient Approximation (GGA), defined in the early and mid eighties [49-51]. This approximation is still local, but takes into account the gradient of the density at the same coordinate,

$$E_{XC}[\rho_\uparrow, \rho_\downarrow] = \int \varepsilon_{XC}(\rho_\uparrow, \rho_\downarrow, \vec{\nabla}\rho_\uparrow, \vec{\nabla}\rho_\downarrow)d^3r \qquad (1.6)$$

Using GGA, very good results for molecular geometries and ground state energies have been achieved. Many further improvements have been incorporated into the DFT framework by developing better representation of functionals including hybrid exchange-correlation functionals [52], self interaction correction [53], meta-generalized gradient approximation (meta-GGA) [54], DFT+U approximation [55], etc. In solid state calculations, LDA and GGA are commonly used along with plane wave basis sets [56,57]. In molecular calculations, more sophisticated functionals, such as hybrid B3LYP [58] have

been developed. However, although DFT has been found usually sufficiently accurate for many applications, there are some drawbacks remaining in this method. It formally only calculates ground state properties; it results in very poor cohesive energy, usually too high; it performs badly in weak interactions, such as Van-der-Waals interaction; it is unstable in treating negative ions; and there is no systematic way of improving it [59,60]. Hence in the current DFT approach, it is impossible to estimate error of the calculations without comparing them to other methods or experiments.

The methodologies that explicitly describe the geometric and electronic structure which are used in this investigation of oxide surfaces can be categorized into two groups. One group contains periodic slab band structure calculations, that is, methods taking care of the infinite periodic structure of a single crystal or a single crystal surface. The actual dimension of such a calculation depends only on the size of the unit cell, due to the incorporation of the periodicity of the crystal lattice. The alternative method used is cluster calculations, in which a finite cluster of atoms or ions is treated explicitly. The cluster can be further embedded in an external field in order to simulate interactions with the rest of the crystal or film. Cluster approach is particularly suitable when the local effects, such as adsorption, defects and so on are especially of interest. It is obvious that the quality of the results of a cluster description depends on the size, the localizability and the nature of the chemical bonds in the crystal.

1.2.2 Periodic slab band structure calculation tool

The periodic plane wave band structure tool Vienna *ab initio* Simulation Package (VASP) and the ultrasoft pseudopotential database contained therein [56,57] are largely applied in all the projects. They are used to relax surface geometry, calculate ground state energies and analyze electronic structure, such as Density of States (DOS).

Vienna *ab initio* Simulation Package (VASP) [61] is a complex package for performing *ab initio* quantum-mechanical molecular dynamics (MD) simulations using pseudopotentials or the projector-augmented wave method and a plane wave basis set.

The approach implemented in VASP is based on the finite-temperature local-density approximation, with the free energy as variational quantity and an exact evaluation of the instantaneous electronic ground state at each MD time step. VASP uses efficient matrix diagonalisation schemes and an efficient Pulay/Broyden charge density mixing. The interaction between ions and electrons is described by ultra-soft Vanderbilt pseudopotentials [62] or by the projector-augmented wave (PAW) method [56,57]. These pseudopotentials allow a smaller basis set for a given accuracy. The residual minimization technique [57] is used to calculate the electronic ground state. The relaxation of different atomic configurations is based on conjugate-gradient (CG) minimization [63] of the total energy.

1.2.3 Embedded cluster calculation tool

As a complementary tool to VASP, the first principles local-density self-consistent-field (SCF) embedded–cluster method is extensively used appling the SCF local-density theory in a molecular-orbital (MO) framework to describe electronic properties of solids [64,65].

The linear combination of atomic orbitals (LCAO) method and discrete variational method (DVM) with a numerical integration scheme is used in this thesis, with atomic radial basis functions generated as numerical solutions of atoms/ions in a potential well represented by values tabulated on net points. The effective atomic configurations of the cluster atoms are obtained self-consistently by iterating the charge and spin density, using the *VWN* exchange and correlation potential [66] and a least-squares fit of model parameters to the eigenvector densities [65]. As to the embedding model, the charge density ρ, which determines both Coulomb potential and the approximate exchange-correlation potential V_{XC}, includes contributions from the embedding lattice as well as the variational cluster [65]. Thus, the total Coulomb potential can be written as $V_C^{tot} = V_C^{cluster} + V_C^{emb}$, where V_C^{emb} is the Coulomb potential contributed by the assumed charge distribution of embedding lattice calculated by Ewald summation [67].

Electronic structure, bonding information and charge density can be extracted from cluster calculations to get more details of clean surfaces and its interaction with adsorbates. Mulliken charge and population are examined; graphs of local density of states (LDOS) are plotted. LDOS is obtained by broadening discrete cluster energy levels into Lorentzian lines, that is,

$$D_j(E) = \sum_i f_{ij} L(E - \varepsilon_i, \gamma)$$ (1.7)

Here, f_{ij} is the weight determined by Mulliken population analysis of atomic orbital j on a selected site in the energy level ε_i, and γ is the width of the Lorentzian function.

In the bonding analysis, bond order (*BO*) [68], which evaluates the degree of shared charge between atoms is calculated. This is defined as the summation of overlap populations between atoms μ and v,

$$BO_{u,v} = \sum_{i \in \mu, j \in v} S_{ij} \sum_k n_k C_{ik} C_{jk}$$ (1.8)

Charge density contours are also plotted to present distribution of charge among atoms. The bond critical point (ρ_c) [69], which is the value of density along the interatomic lines where the gradient of the charge density $\nabla\rho = 0$, helps to define a 'topological atom', and reflects the covalency at the interatomic surface.

1.3 Development in iron oxide surface studies

Iron is the most abundant element in the earth's crust following oxygen and silicon. Iron oxides [70] exist as various different polymorphs, including FeO, Fe_3O_4, Fe_2O_3, etc. Hematite (α-Fe_2O_3) and magnetite (Fe_3O_4) are the most common and stable phases of iron oxides. The structure of Hematite is the same as corundum, whereas magnetite possesses an

inverse spinel, $Fe^{3+}(Fe^{2+}Fe^{3+})O_4$, structure. Other iron oxide phases include maghemite (γ -Fe_2O_3), a meta-stable phase nearly iso-structural with Fe_3O_4, and wustite (FeO), which has the rock salt structure and is not stable at temperatures below 843 K [71].

As the most intensively studied oxide surface in this dissertation, Hematite crystals (α-Fe_2O_3) do not readily cleave and its (0001) and the ($10\bar{1}1$) basal planes are the predominant naturally grown faces [12]. Surface reconstruction of Hematite to Fe_3O_4 and FeO has been observed at annealing temperatures lower than 1173 K. The (1x1) LEED pattern characteristic of α-Fe_2O_3 (0001) is observed after prolonged annealing at 1173 K or above. Different preparation methods and characterization of the α-Fe_2O_3 (0001) surface are described in the literature [72-75]. Weiss and coworkers investigated the dependence of α-Fe_2O_3 (0001) surface structure on ambient oxygen gas pressure with STM and LEED and presented a procedure to epitaxially grow controllable iron oxide model catalyst films [3]. α-Fe_2O_3 (0001) can be transformed from pre-oxidized Fe_3O_4(111) films by a high-pressure oxidation treatment in 1 mbar oxygen at 1100 K for about 10 min. A hexagonal LEED pattern appeared after the sputtered surface is annealed in vacuum at 900℃ for 30 minutes by electron beam heating. Studies on either the α-Fe_2O_3 (0001) mineral single crystals [76] or the thin epitaxially grown film sample [77] confirm the formation of magnetite, Fe_3O_4, (111) selvedge on top of the hematite bulk crystal. A "floret" LEED pattern is observed if the sputtered sample is annealed under 1-5 x10^{-6} torr O_2 pressure at 900℃ for 30 minutes. STM studies [78] show an ordered super-lattice structure, which is composed of FeO (111) and α-Fe_2O_3 (0001) islands. This surface is then called the "biphase" surface [73].

The defect sites on α-Fe$_2$O$_3$ (0001) surfaces can be created during bombardment process [79,80]. The electronic structure of defective α-Fe$_2$O$_3$ (0001) surface has been extensively investigated using UPS, XPS and Auger spectroscopy [79]. The resulting spectra indicate that the ion-bombarded surface is O deficient relative to the stoichiometric α-Fe$_2$O$_3$ (0001) surface with contributions from reduced cations, mainly Fe^{2+} and metallic Fe^0. In addition, irradiation of α-Fe$_2$O$_3$ (0001) with UV photons having energies greater than the band gap of α-Fe$_2$O$_3$ (0001), which is 2.2 eV, results in the formation of electron–hole pairs that create transient Fe^{2+} cations [80]. These defect sites turn the inert stoichiometric α-Fe$_2$O$_3$ (0001) surface into a reactive catalyst material and an adsorbent toward gases such as H$_2$O, styrene, ethylbenzene, SO$_2$, CCl$_4$, CO, etc. [81-85].

Some theoretical works have been conducted on iron oxide bulk and surfaces which used *ab initio* approaches to calculate the surface relaxation, binding energies, magnetic properties and electronic structure [86-88]. Wang [87] et al., used DFT results to explain the experimental observation that a Hematite (0001) surface with a permanent dipole moment along the surface normal direction could be obtained on a thin film sample. They found that electron redistribution and strong relaxation greatly increase the covalent character of the Fe-O bonds and lead to the stabilization of the surface. Rohrbach [86] et al., introduced the usage of the GGA+U approach for better treatment of strong d-d interaction of Fe in the hematite crystal. There are some other reports on the adsorption properties of Hematite (0001) surfaces toward air pollutants and wastes [89,90].

1.4 Introduction to Hydroxyapatite research

Hydroxyapatite (HAP) is one of a few minerals that can be classified as bioactive materials. It is known under the chemical formula of $Ca_{10}(PO_4)_6(OH)_2$, and is widely used in the repair, reconstruction, and replacement of diseased or damaged parts of the bones or teeth [91-94]. It also claims attention as an environmental adsorbent of metals and waste removal due to its porous nature and excellent ion exchange character [95,96]. It has been shown from both experiments and theoretical calculations that the (0001) surface of HAP is the dominant interface with respect to vacuum and aqueous phases [97]. Because the surface of HAP is of great importance for understanding of dissolution [98] and interfacial interactions [99] between the crystal and ambient phases, some efforts have been made to investigate the relevant surface properties. In experiments, multiple studies have been carried out by using several characterization techniques [100] to identify the HAP biocompatibility [101], adhesion properties [92] and synthetic conditions [102]. Meanwhile, computational methodology has shown its strength in interpreting electronic structure, charge distribution and atomic configuration by quantum mechanics [103-105], semi-empirical [106] and density functional theory [107].

Wu and his co-workers studied surface energetics of HAP by the DFT approach, finding that the relaxation of the slab surfaces has an apparent effect on surface energy, and they also proposed the relative order of the morphological importance of different (*hkl*) surfaces [108]. Zahn and coworker investigated energetic preference of HAP with substitutional defects in order/disorder arrangement of OH⁻ ions, concluding that HO⁻…HO⁻ arrangement is most favorable [109]. De Leeuw drew the similar conclusion using DFT [110]. There are some other theoretical papers reporting the studies about defects, structures, and

adsorptions on HAP surfaces or near-surface [111,112]. In a recent work of Zahn et al., molecular dynamics approaches were applied to study the hydration of (0001) HAP interfaces [113]. They found that water can form strong electrostatic interactions with the calcium and the phosphate ions of the crystal surface. But so far, no DFT first principles work has been done in this aspect.

1.5 The objective and outline of the thesis

The objective of this research is to use DFT approaches to study the properties of reactive ionic surfaces, especially iron oxide and Hydroxyapatite surfaces with and without adsorbates, such as $CH_3 \cdot$, H_2O, CH_3OH, V, etc. The following topics will be discussed through this research presentation:

Method credibility and feasibility: This research will compare the theoretical results obtained from DFT practices with the relevant experiments. The systematic errors in theoretical methodology and drawbacks in experimental techniques will then be commented upon.

Surface stability: One of vital questions in surface science study is the relative stability of various surfaces. The ionic surfaces involved in this research are complex and may exhibit different terminations in theoretical modeling. Excluding those less stable surfaces will help set up future simulations which are of more practical meaning.

Adsorption and surface interaction: The preferential adsorption sites will be found through

comparison of energies on defective and regular surface sites. Surface geometrical, energetic, and electronic information will be extracted from calculation results. They can provide insights into the chemistry behind the interactions.

Substitution and occupation: Zn substitution and occupation on metal ion sites of Hydroxyapatite will be studied to investigate the material's ion exchange property.

The reactive ionic surfaces studied in this research are:

- Iron oxide surfaces: α-Fe_2O_3 (0001), Fe_3O_4 (111), and FeO (111).

- Hydroxyapatite (0001).

The following adsorbates are considered: $CH_3\cdot$, H_2O, and $HO\cdot$ on iron oxide surfaces; Zn^{2+} ion on HAP surfaces.

This dissertation includes 4 chapters. Chapter 1 briefly describes experimental and theoretical background in the fields of metal oxide surface research, especially on iron oxide and Hydroxyapatite surfaces which are the focus in this thesis; Chapter 2 analyzes the DFT studies of adsorption of $CH_3\cdot$ on the iron oxide surfaces, compared with the related experimental work; Chapter 3 presents two additional studies of adsorption on α-Fe_2O_3 (0001) surfaces, the first one is initial stages of H_2O adsorption, in collaboration with Shuxia Yin, the second is V atom adsorption and oxidation, in collaboration with Jianjian Jin; Chapter 4 presents the DFT work in the hydration and subsequent substitution and occupation of Zn^{2+} on HAP (0001) surfaces.

CHAPTER 2

THEORETICAL STUDIES OF METHYL RADICAL

ADSORPTION ON IRON OXIDE SURFACES

2.1 Introduction

Methyl radical (CH$_3$·) is among the intermediates frequently encountered in hydrocarbon reactions [1,2]. It is also known to be present as an intermediate during metal, semiconductor and diamond film growth by chemical vapor deposition of the corresponding alkyls [3,4]. By knowing the detailed mechanism of methyl radical interaction with metal oxides, people may very possibly be able to understand the initial stages of similar reactions of hydrocarbon compounds with metal oxide catalysts.

The Lunsford group has done a lot of experimental work on the interaction of CH$_3$· with metal oxides [5-9]. One study investigated the conversion of methyl radicals to methanol and formaldehyde over vanadium oxide catalysts [10]. They found that the interaction involved the formation of methoxide ions and the reduction of V^{5+} to V^{4+}. Since Vanadium oxide has the same corundum type structure as Hematite, this mechanism could be a very relevant comparison.

Theoretically, there have been several first principles investigations of methyl interaction with various transition metal surfaces such as Ni (111) [11] or Rh (111) [12] and metal oxide surfaces such as MgO (100) [13] or NiO(100) [14]. It is predicted, using the Hartree-Fock (HF) methodology, that methyl binds very weakly with NiO (100) and MgO (100) surfaces, which is within expectations that perfect MgO (100) surfaces may have very low reactivity. However, it is somewhat surprising that HF predicts NiO (100) cannot form strong bonding with methyl, especially after CH$_3$· is experimentally observed to adsorb onto NiO (100) surfaces [6]. A possible explanation is the underbinding trend of HF

predictions; such conjecture is further corroborated by recent studies of CO and NO adsorption on NiO (100) and $Ni_xMg_{1-x}O(100)$ surfaces which conclude that HF cluster calculations indeed underestimate the adsorption energy of small molecules on metal oxide surfaces by a magnitude of 0.3~0.4 eV [15]. On the other hand, due to incomplete description of strong 3d electron localization effects, density functional theory (DFT) has been found to overestimate the binding energy between small molecules and transition metal surfaces [15-19]. Hence, using DFT to study molecular adsorption on transition metal surfaces should be carried out with great caution and must be carefully compared with corresponding experimental results. Recently, some attempts to improve DFT treatment of correlation have been made, such as the DFT+U method, and schemes which empirically mix HF and DFT exchange and correlation functionals (e.g., B3LYP, [17,18]). However, these newer approaches are not yet well "calibrated", so they must be compared with experimental results or other computational methods for reference.

This chapter will focus on the theoretical study of adsorption of methyl radical on various terminations of Hematite (0001) surfaces. Both first principles band structure and embedded cluster methods are used to find the relevant geometries, energetics, adsorption sites, and electronic structure on the atomic scale. A parallel experiment was carried out by Li Liu [20,32]. A comparison between theoretical and experimental results will be made, and the methyl adsorption on FeO (111) and Fe_3O_4 (111) surfaces will also be included as references.

2.2 Settings in periodic slab band structure program

The band structure calculations were performed using the first principles DFT Program VASP (Vienna *ab initio* simulation package). The program background can be found in Chapter 1.2.2. The exchange-correlation potential is chosen as the spin-polarized generalized gradient approximation (SP-GGA) in a scheme developed by Perdew *et al.* (PBE) [21,22]. For each of the simple (1x1) iron oxide surfaces, a 4x4x1 k-points mesh is used for geometrical relaxation and energy calculations. In geometrical relaxation, a Gaussian smearing finite temperature broadening method [23] is used with width $\sigma=0.1$eV. For energy calculations, the tetrahedron method is used to perform Brillouin zone sampling [24]. The energy convergence criterion for relaxation is 10^{-3} eV per unit cell. A plane wave basis set is used with energy cutoff 400eV, which has been found to be sufficient to obtain quantitative precision (better than 0.01eV/cell) for iron oxide bulks and surfaces. The vacuum gap thickness between periodic slabs is set to be ~10Å. Computational tests show that increasing the vacuum gap to ~15Å changes energy by less than 1 meV/atom for the clean surface reference system. The number of atomic layers along the z-axis of the clean slabs is kept in the range of 8 to 10, considered to be a good balance between computational cost and accuracy. In modeling $CH_3\cdot$ adsorption, all substrate layers except the top 2 to 3 are fixed to the atomic coordinates obtained in the clean surface relaxation. This simplified partially rigid treatment proves to adequately reproduce the same relaxation structure as a fully relaxed slab. For example, in a model in which up to 5 substrate layers are relaxed, the effect of adsorption on the substrate 2 layers below the surface is quite small (z-direction displacement difference is only about 0.01Å). The corresponding adsorption energy

difference is only about 2meV/atom. So the models and parameter settings are of acceptable precision to describe this $CH_3 \bullet$ adsorption case. Another concern about numerical precision arises from the long-range electrostatic fields associated with the periodic slab model of ions. This can be partially compensated within VASP using the so-called dipole correction scheme [25]. The test of implementing dipole correction finds that it has negligible effects on geometry and adsorption energy in the systems studied here.

Although there are many different terminations available on iron oxide surfaces, this dissertation focuses only on a few important examples. Four types of adsorption cases are chosen for representing different Fe_3O_4 (111) terminations, three for α-Fe_2O_3 (0001) terminations, and one for FeO (111) termination. Table 2.1 lists the eight cases.

Table 2.1 List of all studied adsorption cases

	Termination	Site
Fe_3O_4 (111)	¾ Fe_{oct} + ¼ O	O
	¼ Fe_{oct} + ¼ Fe_{tet}	Fe_{oct}
	¼ Fe_{tet} + ¼ Fe_{oct}	Fe_{tet}
	¼ Fe_{tet}	Fe_{tet}
α-Fe_2O_3 (0001)	Fe-	M.L.
	O-	M.L.
	"Ferryl" (O=Fe-)	M.L.
FeO (111)	Fe-	Fe

Note: M.L.=multiple location.

According to the following notations, ¾ or ¼ means 3 or 1 atom(s) on a 1x1 Fe_3O_4 (111) unit cell. Since Fe atoms occupy both octahedral and tetrahedral sites, "oct" and "tet" are also indicated with a subscript following the "Fe" element.

Here, ¾ Fe_{oct} + ¼ O termination on Fe_3O_4 (111) is the one plotted in Figure 2.1a; ¼ Fe_{oct} +

¼ Fe_{tet} termination on Fe_3O_4 (111) is described in Figures 2.1b and c, where 2.1b is on-top

Fe_{oct} adsorption and 2.1c is on-top Fe_{tet} adsorption; Figure 2.1d is for ¼ Fe_{tet} termination.

a

b

c

d

e
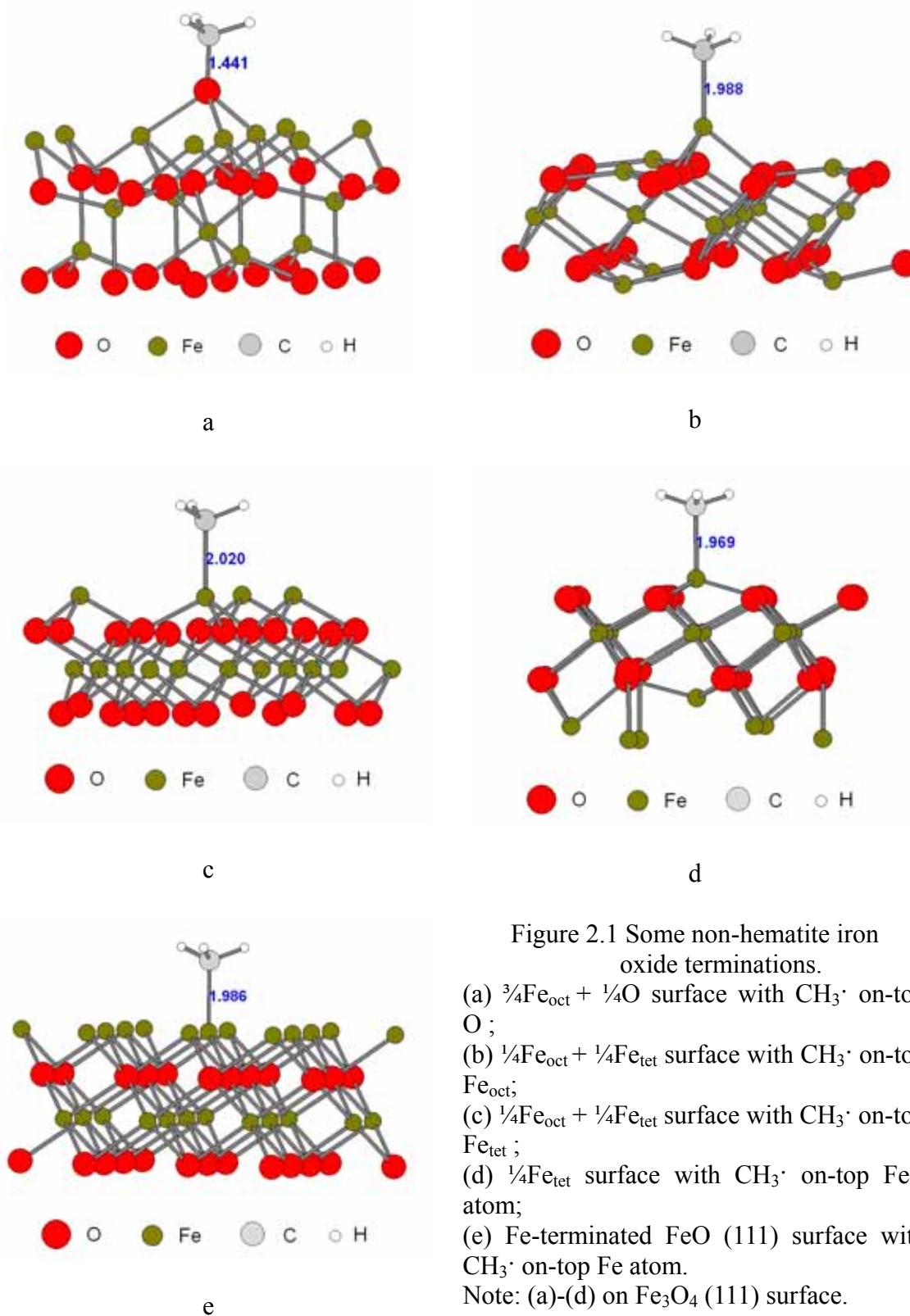
Figure 2.1 Some non-hematite iron oxide terminations.

(a) $\frac{3}{4}Fe_{oct} + \frac{1}{4}O$ surface with $CH_3\cdot$ on-top O ;

(b) $\frac{1}{4}Fe_{oct} + \frac{1}{4}Fe_{tet}$ surface with $CH_3\cdot$ on-top Fe_{oct};

(c) $\frac{1}{4}Fe_{oct} + \frac{1}{4}Fe_{tet}$ surface with $CH_3\cdot$ on-top Fe_{tet} ;

(d) $\frac{1}{4}Fe_{tet}$ surface with $CH_3\cdot$ on-top Fe_{tet} atom;

(e) Fe-terminated FeO (111) surface with $CH_3\cdot$ on-top Fe atom.

Note: (a)-(d) on Fe_3O_4 (111) surface.

Among the other 4 surfaces listed in Table 2.1, Fe-terminated α-Fe$_2$O$_3$ (0001) refers to an ideal Fe-terminated surface; O-termination refers to an ideal oxygen-terminated surface; O=Fe-termination represents a partially oxidized Fe-terminated surface that will also be called 'ferryl' structure [26] and Fe-termination on FeO (111) is the second component of the α-Fe$_2$O$_3$ (0001) and FeO "biphase" structure (Figure 2.1e) [27].

2.3 Settings in cluster calculation program

Using final relaxed geometries resulting from the periodic slab band structure models, cluster computations are carried out to get charge density, local densities of states (LDOS), Mulliken populations, charge and bonding order (BO) (see Chapter 1.2.3 for mathematical formula). A typical small cluster, for Fe-terminated α-Fe$_2$O$_3$ (0001) with CH$_3$· sitting at the on-top site, consists of 29 atoms (Figure 2.2a, 11 Fe atoms and 18 O atoms) in the substrate and the CH$_3$· adsorbate. Within this model, the methyl group is rigidly shifted along the z-axis, mapping out a rough approximation of the binding energy curve for a frozen substrate. This procedure allows for a clean interpretation of bonding around the VASP determined minimum-energy configuration, by comparing energies of closer and more distant adsorbate positions. The effects of embedding on the binding energy curves are found to be dominated by the long-rang interactions, while the local (interior of cluster) bonding structures and electron density are essentially unaffected. Since the binding energy with relaxed substrate is definitively determined in the VASP calculations, the embedding is not necessary to be included in the final cluster models.
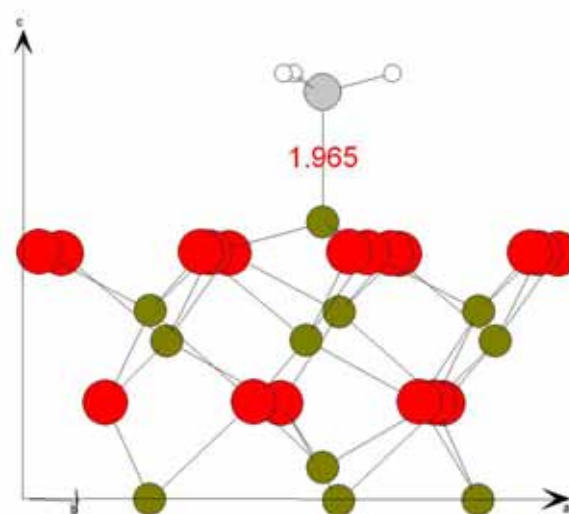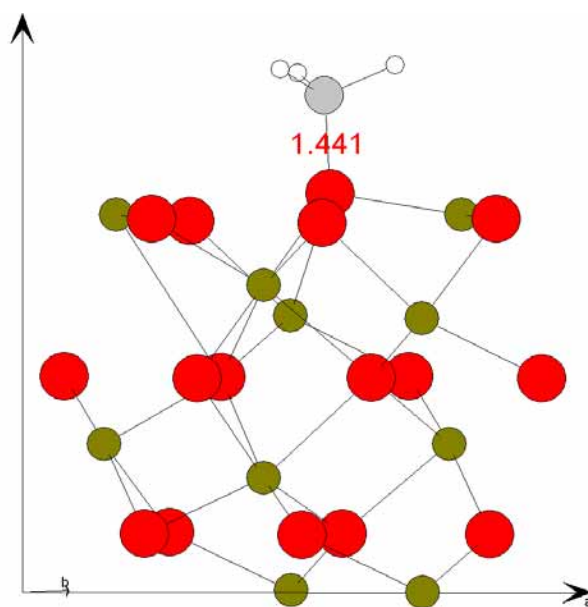
Figure 2.2 CH₃· adsorption on Fe-terminated Hematite (0001) surface.

(a) on-top Fe atom; (b) on-top second layer O atom.

2.4 Relaxed geometry and adsorption energy

2.4.1 Bulk Hematite

A Fe-terminated Hematite along the (0001) direction shows a Fe_A-O3-Fe_B-Fe_A-O3…
periodic arrangement (Figure 2.3). Much theoretical work has been done on bulk and
surface α-Fe_2O_3 [26,28]. As the first step of this work, optimized lattice constants from this
computational setup are compared with previous theoretical results and experiments.
Within the spin-dependent DFT methodology described above, an initial anti-ferromagnetic
spin distribution of iron, in which the iron pairs in -O3-Fe_B-Fe_A-O3- have the same spin
direction while neighboring -Fe_A-O3-Fe_B- pairs have opposite spin direction, is assumed.
This is the ground state magnetization distribution suggested by previous experimental and
theoretical works. Compared with experiment [29], the calculations of Wang et al. [28],
Wolfgang et al. [30], and Rohrbach et al. [26], this work achieves within 1% of the
experimental lattice constants, and highly satisfactory atomic coordinates within the unit
cell, which indicates a stable and accurate plane wave methodology. Therefore, all the
following surface-slab calculations are based on the lattice constants which are obtained in
this initial study.
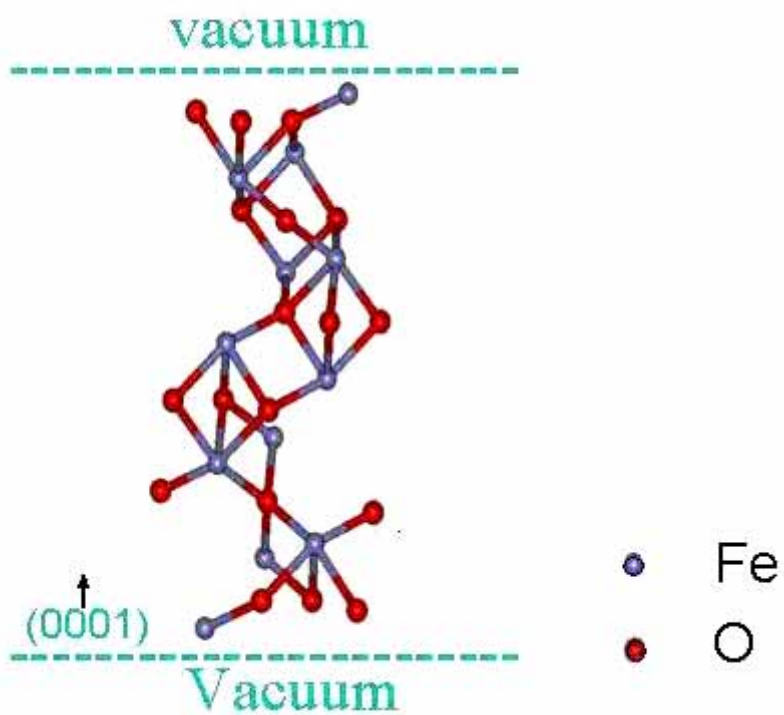
Figure 2.3 18-layer Fe-terminated α-Fe$_2$O$_3$ (0001) surface structure (side view).

2.4.2 Relaxation of clean surface

Iron oxides encounter large scale surface relaxation when their surfaces are exposed to the air. This has been proved by other works [30]. As the second step of the simulation, surface relaxation on iron oxides, especially on the α-Fe_2O_3 (0001) surface, has been meticulously calculated as a subsidiary checkpoint to test the feasibility of the DFT method applied in this research.

The relaxation of three different α-Fe_2O_3 (0001) terminations is checked.

For the clean Fe-terminated surface, the model of top-layered Fe_S (s: surface atom) occupying the corresponding Fe position in bulk hematite is probed, which is found to be the most stable location for Fe according to Wolfgang et al. [30]. A strong relaxation compared to bulk hematite, especially for the first Fe_S layer and the second oxygen layer, is found in this case.

For the O3-terminated surface, a fully oxidized Hematite surface that has 3 oxygen atoms as the top layer is probed. The result shows that the C_3 symmetry is well maintained except that the top oxygen atoms rotate about 5 degrees around the z-axis. Although there is minor relaxation for the distance between the first (O) layer and the second Fe_B layer, there is much stronger relaxation between the second Fe_B layer and the third Fe_A layer so that the two Fe layers below the top oxygen layer become almost flattened into a single layer. The O2-terminated O-vacancy surface no longer reflects C_3 symmetry. Similar to the O3-terminated surface, there is a strong relaxation of the outermost Fe_B-Fe_A double layer.

Finally the O=Fe-terminated structure which represents a partially oxidized Fe-termination surface, the so called "ferryl structure" [26], is relaxed. The O=Fe- bond is vertical to the surface, and the bond length for the clean surface is about 1.6Å. Although the subsequent relaxation between top O=Fe-O3 layers is much smaller compared with that of the Fe-terminated surface, the Fe_B-Fe_A double layer contraction is still very noticeable. In a previous theoretical study [26,30], this ferryl structure was found to be possibly meta-stable within an O-rich environment.

Table 2.2 compares the relaxation results of various terminations on α-Fe$_2$O$_3$ (0001) surface done in this work with other works [30]. It is clear that the thinner slab models in this study are in semi-quantitative agreement with the relaxation results obtained by thicker slabs and highly precise methods, so they are reliable to be used for the following CH$_3\cdot$ adsorption studies.

Table 2.2 Surface relaxation results on clean α-Fe$_2$O$_3$ (0001) surfaces

	Fe_S-O3- (%)	O-Fe_B- (%)	Fe_B-Fe_A- (%)	Fe_A-O3- (%)	O3-$Fe_{B'}$- (%)
Fe- [a]	-51.3	6.4	-31.7	13.1	
Fe- [b]	-59.4	5.8	-46.0	9.7	
O3- [a]		-4.9	-78.4	34.7	-7.1
O3- [b]		-5.8	-73.0	30.6	4.5
O2- [a]		4.9	-56.3	14.6	3.5
O2- [b]		9.6	-58.3	11.4	15.6
O=Fe- [b]	-19.1	1.5	-33.7	13.3	

Note: (a) [30]; (b) This work.

2.4.3 CH$_3$· preferential adsorption on Hematite (0001) surface

2.4.3.1 Fe-terminated surface

Two adsorption cases are investigated:

(1) Directly adsorbed on top of a terminal Fe atom (Figure 2.2a);

(2) Adsorbed on top of an O atom on the second, partially exposed layer (Figure 2.2b).

In the first case, the C_3 symmetry of CH$_3$· is well maintained after geometric relaxation with $\theta_{H\text{-}C\text{-}H}$ about 113˚, larger than 109° in a tetrahedral methane structure, and $\theta_{Fe\text{-}C\text{-}H}$ about 105˚. The equilibrium bonding distance R$_{C\text{-}Fe}$ is about 1.97Å. The presence of CH$_3$· enlarges the first interlayer distance by only 0.12Å and has negligible effects on the deeper layers. The PBE-GGA functional predicts strong exothermic adsorption energy of -2.3eV.

In the second case, CH$_3$· stands vertically on top of one of the three-fold oxygen atoms belonging to the second atomic layer. Though both Fe and O compete to interact with C, after the geometric optimization, it turns out that C stably adsorbs on O which is thus pulled out of the second layer and finally stays almost as high as the topmost Fe atom. This rearrangement of the structure decreases the repulsion between positively charged H and Fe. The equilibrium C-O bonding distance is found to be 1.44 Å, and the C-O bond tilts from the surface normal by 4.6˚ for 1ML adsorption. This tilt might further lower Coulomb repulsion between H and surface Fe atoms. Since it is energetically costly to attract the O atom upward, the net adsorption energy is 0.5eV lower than that in the on-top Fe case. A

summary is given in Table 2.3.

2.4.3.2 O3-terminated surface

For the O3-terminated surface, there are three possible adsorption cases:

(1) Directly adsorbed on top of O atom (Figure 2.4a);

(2) Adsorbed on the O-O bridge site (Figures 2.4b and c);

(3) Adsorbed on the three-fold hollow site.

Figure 2.4a shows that $CH_3\cdot$ binds with the O atom, with C-O bond length of 1.42 Å; the bond axis is perpendicular to the surface. The PBE-GGA calculates adsorption energy to be -3.2 eV. In addition to a stronger C-O bonding, compared to the previously described $CH_3\cdot$–Fe adsorption case, the $\theta_{O\text{-}C\text{-}H}$ and $\theta_{H\text{-}C\text{-}H}$ angles are closer to tetrahedral values.

If the initial position of $CH_3\cdot$ is on top of the O-O bridge (the mid-point of two neighboring O atoms), the adsorbate fails to form a symmetrical status with both O atoms. For different starting position trials, local relaxation calculations suggest that $CH_3\cdot$ will either evolve to bind with one of the neighboring O atoms (Figure 2.4b) with tilting angle of 14° and adsorption energy of -3.0 eV, or dehydrogenate when one of the H atoms comes close enough to interact with surface O, as described in the reaction of $CH_3\cdot + 2O^{2-} \rightarrow CH_2O^- + OH^{\cdot-}$. In the dehydrogenation scenario (Figure 2.4c), the adsorption energy is -2.6 eV, for energy gain of forming an O-H bond is much higher than the cost of breaking a C-H bond.
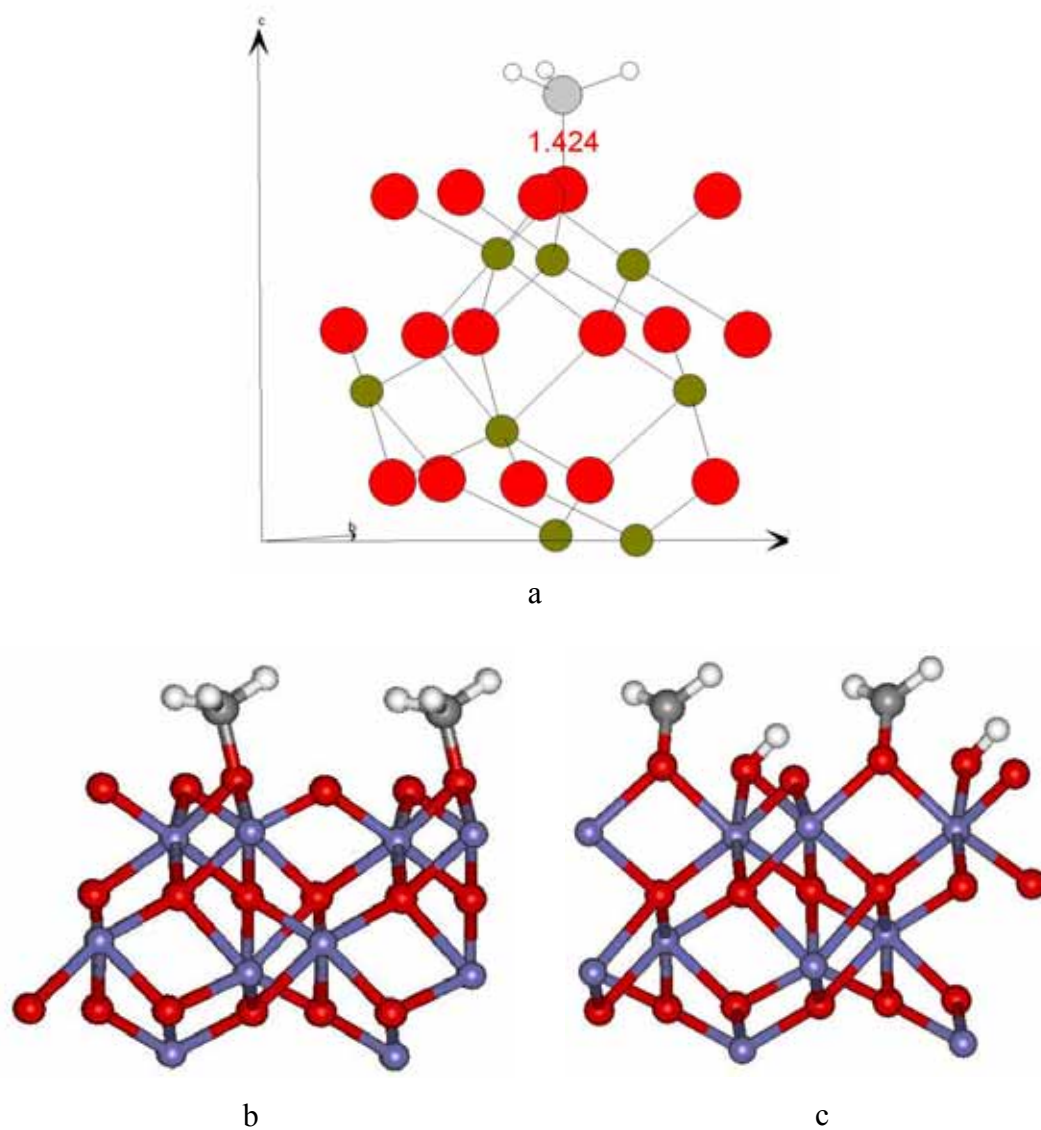
Figure 2.4 CH$_3\cdot$ adsorption on O3-terminated Hematite (0001) surface.

(a) on-top O atom; (b) on O-O bridge site (non-dissociative); (c) on O-O bridge site (dissociated).

It is worthwhile to remember that the organic molecule dehydrogenation process has been proved to be a crucial step in the whole catalysis sequence [31]. This calculation shows that such dehydrogenation is favored when methyl drops close enough to an O-O bridge. Since these sites are not energetically most favorable adsorption sites, increasing molecular kinetic energy or creating defects on the surface is important to increase the probability for such a dissociation process.

The calculation also indicates that when $CH_3\cdot$ is introduced to the three-fold hollow sites on the O3- surface plane, it fails to adsorb. It could be because the highly symmetrical C_3 structure makes it difficult for $CH_3\cdot$ to dehydrogenate twice to generate 2 Hydrogen radicals, binding with the other two surface O atoms. A summary can be found at Table 2.3.

2.4.3.3 O2- terminated surface

The oxygen-vacancy O2-terminated surface can represent a hematite substrate system at low O_2 pressure and elevated temperature. The predicted on-top O adsorption geometry is similar to the O3- case, not showing any tendency to interact with the vacancy. However, when $CH_3\cdot$ is placed on the top of a second layer Fe atom, a C-Fe bond formed (Figure 2.5a). The adsorption energy is -1.7 eV and the Fe-C tilting angle is 30˚. A summary is given in Table 2.3.
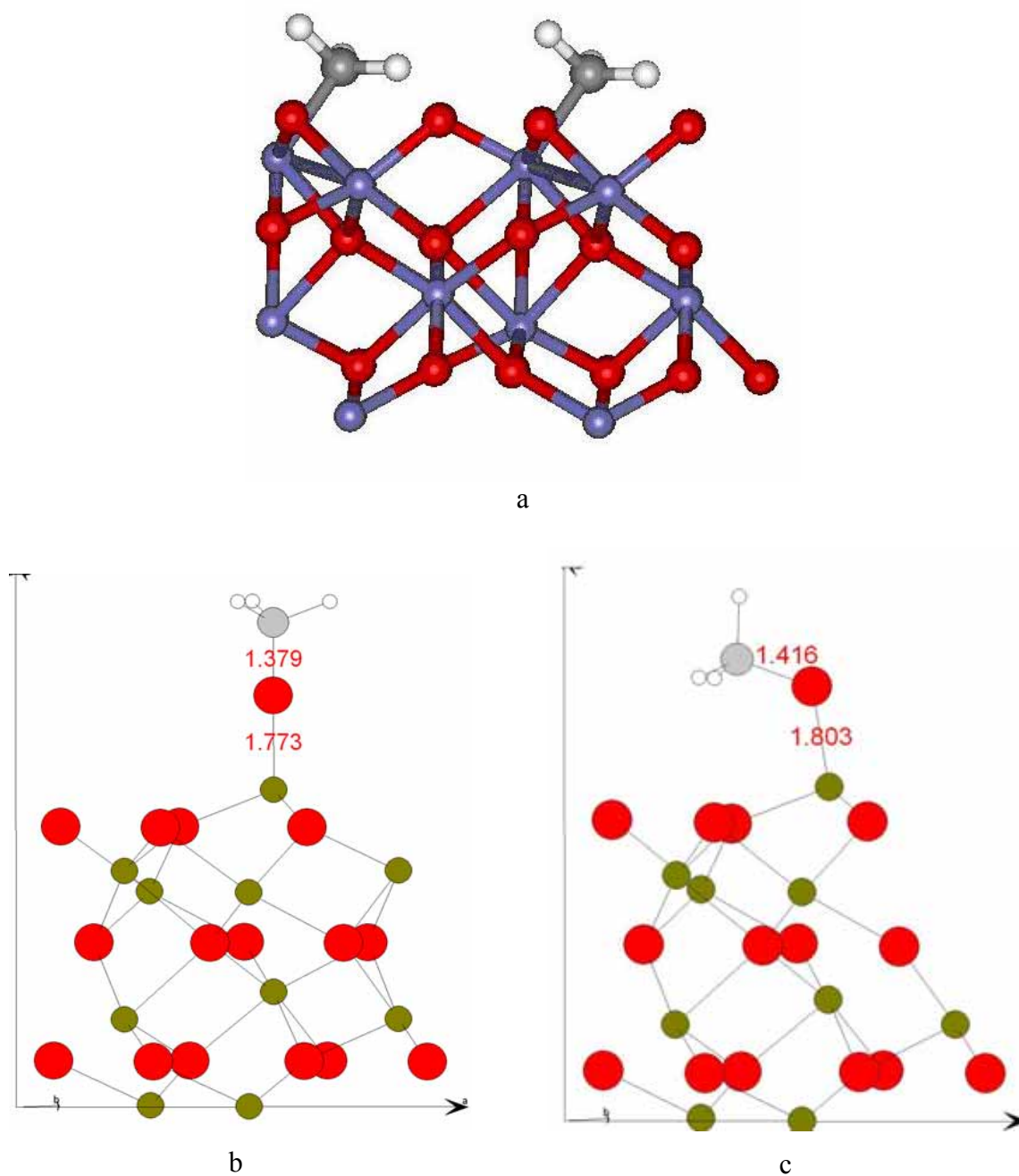
Figure 2.5 CH$_3$· adsorption on O2-terminated and O=Fe- terminated surfaces.

(a) O2-termination with CH$_3$· on oxygen vacancy site; (b) O=Fe-termination with CH$_3$· on the top of O atom; (c) O=Fe-termination with CH$_3$· on the side of O atom.

2.4.3.4 O=Fe-terminated surface

Two highly symmetric adsorption sites are investigated for the case of $CH_3\cdot$ adsorbing on the O=Fe-terminated surface, the so-called "ferryl structure" [26].

(1) Directly adsorbed on top of O (Figure 2.5b);

(2) Directly adsorbed on the bridge site between two neighboring O=Fe- groups (Figure 2.5c).

In the first case, the adsorption geometry of $CH_3\cdot$ is similar to the "O3-top" adsorption model. However, the C-O bonding distance here is only 1.38 Å compared to 1.42 Å in the "O3-top" case. This might be due to the O atom's lower coordination number in the ferryl case. The adsorption energy is -3.4 eV, the largest found for any surface model considered here.

For the adsorption of $CH_3\cdot$ at the bridge position between two O=Fe- groups, geometric relaxation predicts a bonding between C and topmost O atom. A 31° tilt angle of the C-O bond is observed, probably due to repulsion from the nearest Fe atom. The O upon which the adsorption takes place moves upward. As large bond reformation is associated with this process, for 1 ML coverage, DFT–GGA predicts modest exothermic adsorption energy of -1.1 eV. A summary is included in Table 2.3.

Table 2.3 CH$_3\cdot$ adsorption on different terminations of α-Fe$_2$O$_3$ (0001) surface

Case	E$_{ad}$(eV)	C-O/Fe (Å)	Tilt angle (°)
Fe-terminated On-top Fe	-2.3	1.97	0.0
Fe-terminated On-top O	-1.8	1.44	4.6
O3-terminated On-top O	-3.2	1.42	0.0
O3-terminated Bridge-tilt	-3.0	1.43	14.2
O3-terminated Bridge-dissociation	-2.6	1.28	26.0
O3-terminated Hollow site	No adsorption	N/A	N/A
O2-terminated On-top O	-3.0	1.42	3.1
O2-terminated Hollow site	-1.7	2.06	31.9
O=Fe-terminated On-top O	-3.4	1.38	0.0
O=Fe-terminated Bridge-tilt	-1.1	1.42	30.5

Note: $E_{ad} = E_{surface-CH_3\cdot} - (E_{surface} + E_{CH_3\cdot})$.

2.4.3.5 Fe$_3$O$_4$ (111) and FeO (111) surfaces

Four cases are considered for CH$_3\cdot$ adsorption on Fe$_3$O$_4$ (111) surfaces (1)-(4) and one for

FeO (111) (5). In all cases, adsorption is directly "on top":

(1) O on ¾ Fe$_{oct}$ + ¼ O surface (Figure 2.1a);

(2) Fe$_{oct}$ on ¼ Fe$_{oct}$ + ¼ Fe$_{tet}$ surface (Figure 2.1b);

(3) Fe$_{tet}$ on ¼ Fe$_{oct}$ + ¼ Fe$_{tet}$ surface (Figure 2.1c);

(4) Fe$_{tet}$ on ¼ Fe$_{tet}$ surface (Figure 2.1d).

(5) Fe on Fe-terminated FeO (111) surface (Figure 2.1e).

In all the above cases, CH$_3\cdot$ is found preferable to adsorb at on-top sites of the atoms and

exhibits fairly large adsorption favorability. A summary of energy and bond lengths is

shown in Table 2.4.

Table 2.4 CH$_3$· adsorption on Fe$_3$O$_4$ (111) and FeO (111) surfaces

Cases	Site	C-O/Fe (Å)	E$_{ad}$ (eV)
Fe$_3$O$_4$ — ¾ Fe$_{oct}$ + ¼ O	O	1.44	-1.9
Fe$_3$O$_4$ — ¼ Fe$_{oct}$ + ¼ Fe$_{tet}$	Fe$_{oct}$	1.99	-3.1
Fe$_3$O$_4$ — ¼ Fe$_{tet}$ + ¼ Fe$_{oct}$	Fe$_{tet}$	2.02	-2.5
Fe$_3$O$_4$ — ¼ Fe$_{tet}$	Fe$_{tet}$	1.97	-2.0
FeO — Fe-termination	Fe	1.99	-1.6

2.5 Electronic structure by embedded cluster studies

Geometric models used in embedded cluster study are the fully relaxed structures obtained in previously described plane wave slab band structure calculations.

The purpose of using the cluster method is to understand the underlying electronic structure and bonding characteristics beyond geometric structure and energy. Two adsorption cases are selected to represent adsorption of CH$_3$· in both on-top Fe (Fe-terminated) and on-top O (O=Fe-terminated) cases.

Figures 2.6a and 2.6b show the LDOS, depicting the density of electrons of given energy for selected atomic orbital character, before and after adsorption in the on-top Fe case. Comparing the two spectra, there is little change in the Fe 3d distribution, in contrast to a large change in C valence orbitals. In Figure 2.6b, C 2p orbital peaks which are near E$_f$ are shifted below due to bonding, and the anti-bonding peaks are shrunken. According to overlap of C 2p m$_l$ and Fe 3d m$_l$ LDOS, the main bonding structure, with σ character, is due to the 2p$_z$ atomic orbital of C interacting with the 3dz^2 atomic orbital of Fe^{3+}. In Figure 2.6a, 2s and 2p orbitals on C are split due to spin polarization; in Figure 2.6b, besides the broadening of C 2p bonding orbitals, split on 2s orbital is compressed due to bonding.

a

b
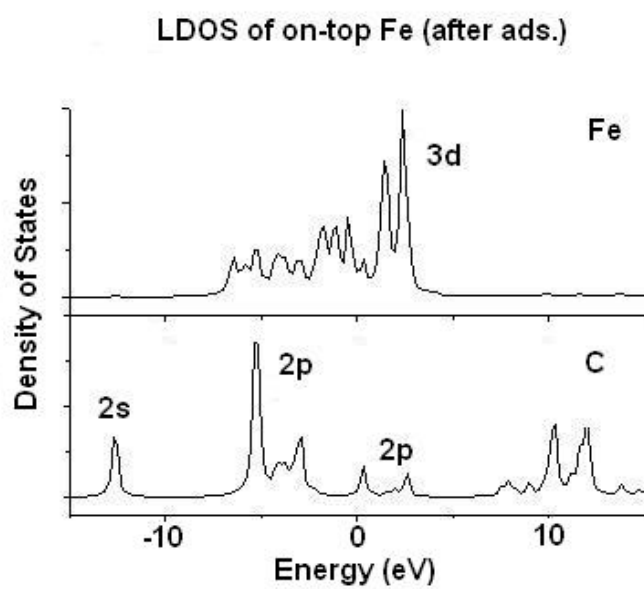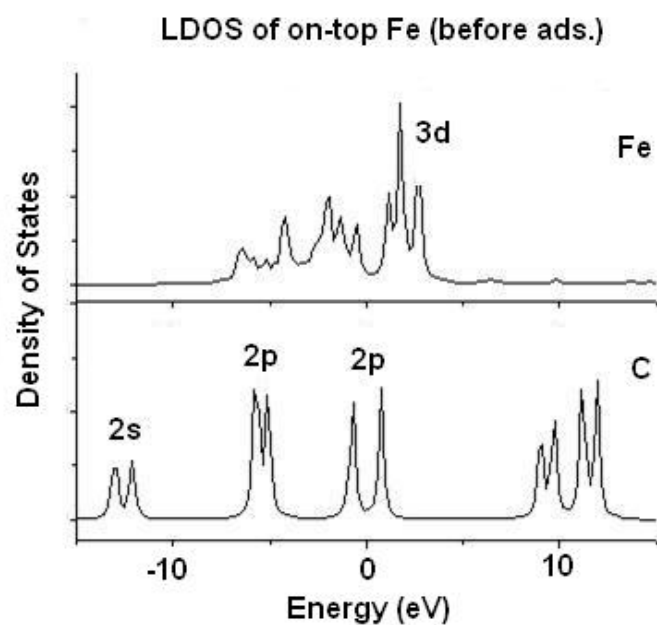
Figure 2.6 LDOS spectra for CH$_3$· on-top Fe (Fe-termination) configuration.

(a) Fe 3d and C 2s, 2p before adsorption; (b) after adsorption.

There is a rich literature on the supposed interplay of σ-donation and π-back donation in d-metal/ligand bonding; in the present surface environment, the σ-character is evidently dominant.

Figures 2.7a and 2.7b give the LDOS figures before and after adsorption on the on-top O=Fe- case. In this case, C shows very similar shift of peaks, compared with the on-top Fe case. This indicates formation of a σ bond between the C $2p_z$ and O $2p_z$ orbitals. These features are entirely expected on a qualitative basis. Table 2.5 lists Mulliken atomic charges and populations "before" and "after" adsorption for the above two typical cases.

Table 2.5 Electronic structure of selected CH$_3$• adsorption cases

On-top Fe (Fe-Hematite)		Fe	C	H
Before	Net charge Populations	2.40 $3d^{5.502}4s^{0.04}4p^{0.06}$	-0.1 $2s^{0.833}2p^{3.204}3s^{0.06}$	0.03 $1s^{0.97}$
After		2.48 $3d^{5.482}4s^{0.06}4p^{0.09}$	-0.21 $2s^{0.672}2p^{3.478}3s^{0.06}$	0.00 $1s^{1.00}$
On-top O (O=Fe-Hematite)		O	C	H
Before	Net charge Populations	-0.55 $2s^{1.983}2p^{4.508}3s^{0.05}$	-0.1 $2s^{0.833}2p^{3.204}3s^{0.06}$	0.03 $1s^{0.97}$
After		-1.05 $2s^{1.895}2p^{5.055}3s^{0.10}$	0.52 $2s^{0.344}2p^{3.102}3s^{0.03}$	0.20 $1s^{0.80}$
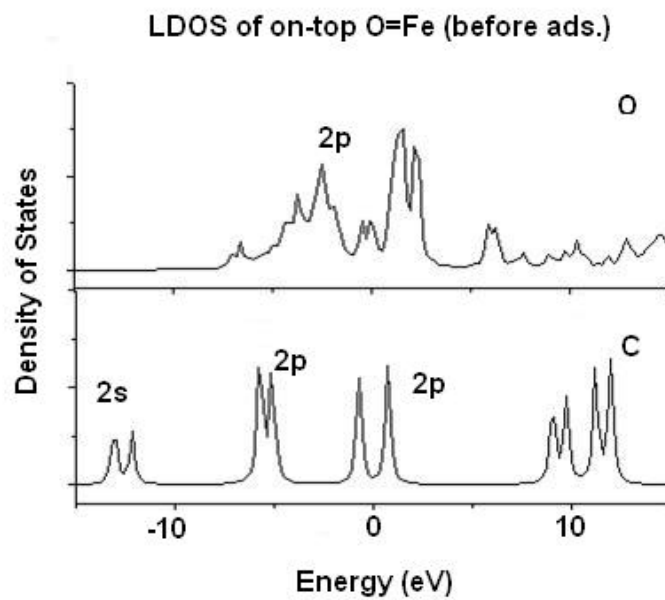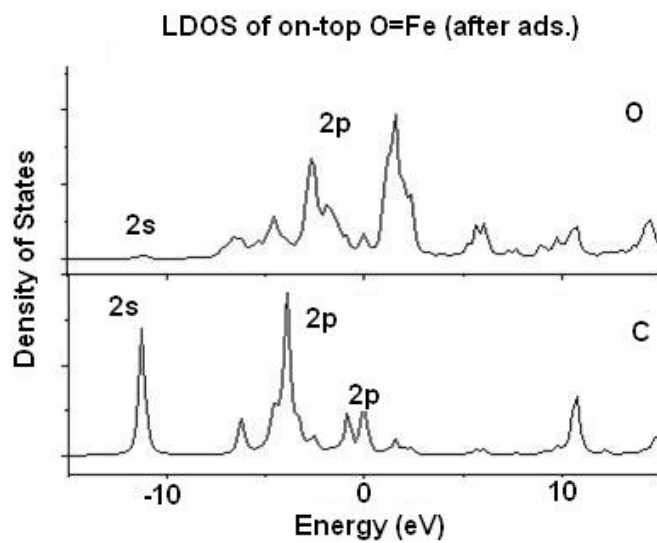
Figure 2.7 LDOS spectra for $CH_3\cdot$ on-top O (O=Fe-termination) configuration.
(a) O 2s, 2p and C 2s, 2p before adsorption; (b) after adsorption.

In the on-top Fe case, electron flow from Fe to C is as predicted; also the energy of C the 2s orbital is lowered and that of 2p is increased. The C 2s, 2p reorganization can be rationalized since the 2p orbital of C is more energetically and spatially suitable to mix with the Fe 3d orbital, which would compensate for the local atomic energy cost. In the on-top O=Fe- case, electron flow is from C and H to O, while orbitals of C 2s and O 2p rehybridize to form a σ bond. LDOS also shows rather small changes in the Fe 3d orbital which is bound to O bonded to C, showing that the effect of adsorption is well localized.

Charge density contour maps of both favorable cases are plotted by projecting the charge density to a bond-containing plane, shown in Figures 2.8a and 2.8b.

The bond critical-point charge, which was elaborated in Chapter 1.2.3, reflecting in one way the strength of covalent bonding according to Bader's topological theory of atoms, is indicated in the contour maps. In the on-top Fe-terminated case, charge density on the plane containing C, one H atom and Fe bonded with C is plotted. It shows a critical point charge density $0.102e/a_o^3$ for the C-Fe bond, but a much larger value of 0.212 e/a_o^3 for the C-H bond. This density shows the considerable covalent character existing in the C-Fe bond, which comes from the electrons shared between the C 2p and Fe 3d orbitals, as the previous Mulliken analysis showed. The C-H bond covalent component is predicted to be twice that of Fe-C.
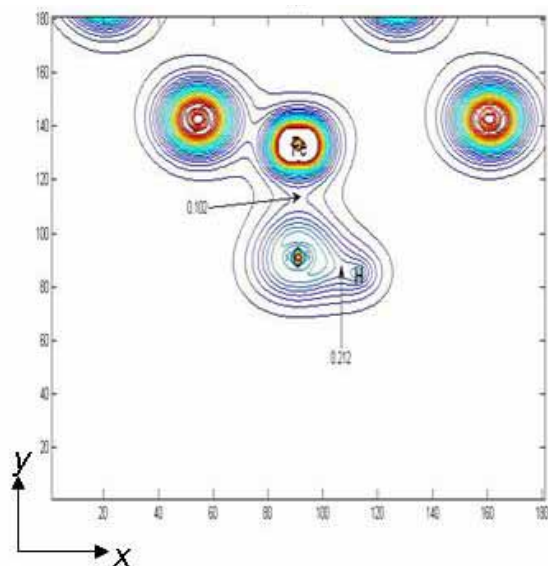
a
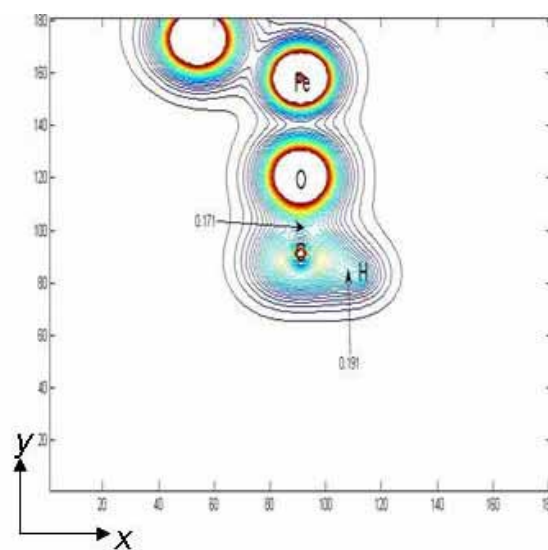
b

Figure 2.8 Charge density contour maps (in a plane defined by 3 non-linear atoms).

(a) $CH_3\cdot$ on-top Fe (Fe-terminated); (b) $CH_3\cdot$ on-top O (O=Fe-terminated).

Figure 2.8b is drawn for the on-top O=Fe-terminated 'ferryl' case, where the critical-point charge density is $0.171 e/a_o^3$ for the C-O bond and $0.191 e/a_o^3$ for a C-H bond. This clearly shows the expected strong covalent character in C-O bonds.

To explore more completely the bonding structure resulting from C-Fe and C-O adsorption, a localized-cluster approach is adopted for electronic structure analysis by comparing typical adsorption cases. Besides the two cases described above, on-top O (Fe-terminated α-Fe$_2$O$_3$ (0001) and on-top O (O3-terminated α-Fe$_2$O$_3$ (0001)) are also incorporated into Table 2.6.

Table 2.6 Bonding analysis on Hematite (0001) surface

	On-top Fe (Fe-)	On-top O (Fe-)	On-top O (O3-)	On-top O (O=Fe-)
Bond type	C-Fe	C-O	C-O	C-O
Bond length (Å)	1.97	1.44	1.42	1.38
ρ_c (C-Fe/O)(e/a$_o^3$)	0.10	0.16	0.21	0.17
Bond Order (C-Fe/O)	0.38	0.20	0.36	0.30
E_{ionic} (eV)	-3.7	-6.8	-6.0	-5.7
E_{ad} (eV) (by VASP)	-2.3	-1.8	-3.2	-3.4

Note: $E_{ionic} = \dfrac{Q_A \times Q_B}{R_{AB}}$. Q_A, Q_B are Mulliken charge of two bonded ions; R_{AB} is bond length.

The critical-bond-point density ρ_c, and bond order (BO) represent the strength of covalent bonds in different ways. For the three C-O bonding cases, the trend is the higher ρ_c, the higher bond order, which makes sense, as comparing the bond-center maximum with the total shared charge. The on-top O=Fe- model is exceptional, with lower critical charge density but much higher bond order. It also has the shortest bond length, but moderate covalent bond strength. This could be understood in two ways. First, compared with on-top

O in the O3-terminated surface case, the coordination number of the bonded oxygen atom is lower, so the strength of C-O bond could be stronger. Second, the Coulomb repulsion between the positively charged C, H and Fe atoms is not negligible. For on-top O (Fe-termination), it requires energy compensation for the adsorption, while the larger distance in the O=Fe-top case lowers this requirement.

2.6 Discussion and conclusions

The methyl radical has been proposed as an intermediate in a variety of catalytic reactions. For example, the dehydrogenation of methyl radicals is an important elementary step in steam reforming and methanation reactions. Furthermore, the methyl radical surface chemistry can contribute to the understanding of the interactions between hydrocarbon radicals and surfaces with technological importance. Thus, the surface chemistry of methyl radicals on catalytically active metal oxides surfaces has been the subject of many surface science studies.

As shown in the preceding part of this chapter, no matter what terminations of Hematite (0001) are considered, there is a predicted strong adsorption of methyl radicals. This finding is markedly different from previous $CH_3\cdot$ adsorption studies on non-polar MgO (100) [13] and NiO (100) [14] surfaces in which no adsorption or very weak adsorption onto the metal sites was found. For adsorption on the Mg site of MgO (100) surface, Mg^{2+} has neither any available 2p (s^2p^6 configuration), nor low-lying 3d orbitals to support strong hybridization with C 2p orbitals. On the other hand, Ni is predicted to be able to adsorb

CH$_3$·, with -0.25 eV binding energy and resulting in bond length R$_{Ni-C}$ = 2.65 Å [14]. The systematic differences between HF vs DFT should be taken into account to evaluate theoretical predictions, since there is a systematic trend that DFT band structure will tend to predict a larger bond strength than HF cluster calculation. The latter method usually suffers from the finite size effect, basis set limitations, and lacks of inclusion of electronic correlation. The different chemical reactivity (local electron affinity) of Mg, Ni, and Fe also plays an important role; the unoccupied 3d orbitals in surface Fe ions may mix more efficiently with C 2p orbitals than Ni orbitals. When considering the adsorption on O atoms, the bonding geometric configuration seems to be the dominant factor. Reasoning from this work, the main reason why the O-top on MgO (100) and NiO (100) surfaces are not active adsorption sites lies in the strong electronic repulsive force from surface-layer metal ions that inhibits the methyl radical from transferring charge to the substrate. On the other hand, for the corundum structure, if the hematite surface is O3-, O2- or O=Fe-terminated, the interaction of methyl with Fe cations is essentially negligible. Therefore, the O ions on Hematite surface are much more reactive than those on MgO (100) and NiO (100).

In the corresponding experiments by Liu [20], Temperature Programmed Desorption (TPD) results were compared on "biphase", Hematite (0001) and Magnetite (111) surfaces, detecting very little methyl adsorption on "biphase", and only 4.5% of methyl radical adsorbing on the Hematite surface [32]. So he tended to discount the adsorption probability of regular sites on α-Fe$_2$O$_3$ (0001) and FeO (111) surfaces. In his suggestion, the most probable surface sites on Fe$_3$O$_4$ (111) responsible for methyl adsorption are two oxygen sites with dangling bonds (Figures 2.9a and 2.9b). Furthermore, he estimated from the TPD

spectra the binding energy of methyl radical with Fe_3O_4 (111) to be -1.4 eV (Figure 2.10a), while it is -1.3 eV with the α-Fe_2O_3 (0001) surface (Figure 2.10b).

a

b
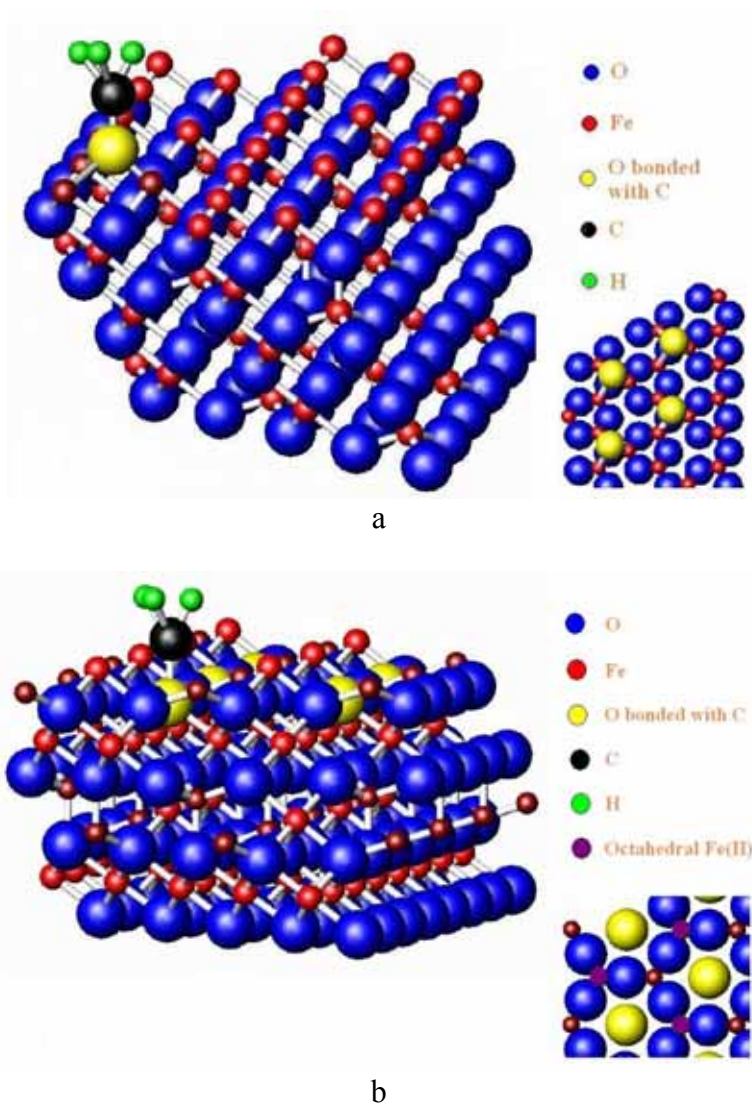
Figure 2.9 $CH_3\cdot$ binding to Fe_3O_4 (111) surface sites with dangling bonds proposed by

Liu [20].

(a) to a surface oxygen atom on the ¾ Fe_{oct} + ¼ O surface; (b) to a surface oxygen atom on the ¼ Fe_{oct} + ¼ Fe_{tet}.
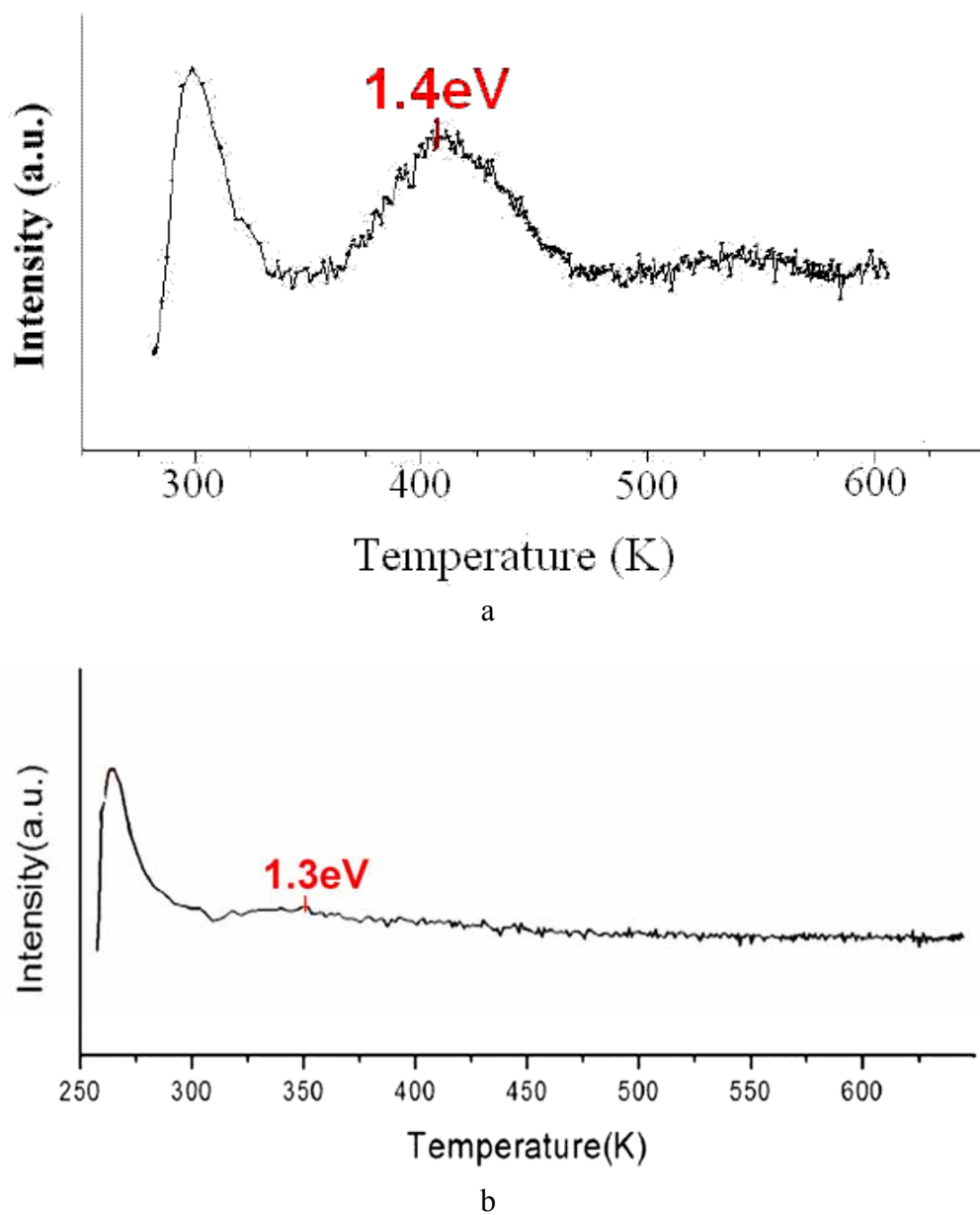
Figure 2.10 TPD spectra of CH$_3\cdot$ on iron oxide surfaces [32].

(a) on the Fe$_3$O$_4$ (111) terminated surface; (b) on the α-Fe$_2$O$_3$ (0001) terminated surface. TPD indicates binding energy of -1.4 and -1.3 eV for each case, respectively.

There is a dilemma resulting here from comparison of theory and the corresponding experiments. What is the level of reliability of DFT-GGA calculations on similar materials and surfaces? According to the existing literature of small molecule adsorption on metal oxides, by far the best studied systems are CO, NO and NH_3 on MgO (100), NiO (100) or mixed crystals like $Ni_xMg_{1-x}O$ (100). Variations among different computational methodologies (cluster, VASP, CASTEP, etc.) typically show a variance of a few tenths eV for comparable cases, with systematic overbinding of ~0.3-0.7 eV and bond length errors of ~0.1Å or less [16-19]. The *largest* marginal error of ~0.7 eV compared to experiment, found in the NO:NiO(100) case [17] using the same codes as in the present work, can be thus taken as a working estimate of the maximum error in this calculation. So, even considering the systematic errors, there is no change of the prediction that on-top Fe- and on-top O- are good candidates to bind with methyl radicals on the studied surfaces. Furthermore, the reference-state calculations on bulk hematite and clean hematite surfaces are consistent both with other theoretical works and experiments. Thus the calculated qualitative pattern that for $CH_3\cdot$ adsorption on both Fe- and O- sites of clean hematite (0001) surfaces is reliable, barring some gross effects due to Fe 3d-3d correlations which would perturb the electronic level structures.

However, comparing the experimental results and theoretical work in this study shows greater differences with predicted adsorption energies of at least -2 eV for most cases. In Figure 2.10a, the experimental C-O binding of ~ -1.3eV indicates some binding to α-Fe_2O_3 (0001) surface, but the density of sites is found to be only a few percent of "Normal" surface atom density [32]. It is possible that the surface is passivated by some undetected

impurities. Liu [20] reported that surface contamination by Ca and K amounts to ~1/5 to 1/6 atom/surface cell – charge donation from these cations could modify the surface reactivity. In order to verify this expectation, additional TPD experiments have been performed on a Hematite (0001) surface where K and Ca are below the detection limit of Auger Electron Spectroscopy. The results of these experiments are essentially the same as previously reported here: very small saturation coverage and maximum desorption activation energies of approximately -1.0 eV [33]. Thus, it appears that K and Ca impurities do not significantly affect methyl radical binding to iron oxide surfaces. Is it possible that the chemically active surface (mono) layer is of completely different structure than the subsequent layers imaged by LEED? This possibility can not be excluded.

On the other hand, DFT has some limitations dealing with small molecule adsorption on metal oxide surfaces, especially in the case of treating strong 3d correlation effect of transitional metal oxide surfaces. There are some possible solutions toward this problem: using a hybrid exchange-correlation potential such as B3LYP; using the empirical DFT+U method; using an improved post-HF method that can explicitly deal with dynamic electron correlation. Recently, some attempts to improve DFT predictions have been made using the DFT+U method [16,17]. However, these attempts are still in the early stages, and are thus not focused on this dissertation.

CHAPTER 3

ADSORPTION OF OTHER MOLECULES/ATOMS ON

HEMATITE SURFACES

Part I. Initial Stages of H_2O Adsorption and Hydroxylation on

Fe-terminated Hematite (0001) Surface

3.1 Introduction

H_2O adsorption and hydroxylation on Fe-terminated Hematite (0001) surfaces are well known in modifying the surface structure, composition and reactivity [1-3]. Generally, it is suggested that H_2O molecules can bind to oxide surfaces as a Lewis base, but the detailed process of H_2O's dissociative adsorption is poorly understood [4-6]. In addition, the defect configuration might play an important role in surface reactions [7], but limited experimental techniques keep people from better investigating the defect sites, and therefore proposing the possible mechanisms. The so-called "ferryl structure" can be seen as one special type of defect. Lemire et al. have observed ferryl groups (Fe=O-) on an Fe-terminated Hematite surface to be stable at certain oxygen pressures [8], which are expected to be active centers in some Hematite surface related reactions.

Most theoretical works on α-Fe_2O_3 (0001) surfaces have focused on the analysis of structure with different terminations and stoichiometries [7,9,10], but only a few works have dealt with the hydroxylated and hydrated (0001) surfaces. Wasserman and co-workers simulated hydroxylation of Hematite (0001) and $(1\bar{1}02)$ surfaces using parameterized analytical potentials [11], finding that hydroxylation is energetically favored in both gas-phase and solution-phase. Jones et al. studied the coverage effect of water adsorption on Hematite (0001) surfaces using an atomistic potential [12], showing that, at high H_2O coverage, the hydrated Fe-terminated surface is unstable and will lead to the detachment of $Fe(OH)_3$, resulting in a hydroxylated O-terminated surface; but at less than 33% coverage (one H_2O molecule per unit cell), in which Fe is not fully coordinated, the hydrated surface

is predicted to be relatively stable. This coverage is therefore used in the present calculations.

This section will report DFT research on molecular adsorption and dissociative adsorption of H_2O on Fe-terminated Hematite (0001) surfaces. Several possible orientations are studied to determine the most favorable adsorption configurations. Electronic structure calculations and charge density maps will help to reveal mechanisms of different surface interactions. Dissociative adsorption on an oxidized ferryl site is also studied, to examine suggested local reactivity enhancement.

3.2 Computational Methods and Models

3.2.1 Periodic slab plane wave band structure calculations

The band structure calculations have been performed on the basis of spin-polarized DFT theory with the Vienna *ab initio* simulation package (*VASP*), using a periodic slab model (see Chapter 1.2.2 for program details, and [13] for detailed parameters).

An asymmetrical anti-ferromagnetic Fe-terminated Hematite (0001) slab containing 12 atomic layers is imported from previous bulk calculations [14]. Monolayer adsorption of one H_2O molecule on each unit cell is considered (this is called '1/3 coverage' in Jones' notation [12]). Three possible molecular adsorptions on this surface are optimized by taking into account the possible interactions between surface and adsorbates. Hydrogen bonding, as a non-trivial inter-molecular interaction, is also considered. Two dissociative adsorptions

are studied: homolytic dissociation, $H_2O \leftrightarrow HO\cdot + 1/2\ H_2$; and heterolytic dissociation, $H_2O \leftrightarrow OH^- + H^+$. The former results in only one surface hydroxyl associated with surface Fe, while the latter produces two types of surface hydroxyl groups --- one is associated with surface Fe and the other is formed by protonating a near-surface O atom. The adsorption energy is calculated according to the expression, $E_{ad} = E_{surface-adsorbate} - (E_{surface} + E_{adsorbate})$, where $E_{surface-adsorbate}$ is the total energy of the adsorbed surface system, $E_{surface}$ is the total energy of the clean surface, and $E_{adsorbate}$ refers to the energy of the free adsorbate. According to this definition, negative E_{ad} generally indicates a stable adsorption taking place.

In addition, H_2O molecular and dissociative adsorptions on a ferryl-terminated surface are also examined. In molecular adsorption, a water molecule is adsorbed directly onto the ferryl Fe atom. In dissociative studies, two cases are investigated: 1) a hydroxyl adsorbs on ferryl Fe and a proton binds to ferryl O; 2) a hydroxyl adsorbs on ferryl Fe and proton binds to an oxygen atom of the partially exposed second layer.

3.2.2 Cluster calculation

In order to obtain chemically intuitive interpretations of the surface bonding structure and the associated electronic distribution, an embedded cluster study using the Discrete Variational Method (DVM) with a numerical atomic orbital basis set (see chapter 1.2.3 for program details) is also carried out. Variational clusters generally containing around 55 atoms (slightly different from case to case) are carefully selected by centering on the sites

where adsorption takes place. The geometries are directly imported from the previous band structure surface relaxation calculations. Mulliken atomic orbital populations, atomic charges and the corresponding bond orders are compared in order to detect adsorption-induced charge transfer and modification of the mixed ionic-covalent metal-ligand bonding. Charge-density maps and bond-critical-point charge density ρ_c [15], which is the density value along inter-atomic line where the gradient of ρ_c is 0, are also presented for better visualization of charge distribution.

3.3 Results and discussion

3.3.1 Molecular adsorption on a regular Fe-terminated surface

Three stable water molecular adsorption configurations are found (Figure 3.1). (a) H_2O stands on the surface with its O_{ad} binding to a surface Fe atom (denoted as Fe_s). In this case, H_2O's C_{2v} axis is parallel to the surface normal. (b) H_2O lies flat on the plane parallel to the surface with its O_{ad} binding to Fe_s. (c) H_2O molecule tilts and forms a Hydrogen bond (H-bond) with surface O atom (denoted as O_{s-1}, for it is on the second layer of a single Fe-terminated slab). Bond lengths and adsorption energies are summarized in Table 3.1 [16].

Table 3.1 Bond lengths and adsorption energies for H_2O molecular adsorption on a Fe-terminated surface

	Standing-on	Lying-on	Tilted with H-bond
Fe-O Bond length (Å)	2.17	2.23	2.22 (H-bond: 2.06 Å)
E_{ad} (eV)	-0.34	-0.58	-0.44

Note: $E_{ad} = E_{surface-H_2O} - (E_{surface} + E_{H_2O})$

In the three structures, Fe_s-O_{ad} bond lengths are somewhat longer than those of Fe-O bonds in the bulk, which are 1.92 Å and 2.13 Å for two types of Fe-O bonds, respectively (Chapter 2, Figure 2.3), and much greater than the Fe_s-O_{s-1} bonds (1.79 Å) [16] in the clean surface. These longer distances here suggest weak molecular interactions between H_2O and the surface. In structure (c), H_2O forms a H-bond of 2.06 Å with O_{s-1}, a little bit greater than the intermolecular distance for H-bond in liquid water (1.88 Å, at 4℃) [17].
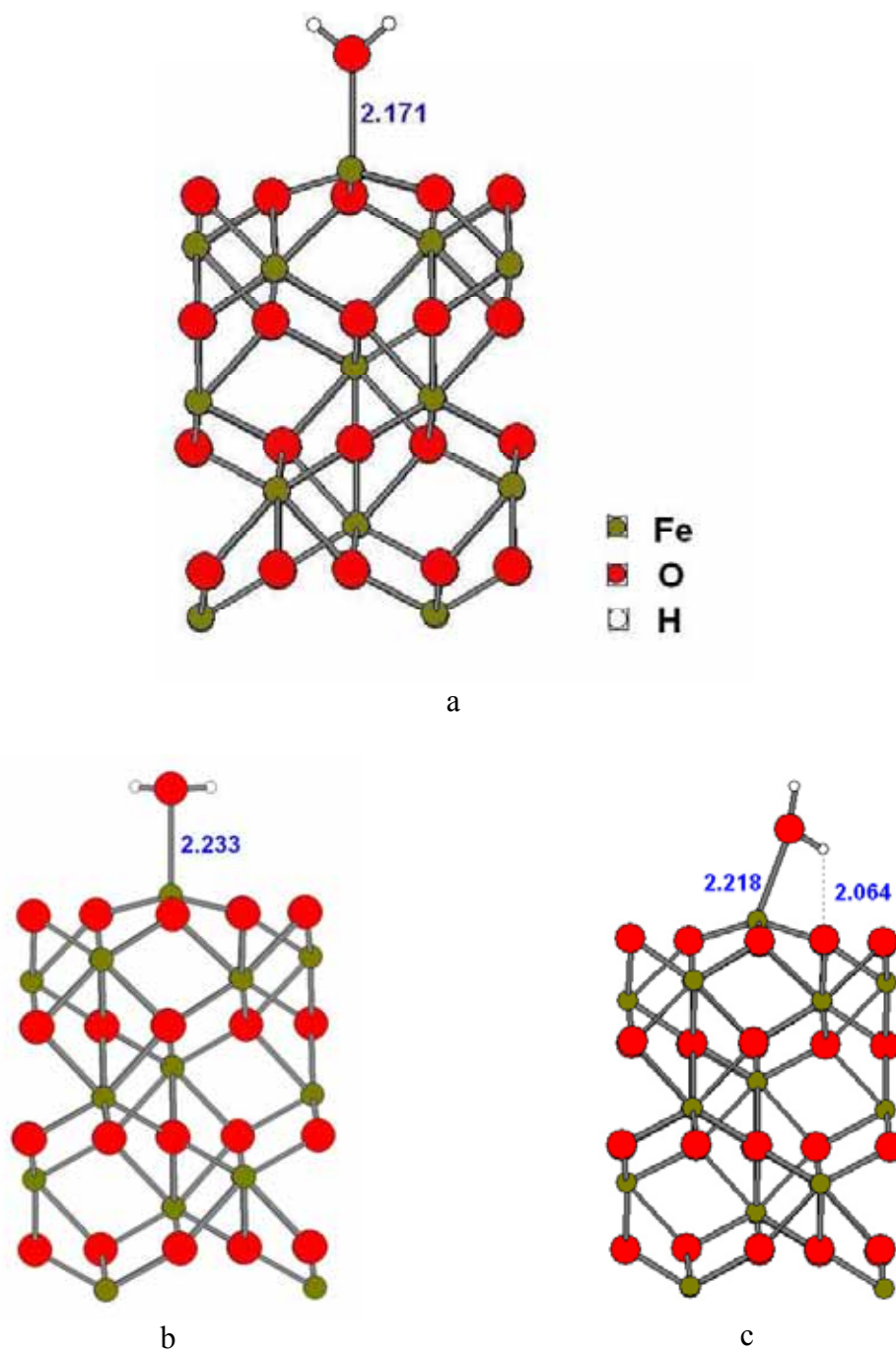
Figure 3.1 H_2O molecular adsorption on Fe-terminated Hematite (0001) surface.

(a) Standing-on; (b) Lying-on; (c) Tilted and forming an H-bond. Bond lengths are given in Å.

Small adsorption energies prove the existence of weak physical adsorption. This weak adsorption conclusion is consistent with a combined STM and computational study by a Hartree-Fock approach [18]. Structure (b) is slightly more favored among the three, and forming a H-bond is found to favor H_2O adsorption, since configuration (c) is energetically more favorable than the standing-on case (a) by virtue of forming a H-bond with O_{s-1}. Although the lying-on case (b) has longer Fe_s-O_{ad} bond length than that of (a), the flat configuration makes it easier to gain energy favor by forming H-bond(s) (the average H-O_{s-1} distance is 2.78 Å, not denoted in Figure 3.2c).

3.3.2 Dissociative adsorption on a regular Fe-terminated surface

Homolytic dissociation results in the releasing of $1/2H_2$ (gas phase) and binding of neutral HO· to Fe_s. Figure 3.2a shows the optimized surface geometry after homolytic dissociation. HO· stands on top of Fe_s. The adsorption energy is positive (Table 3.2), implying that homolytic dissociation is energetically unfavorable. However, a sole HO· radical can result in adsorption energy of -3.05 eV on this site [16], which shows HO· has very strong affinity to the surface. The same conclusion is drawn when methyl radical can stably adsorb on the same site with -2.31 eV adsorption energy [7]. So, the on-top Fe site of a Fe-terminated surface is a good place to interact with some small free radicals.

Table 3.2 Bond lengths and adsorption energies for H_2O dissociative adsorptions on Fe-terminated surface

	Homolytic: $H_2O \rightarrow HO\cdot + 1/2H_2$	Heterolytic: $H_2O \rightarrow OH^- + H^+$
Fe-O Bond length (Å)	1.77	1.83
E_{ad} (eV)	+0.28	-0.83
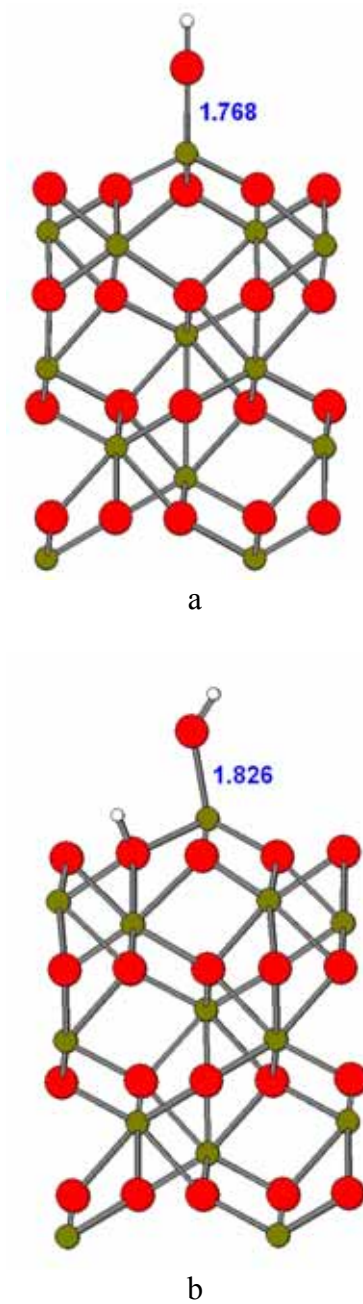
Figure 3.2 H$_2$O dissociative adsorption on a Fe-terminated Hematite (0001) surface.
(a) homolytic dissociation; (b) heterolytic dissociation.

Figure 3.2b shows the equilibrium configuration of heterolytic dissociative adsorption. O_{ad} of the dissociated OH⁻ group from H_2O is attached to Fe_s, forming a tilted Fe_s-O_{ad} bond, while the proton binds with a nearby O_{s-1}, forming a second surface hydroxyl group. Adsorption energy is -0.83 eV in this case, showing that heterolytic dissociation is energetically favored compared with homolytic dissociation and molecular adsorptions, largely due to bond breaking and reforming effects.

3.3.3 Adsorption on a ferryl-terminated surface [16]

For the molecular adsorptions (Figure 3.3a), the Fe=O- bond is elongated from 1.59 Å [19] to 1.67 Å and stays tilted. In Figure 3.3b, H_2O is heterolytically dissociated, leaving a bi-hydroxyl structure with one hydroxyl binding to ferryl Fe and a proton binding to ferryl oxygen. The proton on ferryl O also forms a H-bond with the O in OH⁻. Figure 3.3c shows the case with proton binding to surface O_{s-1}. The hydroxyl group binding with Fe_s also forms a hydrogen bond with the proton. The bond lengths and adsorption data are reported in Table 3.3.

Table 3.3 Bond lengths and adsorption energies for H_2O adsorption on ferryl site

	Molecular	H^+ with ferryl O	H^+ with surface O_{s-1}
Fe-O_{ad} Bond length (Å)	2.08	1.79	1.81
Fe=O Bond length (Å)	1.67	1.83	1.66
E_{ad} (eV)	-0.29	-0.36	-0.11
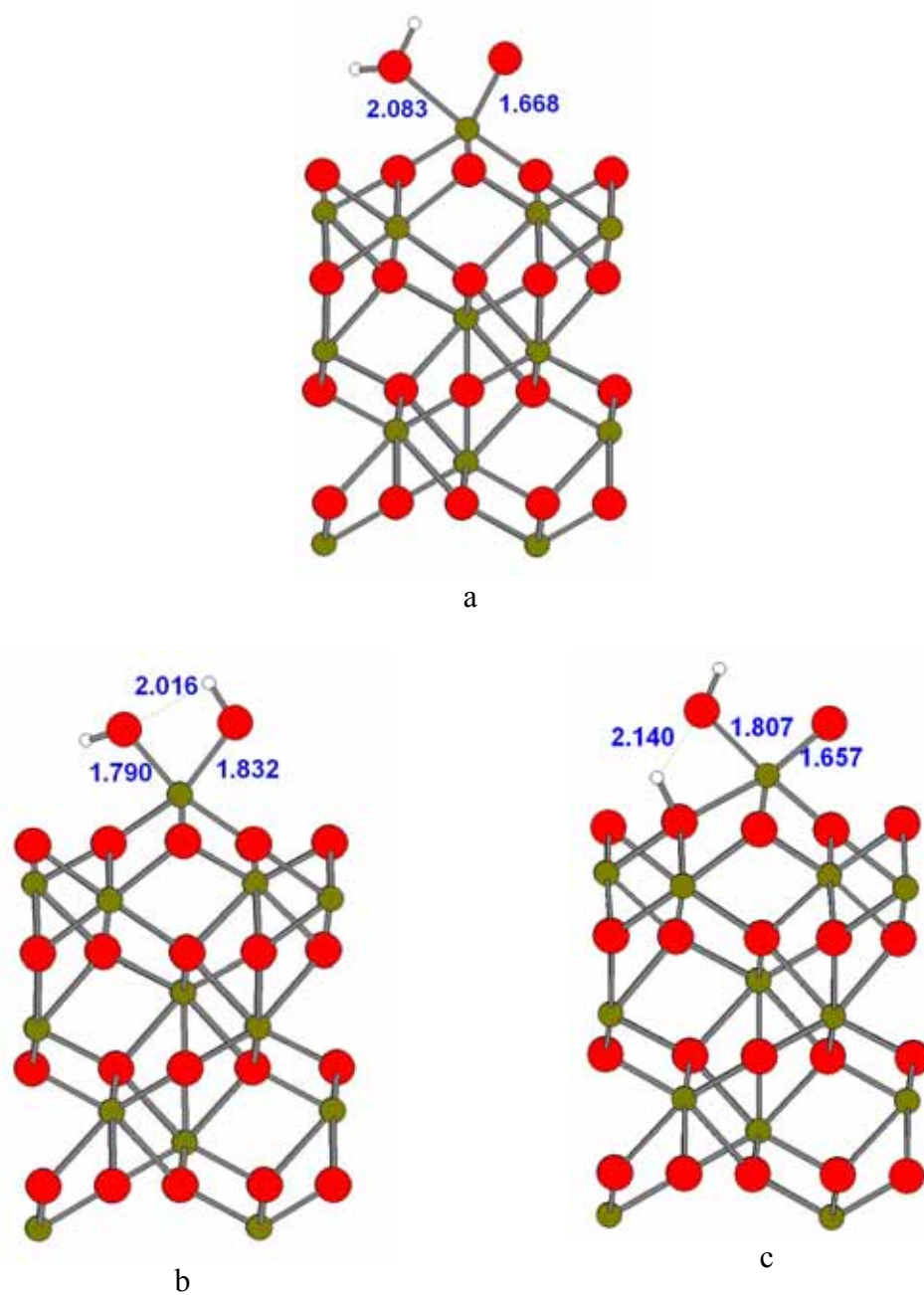
Figure 3.3 H_2O adsorption on ferryl-terminated Hematite (0001) surface.

(a) molecular adsorption; (b) heterolytic adsorption (H^+ with ferryl O); (c) heterolytic adsorption (H^+ with surface O).

Table 3.3 shows that the ferryl site is not favorable for H_2O adsorption. It has a -0.29 eV energy gain for molecular adsorption, less than its counterpart on regular Fe on-top site (-0.58 eV); it only has -0.36 eV and -0.11 eV for dissociative adsorption. This ferryl site shows strong affinity to free radicals, but it is obviously not an active center for molecular and dissociative adsorption. This could be explained by over-coordination of the ferryl Fe atom. The inner 4-member ring in Figure 3.3b seems to show a slight stability preference over the other cases in this category. Considering DFT's trend of overestimating the adsorption energy around 0.5 ~ 0.7eV [20], this small energy difference might not be sufficient to prove the ferryl site is an active defect site for H_2O adsorption. More experiments and other theoretical methods need to be carefully considered.

3.4 Electronic structure of adsorption systems

The electronic structure of two dissociative adsorption cases is investigated using the embedded cluster method. Table 3.4 summarized Mulliken charge populations, atomic charges, bond orders and bond critical point density for both homolytic and heterolytic cases.

Table 3.4 Electronic structure data of H_2O dissociation on a Fe-terminated surface.

		Mulliken population	Net charge (e)	Bond orders		ρ_c (e/a$_o^3$)
Homolytic dissociation	Fe_s	$3d^{5.46}4s^{0.01}$	2.48	Fe_s-O_{ad}	-0.06	0.10
	O_{ad}	$2s^{1.94}2p^{5.80}$	-1.73	Fe_s-O_{s-1}	0.05	0.09
	O_{s-1}	$2s^{1.98}2p^{5.56}$	-1.54	O_{ad}-H	0.42	0.23
	H	$1s^{0.15}$	0.85			
Heterolytic dissociation	Fe_s	$3d^{5.48}4s^{0.02}$	2.45	Fe_s-O_{ad}	0.08	0.10
	O_{ad}	$2s^{1.96}2p^{5.77}$	-1.72	Fe_s-O_{s-1}	-0.02	0.07
	O_{s-1}	$2s^{1.93}2p^{5.72}$	-1.65	O_{s-1}-H_p	0.45	0.17
	H	$1s^{0.18}$	0.82	O_{ad}-H	0.41	0.15
	H_p	$1s^{0.23}$	0.77			
Clean surface	Fe_s	$3d^{5.64}4s^{0.07}$	2.23	Fe_s-O_{s-1}	0.15	0.11
	O_{s-1}	$2s^{1.98}2p^{5.50}$	-1.48			

Note: H_p denotes the proton produced through H_2O heterolytic dissociation.

The Mulliken population and net charge data of the equilibrium configurations show the charge transfer between Fe_s and O_{ad} is minor. The ionicity of Fe_s only increased from 2.23e to 2.48e and 2.45e according to results of clean surface, mono-hydroxylated and bi-hydroxylated surfaces, respectively. In the two dissociative adsorption cases, the Fe_s-O_{s-1} bond orders both are lowered from the clean surface's +0.15 due to the attraction of the adsorbed hydroxyl group; what's more, for all Fe-O bonds, including Fe_s-O_{s-1} and Fe_s-O_{ad}, the bond orders are close to 0. The low bond orders indicate very few shared electrons between Fe and O atoms; i.e., the Fe-O bond is basically ionic. The charge analysis and orbital population from *VASP* calculations [16] lead to the same conclusion.

In homolytic dissociative adsorption, O_{s-1} seems less electronically affected by the hydroxyl group adsorption on ferryl Fe than in the heterolytic case, which is intuitive from the geometries (Figures 3.2a and 3.2b). The proton adsorbed on surface O_{s-1} site in heterolytic dissociation is less ionic than H in a hydroxyl group due to more electron sharing, which

also explains why $O_{s\text{-}1}$-H_p (+0.45) has higher bond order than O_{ad}-H (+0.41). Although in Figure 3.2b, the distance between O_{ad}-H_p is too great to be considered forming a H-bond, the tilted geometry of the hydroxyl group might give some contribution to the higher amount of electron sharing.

That the $O_{s\text{-}1}$-H_p pair has a stronger covalent character can also be proved in charge density contour maps, which graphically reflect the charge distribution by projecting the charge density onto a plane defined by three non-linear atoms, shown in Figure 3.4.

a

b
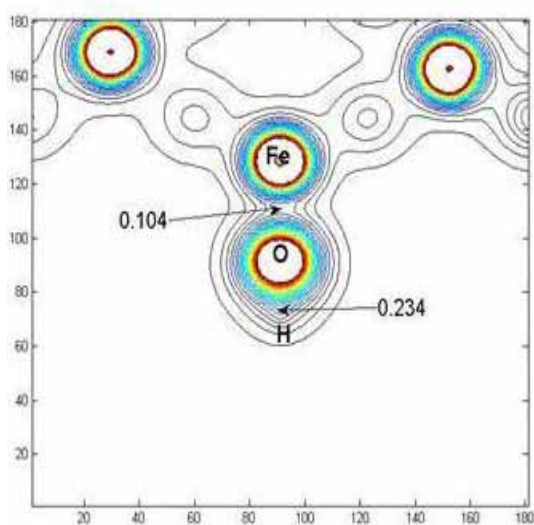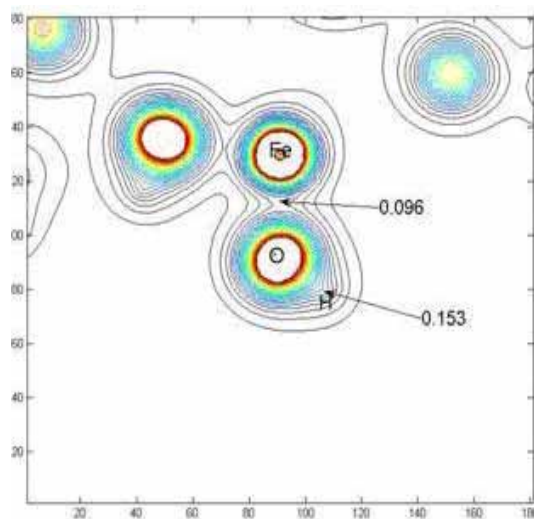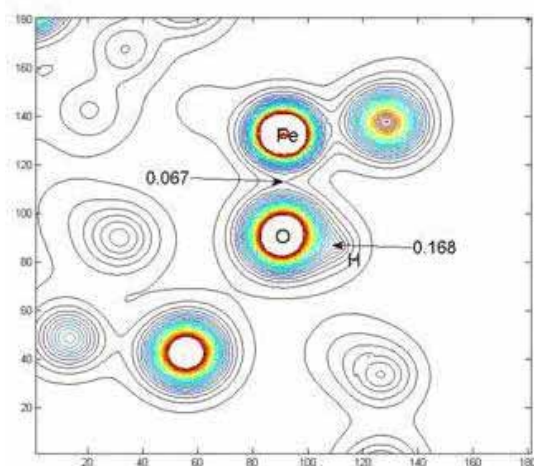
Figure 3.4 Charge density contour maps

(x-y plane defined by 3 atoms).

(a) Fe_s, O_{ad} and H for homolytic dissociation mono-hydroxylated case;
(b) Fe_s, O_{ad} and H for heterolytic dissociation bi-hydroxylated case;
(c) Fe_s, O_{s-1} and H_p for heterolytic dissociation bi-hydroxylated case.
The critical-point charge densities are given.
Equal-interval contours, ρ_c values in e/a_o^3.

c

In Figure 3.4a, ρ_c of the Fe$_s$–O$_{ad}$ pair is 0.10 e/a$_o^3$, less than its coadjacent O$_{ad}$-H pair at 0.23 e/a$_o^3$. Comparing Figures 3.4b and 3.4c, the hydroxyl group formed on the surface (0.17 e/a$_o^3$) has a little higher density than that from dissociated H$_2$O (0.15 e/a$_o^3$); the Fe$_s$-O$_{s-1}$ interaction shows higher ionicity by revealing 30% less density to Fe$_s$-O$_{ad}$: 0.07 e/a$_o^3$ to 0.10 e/a$_o^3$. At the same time, this charge density is also calculated by *VASP* and gives qualitatively similar results to the cluster calculations [16]. Thus band structure and cluster approaches imply similar electronic structure and charge information of the dissociation of H$_2$O on a Fe-terminated Hematite (0001) surface.

3.5 Conclusions

Theoretical studies of H$_2$O adsorption on Fe-terminated and ferryl Hematite (0001) surfaces have been carried out using DFT band structure and embedded cluster methods. The geometries are fully relaxed by *VASP*. Efforts have been made to calculate the adsorption energies with good precision and to extract the electronic and bonding information.

The study of this section focuses on interactions of one H$_2$O per unit cell on a Hematite (0001) surface, including molecular adsorption and dissociative adsorption, which can be further categorized into homolytic and heterolytic dissociation. The calculated adsorption energies show that molecular adsorption is less favored than heterolytic dissociation on Fe-terminated Hematite (0001) surface; and that the Fe=O ferryl site generally is not active to interact with H$_2$O, either molecularly or in a dissociative manner, although it has been found to be a very good site to bind with methyl or hydroxyl radical.

Some discussion is given here, attempting to explain the interaction mechanisms. First, it is the influence of forming a hydrogen bond. H-bond is relatively weak in the aspect of energy, but it will affect the equilibrium configuration; therefore it efficiently compensates the energy cost of adsorption and dissociation. The configuration preference to the tilted geometry in Figures 3.1c and 3.2b proves this. Second, coordination may play a role in the surface configuration: three-fold coordinated Fe at the Fe-terminated surface is expected to be more active to H_2O, compared to the ferryl Fe. The H_2O molecule is weaker as a Lewis base to Fe than either OH^- or $OH\bullet$, so molecular adsorption is less favored than dissociative adsorption.

In the electronic structure and bonding information analysis, two types of surface hydroxyls, the dissociated O_{ad}-H and the proton-adsorbing O_{s-1}-H, are carefully compared. The former is more ionic, for O_{ad} is less coordinated. In summary, the hydroxyl group adsorbs on Fe_s largely by the Coulomb force and then weakens the interaction of Fe_s-O_{s-1}.

Metal oxide surfaces possess a wide variety of defects, even if the surfaces are extremely carefully prepared. Experiments of water reaction with Hematite (0001) surfaces [21] suggest that the initial hydroxylation is associated with surface defect sites, and that only over some threshold pressure, will water react with non-defective surface sites. In the present calculations of adsorption on the ferryl defect site, there is no enhanced reactivity for water dissociation observed. It might be possible that the ferryl group can work as a catalyst in the interaction process, lowering the reaction barrier. However, there should be many other defect sites which are more closely involved in this process to enhance the surface reactivity. Because water and hydroxyl are both Lewis bases, low-coordinated Fe (by loss of either

neighboring oxygen(s) in the terrace sites or low-coordinated oxygen(s) in vacancy defect sites) will be more susceptible to hydroxyl in the initial stages of surface interaction with water. Further studies on those surface defects with water should be carried out in a similar manner.

Part II. Adsorption of Vanadium on a Hematite (0001) Surface:

submonolayer and monolayer coverage

3.6 Introduction

In this section, DFT studies of Vanadium adsorption on Hematite (0001) surfaces are briefly presented. Growth of ultra-thin metal films on metal oxide surfaces and formation of heterogeneous metal/metal oxide systems have attracted increasing interest in recent years, for they provide a novel class of materials that could enhance catalytic capability compared to a single metal oxide [22-24]. Vanadium is a common multivalent transition metal ($+3(d^2s^0)$ and $+5(d^0s^0)$ being most common), which results in a wide range of chemical reactivity. Some other supporting substrates, such as alumina, ceria, titania, silica, and other numerous metal oxides have been reported [25-27], but rare on Hematite (0001) surface [28,29].

Experimental studies of Vanadium adsorption on clean Hematite (0001) were reported by Kim [30], using both atomic resolved X-ray standing wave measurements (XSW) to detect V site geometry and X-ray photoemission spectroscopy (XPS) to detect electronic structure changes. This section reports the parallel theoretical research using DFT as a tool to explore the adsorption process, and to expand the understanding of the composition, geometry and underlying electronic structure.

Chapter sections 3.6-3.10 will focus on the interface of V/Hematite, evaluated within the framework of spin-polarized DFT; further research of the reoxidized V_xO_y/Hematite interface can be found in Jin's Ph.D. thesis [19]. Concerning V adsorption, two terminated surfaces are chosen, denoted as Fe-terminated (Fe-O3-Fe-Fe…) and O3-terminated (O3-Fe-Fe-O3…), the geometry of clean and adsorbed surfaces is relaxed, and adsorption

energies are calculated. The detailed representation of the systems' electronic structure, including charge distribution and bond order, is obtained through the embedded cluster calculations, which provide a good starting point for understanding the interface structure of V/Hematite and its influence on the surfaces' catalytic properties.

3.7 Computational Methods and Models

The periodic slab plane wave band structure calculations have been carried out on the basis of spin-polarized DFT theory with the Vienna *ab initio* simulation package (*VASP*), using a periodic slab model (see Chapter 1.2.2 for program details, and [19] for detailed parameters).

Figure 3.5 shows an idealized Fe-terminated surface (Figure 3.5); a fully oxidized monolayer O3-terminated surface can be constructed by removing the terminal Fe atoms from Fe-terminated surface. For Hematite (0001) surface, above the oxygen layer, there are two occupied high-symmetry Fe sites, distinguished as A and B, that are symmetrically equivalent to the Fe occupied octahedral sites in the bulk. Site A is located closer to the underlying oxygen layer than the B site. The C site is another high-symmetry octahedral surface site, which is not occupied in the bulk by Fe due to stoichiometry.
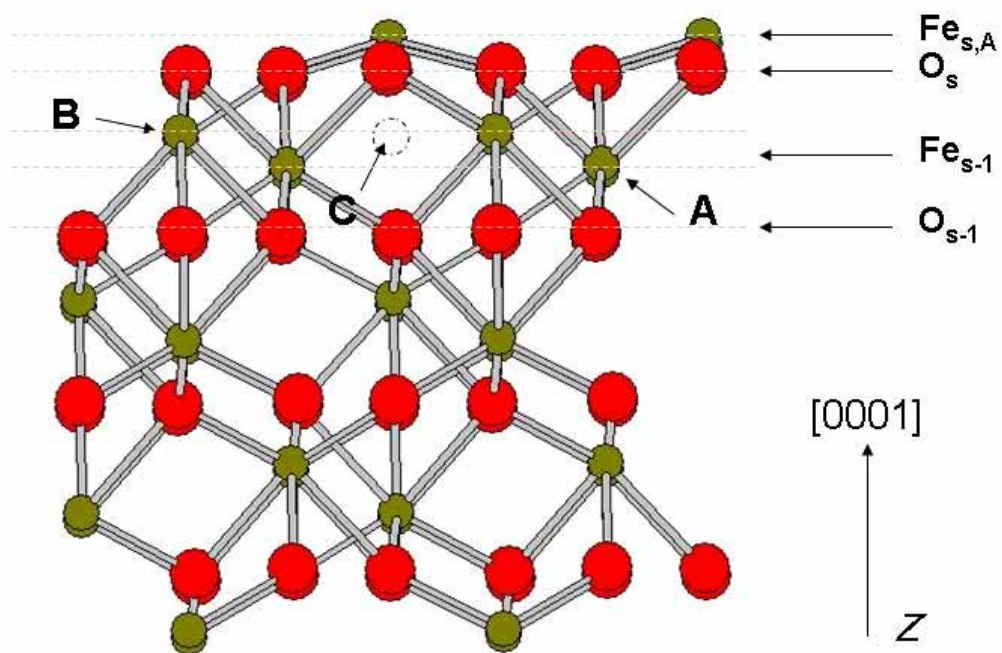
Figure 3.5 Side view of Fe-terminated Hematite (0001) surface.

Three high-symmetry sites A, B, C are indicated, as well as atomic layers near the surface.

The adsorption energy of Vanadium on Hematite surface at different coverage is defined as follows,

$$E_{ad} = \frac{1}{N}(E_{slab}^{V/hem} - E_{slab}^{hem} - NE^{V})$$
(3.1)

where, negative E_{ad} means exothermic adsorption, E^{V} is the energy of the isolated, spin-polarized V atom, and N is the number of adsorbed V atoms per unit cell.

An embedded cluster study using the Discrete Variational Method (DVM) with a numerical atomic orbital basis set is used to extract useful electronic structure and bonding information (see chapter 1.2.3 for program details, and [31] for detailed parameters). Mulliken atomic orbital populations, atomic charges and the corresponding bond orders are compared in order to detect adsorption-induced charge transfer and modification. Charge-density maps and bond critical point charge density ρ_c [15], are also presented for better visualization of charge distribution.

According to the surface terminations and V coverage, the adsorptions are categorized into 4 groups, namely, 0.5 ML (ML=monolayer) V/Fe-termination (1 Vanadium atom per unit cell), 0.5 ML V/O-termination, 1 ML V/Fe-termination (2 Vanadium atoms per unit cell), and 1 ML V/O-termination. In each category, the adsorption geometry and energy are calculated; the electronic structure is analyzed for some important cases.

3.8 Results

3.8.1 0.5 ML V/Fe-terminated interface

For this case, relaxation results show that the V direct adsorption on three-fold hollow site B (V_B, $Fe_{s,A}$) is most stable (Figure 3.6a) with E_{ad} of -6.2 eV due to the formation of three V-O bonds between the adsorbate and the substrate [31]. In (V_B, $Fe_{s,A}$), the V-O bond lengths are 1.76 Å and the vertical distance of V from the O_s plane is less than 0.1 Å. Also, the distance between V_B and the $Fe_{s-1,A}$ below is only 2.56 Å, which suggests a possible V-Fe bonding interaction.

Table 3.5 gives summaries of Mulliken populations, charges, bond orders and bond lengths obtained from SCF cluster results.

Table 3.5 Electronic structure and bonding information for 0.5 ML V/Fe-terminated interface

	Atoms	Mulliken Population	Charge	Bond order /Bond length (Å)
After	V_B	$3d^{2.63}4s^{0.31}4p^{0.16}$	1.91	V_B-$Fe_{s-1,A}$: 0.39/2.56
	$Fe_{s-1,A}$	$3d^{5.60}4s^{0.26}4p^{0.32}$	1.82	V_B-O_s: 0.36/1.76
	O_s	$2s^{1.95}2p^{5.49}$	-1.44	V_B-$Fe_{s,A}$: 0.03/2.95
	$Fe_{s,A}$	$3d^{5.54}4s^{0.10}4p^{0.08}$	2.21	
	$Fe_{s-1,B}$	$3d^{5.41}4s^{0.02}4p^{0.02}$	2.54	
Before (clean surface)	$Fe_{s,A}$	$3d^{5.51}4s^{0.11}4p^{0.14}$	2.31	n/a
	$Fe_{s-1,A}$	$3d^{5.52}4s^{0.09}4p^{0.09}$	2.51	
	O_s	$2s^{1.99}2p^{5.32}$	-1.54	
	$Fe_{s-1,B}$	$3d^{5.41}4s^{0.01}4p^{0.02}$	2.55	

$Fe_{s-1,A}$ is the most affected atom in the substrate, sharing considerable charge with the adsorbed V with bond order of 0.39. $Fe_{s,A}$ atoms are less reduced and $Fe_{s-1,B}$ are not affecte.
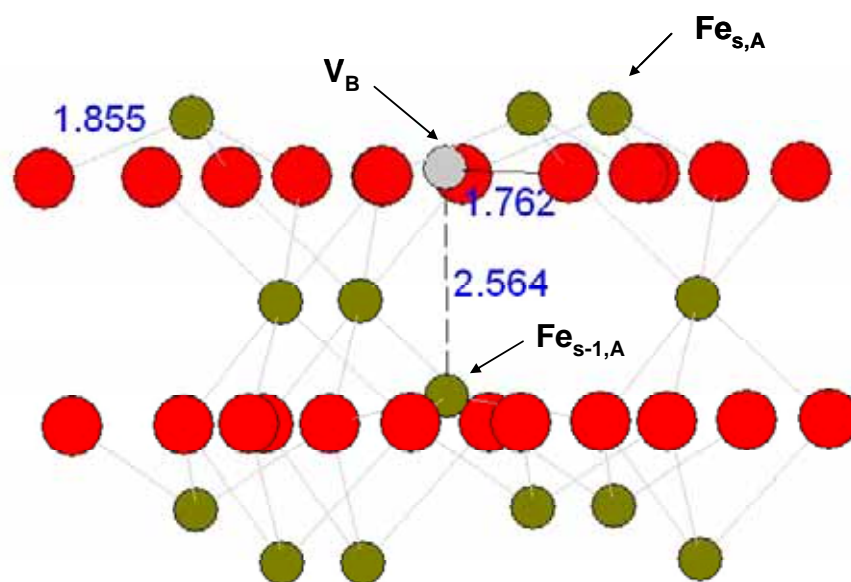
Figure 3.6a One V (V_B) adsorbed on Fe-terminated Hematite (0001) surface.
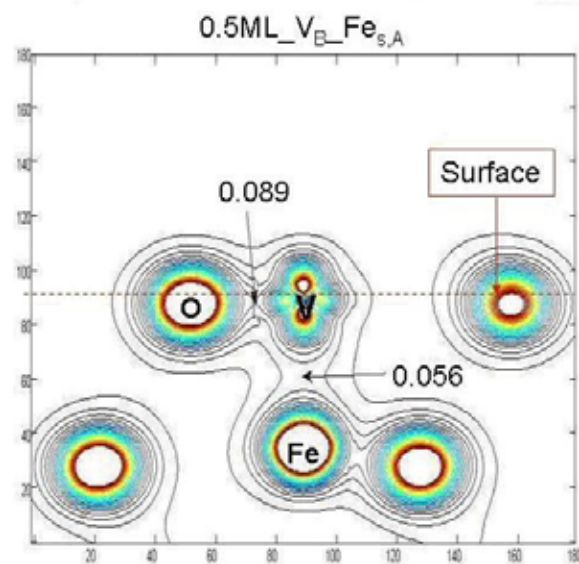
Figure 3.6b Charge density contour (V_B, O_s, $Fe_{s-1,A}$) of 0.5 ML V/Fe-terminated interface. Plane is defined by (O, V, Fe), and has equal interval.

To further clarify the significant charge sharing between V_B and $Fe_{s-1,A}$, a charge density contour map is plotted by projecting the charge density to a bond-containing plane shown in Figure 3.6b. The bond critical-point charge, as mentioned before, reflects the strength of covalent bond, according to Bader's topological theory of atoms. The bonding contour clearly shows a critical point charge of 0.056 e/a_o^3 for the V_B-$Fe_{s-1,A}$ interaction, and a larger value of 0.089 for the V_B-O_s bond. This density demonstrates the considerable V_B-$Fe_{s-1,A}$ covalent bond character due to electron sharing between V 3d and Fe 3d orbitals.

3.8.2 0.5 ML V/O3-terminated interface

In the case of 0.5 ML V adsorption on O3-terminated Hematite, the most stable adsorption site is found to be the three-fold A site (V_A, O3) shown in Figure 3.7a.

Adsorbing at site A, V will avoid repulsive interaction from the sub-surface Fe_{s-1} atoms to the greatest extent, and by forming three strong V-O bonds it can compensate for the excessive surface negative charge, resulting in a very large adsorption energy of -9.9 eV [31].
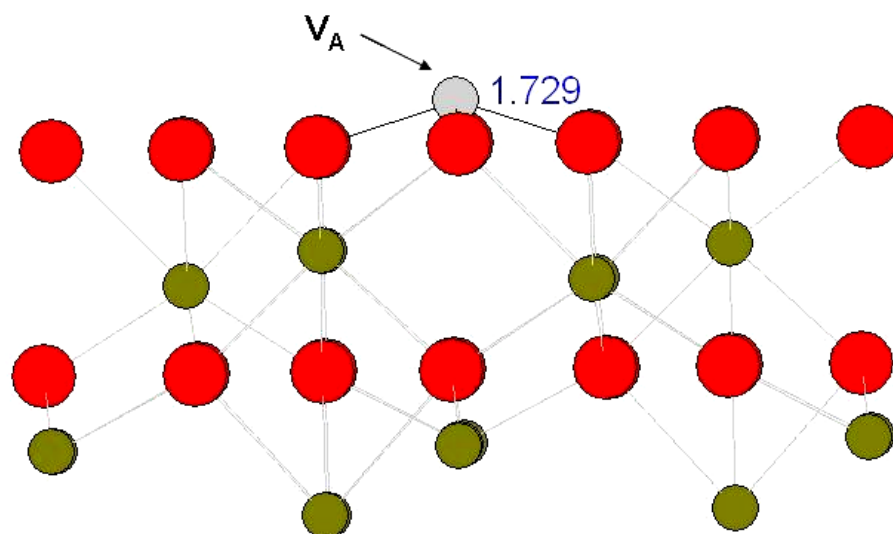
Figure 3.7a One V (V_A) adsorbed on O3-terminated Hematite (0001) surface.
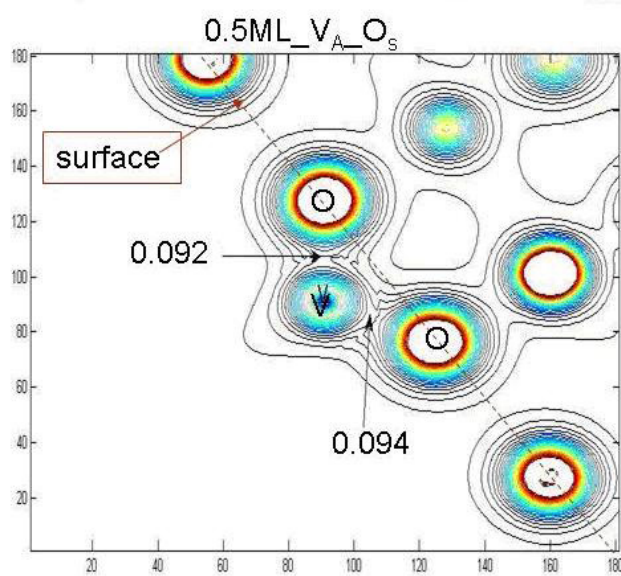
Figure 3.7b Charge density contour (V_A, O_s) of 0.5 ML V/O3-terminated interface.
Plane is defined by (O, V, O) atoms, and has equal interval.

Table 3.6 Electronic structure and bonding information for 0.5 ML V/O3-terminated interface

	Atoms	Mulliken Population	Charge	Bond order /Bond length (Å)
After	V_A	$3d^{2.36}4s^{0.05}4p^{0.05}$	2.55	V_A-O_s: 0.21/1.73
	O_s	$2s^{1.97}2p^{5.30}$	-1.27	
	Fe_{s-1}	$3d^{5.46}4s^{0.03}4p^{0.03}$	2.47	
Before (clean surface)	O_s	$2s^{1.98}2p^{5.93}$	-0.94	n/a
	Fe_{s-1}	$3d^{5.52}4s^{0.01}4p^{0.02}$	2.46	

Table 3.6 gives the cluster analysis of electron population data for the 0.5 ML V/O3--terminated interface, showing a weaker electron sharing between adsorbed V and adjacent O atoms compared to that of V_B-O_s (Table 3.5). The oxidization of V is much higher (2.55 e in Mulliken analysis) compared to that in 0.5 ML V/Fe-terminated interface, due to stronger V-O bonding. Mulliken charge of Fe_{s-1} shows no change compared to the clean surface. The charge density contour map is drawn in Figure 3.7b, where the critical-point charge density is 0.092 and 0.094 e/a_o^3 for both in-plane V-O bonds. This clearly shows the expected strong covalent character in V-O bonds, at the favored symmetrical O_3 hollow site.

3.8.3 1ML V/Fe-terminated interface

There are three possible adsorption combinations for 1ML V coverage on a Fe-terminated surface, based on the assumption that Fe doesn't occupy the same site as V. They are called (V_{AB}, $Fe_{s,C}$), (V_{AC}, $Fe_{s,B}$) and (V_{BC}, $Fe_{s,A}$) cases, in which two V atoms adsorb on top of two different 3-fold oxygen sites. These three configurations are found to have essentially equal adsorption energy of -5.0 eV within the error of the computational approach [31].

(V_{BC}, $Fe_{s,A}$) (Figure 3.8) is chosen as a representative for the following cluster analysis, because in this case, surface Fe stays in its most common site A.
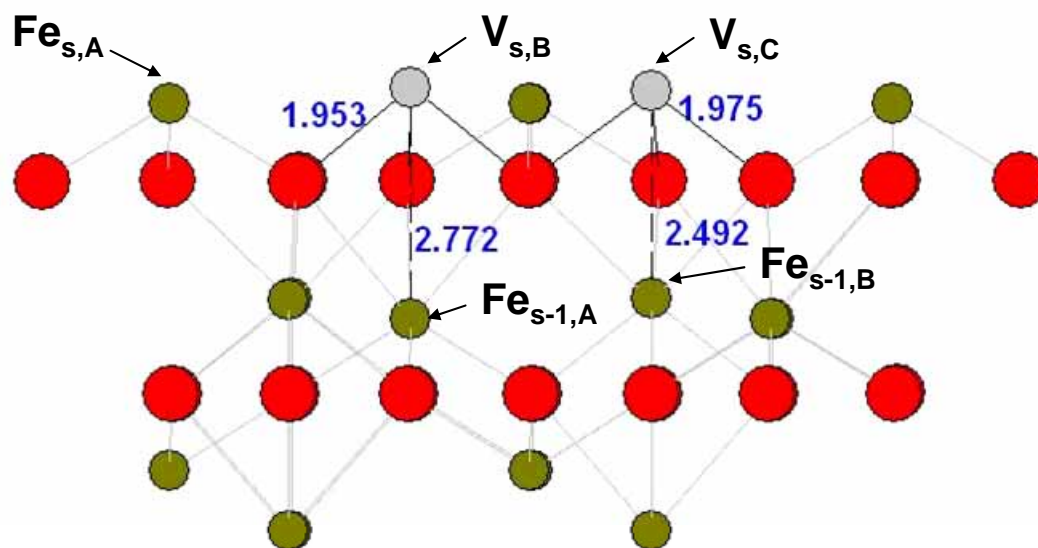
Figure 3.8 Two V (V$_{BC}$) atoms adsorbed on a Fe-terminated Hematite (0001) surface.

As shown in Figure 3.8, V_B and V_C are basically located in the plane which $Fe_{s,A}$ atoms define; the heights to this plane are only 0.1 Å for V_B and 0.05 Å for V_C, respectively. Furthermore, two V adatoms are of noticeable close distances to Fe_{s-1} atoms beneath (noted as $Fe_{s-1,A}$ and $Fe_{s-1,B}$).

The cluster-based electronic structure and bonding analysis of 1 ML V_{BC}/Fe-termination is given in Table 3.7.

Table 3.7 Electronic structure and bonding information for 1ML V_{BC}/Fe-terminated interface

	Atoms	Mulliken Population	Charge	Bond order /Bond length (Å)
After	V_B	$3d^{2.73}4s^{0.53}4p^{0.76}$	0.98	V_B-$Fe_{s-1,A}$: 0.02/2.77
	$Fe_{s-1,A}$	$3d^{5.56}4s^{0.04}4p^{0.06}$	2.34	V_B-O_s: 0.07/1.95
	O_s	$2s^{1.95}2p^{5.55}$	-1.50	V_C-$Fe_{s-1,B}$: 0.07/2.49
	V_C	$3d^{2.75}4s^{0.47}4p^{0.66}$	1.11	V_C-O_s: 0.09/1.98
	$Fe_{s-1,B}$	$3d^{5.56}4s^{0.06}4p^{0.08}$	2.30	V_B-$Fe_{s,A}$: 0.17/2.90
	$Fe_{s,A}$	$3d^{5.54}4s^{0.24}4p^{0.24}$	1.98	V_C-$Fe_{s,A}$: 0.16/2.90
	$Fe_{s-1, others*}$	$3d^{5.49}4s^{0.04}4p^{0.04}$	2.44	
Before (clean surface)	$Fe_{s-1,A}$	$3d^{5.43}4s^{0.02}4p^{0.03}$	2.52	n/a
	O_s	$2s^{1.98}2p^{5.47}$	-1.57	
	$Fe_{s-1,B}$	$3d^{5.45}4s^{0.04}4p^{0.04}$	2.47	
	$Fe_{s,A}$	$3d^{5.53}4s^{0.17}4p^{0.16}$	2.33	
	$Fe_{s-1,others*}$	$3d^{5.45}4s^{0.02}4p^{0.02}$	2.49	

Note: others* refers to other Fe_{s-1} atoms except $Fe_{s-1,A}$ and $Fe_{s-1,B}$ denotes in Figure 3.8.

Compared to 0.5 ML V/Fe-termination, the adsorbed V atoms are much more reduced in the Mulliken scheme (V_B: from 1.91e to 0.98e, V_C: from 1.91e to 1.11e). The bond orders of V-$Fe_{s,A}$ are 0.17 and 0.16, which are clear indications of direct charge sharing. Even though the V-O_s bond lengths increase by about 0.2 Å compared to the 0.5 ML case, their bond orders hardly change, while the V-Fe_{s-1} charge sharing drops to nearly nothing. These

data clearly indicate the change in dominant bonding interactions, involving V and subsurface Fe when coverage increases from 0.5 ML to 1 ML, while the V-O covalency remains nearly constant.

3.8.4 1 ML V/O3-terminated interface

Two representative 1ML V adsorption on O3-terminated surface are calculated and compared (Figure 3.9). The configuration of (V_{AB}, O3) (Figure 3.9a) is found to be energetically preferred over the (V_{AC}, O3) (Figure 3.9b) with adsorption energy of -7.61 eV compared to -6.66 eV.

In Figure 3.9a, V_B drops below the O_s layer, forming a tetrahedral bonding with three O_s atoms and the $Fe_{s-1,A}$ right below. The distance of V_B–$Fe_{s-1,A}$ is 2.04 Å, much smaller than 2.56 Å in the 0.5 ML V/Fe-termination case, which implies a corresponding much higher charge sharing between V_B and $Fe_{s-1,A}$.
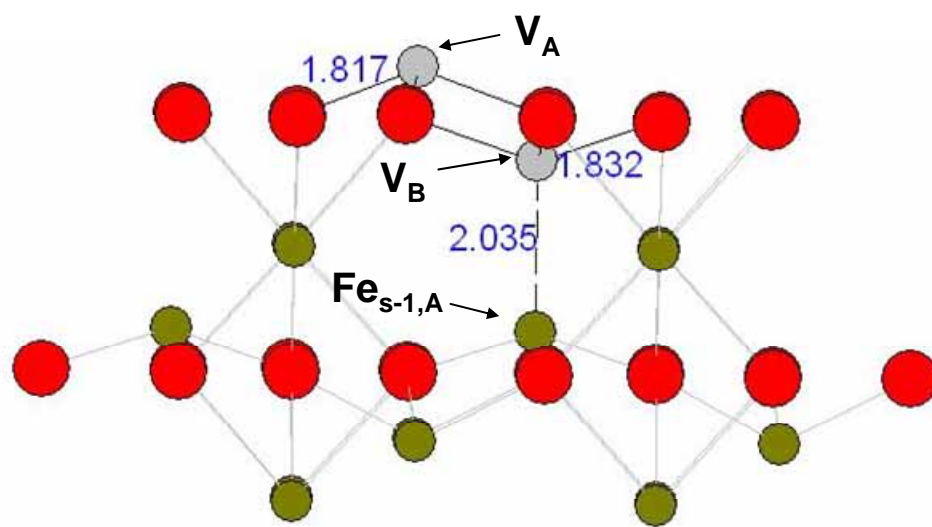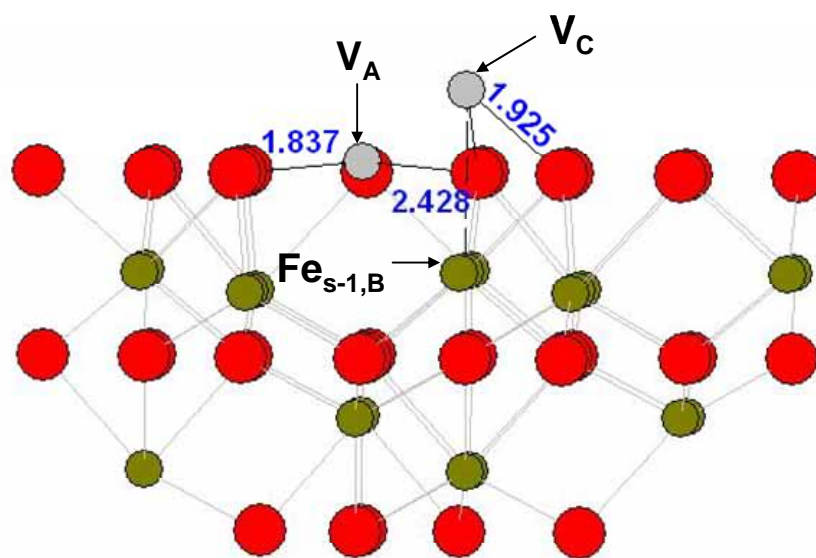
Figure 3.9 Two V (a) V$_{AB}$, (b) V$_{AC}$ atoms adsorbed on O3-terminated Hematite (0001) surfaces.

Table 3.8 demonstrates the extremely high bond order of V_B-$Fe_{s-1,A}$ bond of 0.79e; this strong interaction greatly reduces the charge sharing between V_B and O_s. Meanwhile, the bond order of V_C-$Fe_{s-1,B}$ is much smaller, largely due to its longer bond of 2.43Å.

Table 3.8 Electronic structure and bonding information for 1ML V_{AB},V_{AC}/O3-terminated interface

		Atoms	Charge	Mulliken Population	Bond order /Bond length (Å)
(V_{AB}, O3)	After	V_A	2.49	$3d^{2.44}4s^{0.03}4p^{0.04}$	V_A-O_s: 0.33/1,82
		O_s	-1.25	$2s^{1.98}2p^{5.26}$	V_B-$Fe_{s-1,A}$: 0.79/2.04
		V_B	1.93	$3d^{2.55}4s^{0.19}4p^{0.33}$	V_B-O_s: 0.18/1.83
		$Fe_{s-1,A}$	1.49	$3d^{5.73}4s^{0.29}4p^{0.49}$	
		$Fe_{s-1,others}$	2.48	$3d^{5.42}4s^{0.06}4p^{0.03}$	
	Before	O_s	-1.00	$2s^{1.99}2p^{4.78}$	n/a
		$Fe_{s-1,A}$	2.52	$3d^{5.49}4s^{0.06}4p^{0.08}$	
		$Fe_{s-1,others}$	2.52	$3d^{5.45}4s^{0.01}4p^{0.02}$	
(V_{AC}, O3)	After	V_A	2.28	$3d^{2.56}4s^{0.10}4p^{0.06}$	V_A-O_s: 0.34/1.84
		O_s	-1.41	$2s^{1.97}2p^{5.44}$	V_C-$Fe_{s-1,B}$: 0.07/2.43
		V_C	2.18	$3d^{2.55}4s^{0.19}4p^{0.33}$	V_C-O_s: 0.31/1.93
		$Fe_{s-1,B}$	2.30	$3d^{5.58}4s^{0.04}4p^{0.08}$	
		$Fe_{s-1,others}$	2.42	$3d^{5.51}4s^{0.03}4p^{0.04}$	
	Before	O_s	-1.08	$2s^{1.99}2p^{5.09}$	n/a
		$Fe_{s-1,B}$	2.44	$3d^{5.53}4s^{0.01}4p^{0.02}$	
		$Fe_{s-1,others}$	2.46	$3d^{5.53}4s^{0.03}4p^{0.02}$	

In summary, geometry relaxation and adsorption energy calculations of V adsorption on hematite (0001) surfaces have been carried out. Table 3.9 lists the adsorption energies including some additional cases not discussed here [31].

Table 3.9 Adsorption energy summary of V on Hematite (0001) surface

Adsorption site		E_{ad} /V atom (eV)
0.5 ML	(V_B, $Fe_{s,A}$)	-6.20
	(V_A, O_s)	-9.91
1 ML	(V_{AB}, $Fe_{s,C}$)	-4.98
	(V_{BC}, $Fe_{s,A}$)	-4.96
	(V_{AC}, $Fe_{s,B}$)	-4.95
	(V_{AB}, O_s)	-7.61
	(V_{AC}, O_s)	-6.66
	(V_{BC}, O_s)	-7.40

3.8.5 Core level shifts

Experimental core level shifts obtained by XPS are generally used as a measure of the atomic valence state. It is sometimes important to distinguish between initial state and final state (core hole) relaxation effects. In order to evaluate the importance of final state screening effects, the V core level shift of 38-atom (0.5ML V/Fe-terminated surface) and 50-atom (O-0.5ML V/Fe-terminated surface) molecular clusters centered on V_B of the surface are compared, which allow for both core and valence electron relaxation in an optimized numerical LCAO basis. Ground state (GS, $V^{3.0+}$), Slater transition state (TS, $V^{3.5+}$), and the full core hole excited state (ES, $V^{4.0+}$) are calculated for comparison of energy levels (Table 3.10).

Table 3.10 Fermi energy, E_{2p} eigenvalues and total energy of ground state, transition state and excited state model of V_B adsorbed on Fe-terminated surface, with and without oxygen co-adsorption.

		E_F (eV)	E_{2p} (eV)	Below E_F (eV)	E_{total} (eV)
0.5ML_V_B_Fe$_A$	**GS** $V^{3.0+}$	9.924	Low:-483.46	-493.38	0.00
			High:-483.27	-493.19	
	TS $V^{3.5+}$	8.428	Low:-502.24	-510.67	302.86
			High:-499.77	-508.20	
	ES $V^{4.0+}$	6.925	Low:-520.82	-527.75	620.69
			High:-515.50	-522.43	
O_0.5ML_V_B_Fe$_A$	**GS** $V^{3.0+}$	9.427	Low:-485.29	-494.72	0.00
			High:-485.04	-494.47	
	TS $V^{3..5+}$	7.943	Low:-503.25	-511.19	302.86
			High:-501.11	-509.05	
	ES $V^{4.0+}$	6.466	Low:-522.47	-528.94	620.69
			High:-514.66	-521.12	

Note: E_{total} of TS and ES are referred to Ground state (GS), which is set to be "0.00" eV.

The large quantitative importance of charge transfer from neighbors and the resulting screening are immediately apparent; e.g., for the non-oxidized case, the total energy difference (LDA, non-relativistic) for $V^{3.0+}$ $(2p^6)$ → $V^{4.0+}$ $(2p^5)$ ionizing transition is 620.69 eV, while the experimental $2p_{3/2}$ photoelectron binding energy (BE) appears at ~515.3 eV corresponding to a 3+ oxidation state [30]. The cluster transition state calculations for this case give an ionization band of width ~2.5 eV (due to exchange coupling of the core hole to the valence states) centered at ~509.44 eV. More accurate results would presumably require a relativistic treatment of the $2p_{3/2}$, $2p_{1/2}$ sub-bands. The difference between two TS represents the level shift between V_B/Fe$_A$ and O/V_B/Fe$_A$ (1/3 ML O) environments, which is 0.52-0.85 eV for the two possible core spin orientations. The (initial state only) VASP calculations result in the core level shift estimate of 0.78 eV [31], suggesting that while final state screening is not of over-riding importance, it can contribute

several tenths of eV to the observed values.

3.9 Discussion and conclusions

This section investigated geometric and electronic properties of four V/Hematite systems: (1) 0.5 ML V adsorption on an ideal Fe-terminated Hematite (0001) surface; (2) 0.5 ML V adsorption on an ideal O3-terminated surface; (3) 1 ML V adsorption on a Fe-terminated surface; and (4) 1 ML V adsorption on an O3-terminated surface. These V/Hematite interfaces are regarded as the initial stages of V interaction with Hematite (0001) surfaces, since after Vanadium deposition, the interfaces may undergo oxidation-reduction reactions when ambient conditions change, as Kim has proposed [30].

In the experimental work of Kim et al. [30], X-ray standing wave (XSW) analysis and X-ray photoelectron spectroscopy (XPS) were used to trace the electronic and atomic-scale structural changes of a supported vanadium oxide system at different stages of its oxidation-reduction cycle. The V/Hematite system shows reversible changes through the oxidation-reduction cycle characteristic of catalytic behavior. The present thesis doesn't go very far to discuss oxidation state and adsorption geometry of the vanadium on hematite support in detail, but see Jin's paper [31] for details of 1/3, 2/3 and 1 monolayer O (1 O, 2 O and 3 O, respectively) adsorbing on various terminated surfaces. In that DFT work, strong vanadium-oxygen and vanadium-iron interactions at different scenarios are supported by large bond orders and charge density; V generally functions as an electron donor, causing nearby Fe to be partially reduced; the exposure of the V/hematite system to

atomic O usually causes V to further be oxidized and surface/near surface Fe to be re-oxidized.

In this initial study of the reduced V/Hematite interface, for an ideal single Fe-terminated hematite surface, site B is found mostly preferred for 0.5 ML V deposition; and for O3-terminated surfaces, site A. These results accord with chemical intuition; since the preferred sites are less close to the Fe beneath than site C, they can reduce the Coulomb repulsion from subsurface Fe to the greatest extent. This conclusion is also supported by results for 1ML V deposition, as (V_{AB}, $Fe_{s,C}$) and (V_{AB}, O_s) exhibit lowest adsorption energy on each type of terminated surface. However, there is an apparent disagreement between this theoretical prediction and experimental measurement. Kim et al. [30] would like to suggest that Vanadium in the 3+ oxidation state occupies A and C sites; while highly oxidized Vanadium ions (5+) occupy bulk hematite A and B sites. This discrepancy lies beyond computational error estimates due to the large energy difference (~ 1eV). This difference might be caused by the complexity of the surface region structure. In an ideal bulk model, the distance from site C to the nearest underlying Fe is 2.25 Å. As proved in scenarios shown in Figures 3.9a and 3.9b, the short V_B-Fe_A bond of 2.04 Å causes its bond order to be extremely high, 0.79e, while a longer V_C-Fe_B bond of 2.43 Å causes the bond order to be nearly nothing, 0.07e. There is no guarantee that V_C will not directly interact with Fe_B beneath. However, in order to compete with other energetically favorable sites, it must overcome the higher Coulomb energy barrier to stabilize on the surface. The defect sites on the surface or subsurface may be an aid; e.g., a missing $Fe_{s-1,B}$ will probably favor the V_C occupation. This question awaits further research, especially in defect study. Since

XSW measurements only reveal orientations and heights relative to subsurface bulk structure, while giving little information on the arrangements of surface-region structure, it can not exclude the possible existence of any defects, or non-stoichiometric atomic arrangements.

Theoretical electronic analysis also sees that the effect of V adsorption on Hematite (0001) is quite localized. While in several cases, the Fe atoms beneath adsorbed V atoms are heavily oxidized, the other subsurface Fe atoms keep immune to effects of V adsorption. The adsorption energy calculations find that V adsorption on an O3-terminated surface will result in the largest energy gain, but the relative energy depends very much on the adsorption configuration. Kim et al. [30] found that surface sites A, B, and C can be 60% occupied for the reduced surface. This is quite close to the 1ML cases studied here. So, the adsorption model of (V_{AB}, O_s), which is of noticeably strongest V-Fe interaction, is most preferred over other combinations.

CHAPTER 4

INITIAL STAGES OF HYDRATION AND ZN OCCUPATION ON

HYDROXYAPATITE (0001) SURFACES

4.1 Introduction

Hydroxyapatite (HAP), with chemical formula $Ca_{10}(PO_4)_6(OH)_2$, is widely used in the repair, reconstruction, and replacement of diseased or damaged parts of bones and teeth [1-4]. HAP also claims attention as an environmental adsorbent of metals and toxic waste removal due to its porous nature and highly active ion exchange character [5,6]. It has been shown from both experiments and theoretical calculations that the (0001) surface of HAP is the dominant interface with respect to vacuum and aqueous phases [7]. Because the surface of HAP is of great importance for understanding of dissolution [8] and interfacial interactions [9] between the crystal and ambient phases, some efforts have been made to investigate the relevant surface properties. In experiments, multiple studies have been carried out using several characterization techniques [10] to identify the HAP biocompatibility [11], adhesion properties [2] and synthetic conditions [12]. Meanwhile, computational methodology has shown its strength in interpreting electronic structure, charge distribution and atomic configuration by the *ab initio* Hartree-Fock method [13], molecular dynamics simulation [14], semi-empirical [15] and density functional theory (DFT) [16,17].

Zhu and his co-workers studied vacuum-surface energetics of HAP using the DFT approach, finding out that the relaxation of the slab surfaces has an apparent effect on surface energy. They also proposed the relative order of the morphological importance of different (*hkl*) surfaces [18]. Zahn and Hochrein investigated energetic preference of HAP with bulk substitutional defects in order/disorder arrangement of OH⁻ ions, concluding that the

HO⁻…HO⁻ arrangement is most favorable [19]. De Leeuw drew the similar conclusions using DFT [20]. Ion exchange properties have also been studied experimentally [21,22]. The manner in which some divalent cations in aqueous solution are removed by synthetic HAP has been probed by using both batch and column methods. The ranking of the cations according to amount exchanged is found to be $Cd^{2+} \approx Zn^{2+} > Ni^{2+} > Ba^{2+} \approx Mg^{2+}$, suggesting that HAP has a selectivity for metallic cations and can be employed as a new inorganic cation-exchanger for recovering valuable ions in waste water [5]. There are several other theoretical papers reporting studies about defects, structures, and adsorptions on HAP surfaces or near-surface region [23,24], but they have never treated HAP as a hydrated material for ion exchange. In a recent work by Zahn and Hochrein, molecular dynamics simulations were performed to study the hydration process on HAP (0001) surface [14]. However, until now, no report on using first principles methods to study this process has been found.

There has also been much interest in the chemistry of metal ions as substituents in HAP, especially in the presence of water. In the biological context, it has been established that the uptake and release of Zn in the body is strongly mediated by the bone reservoir [25]. Furthermore, Zn bound HAP, denoted as Zn/HAP, is found to be very effective as a co-catalyst together with a Lewis base in coupling of CO_2 and epoxides [26]. So far, theoretical interpretation of the chemistry of Zn ions in HAP seems to be limited to a study of bulk substitution for Ca [27].

A DFT study on the surface of low-coverage hydrated HAP with respect to surface structure

and adsorption energy will be described in the first part of this chapter. In the second part, the preferential occupation of Zn in the HAP surface region will be reported, through which a better understanding of the geometry, energetics and the corresponding substitution mechanism is expected to be achieved.

4.2 Theoretical approach

4.2.1 Computational methodology

Band structure calculations are carried out using the first principles periodic slab DFT program VASP (Vienna *ab initio* simulation package) [28] making use of pseudopotentials with a plane wave basis [29] (see chapter 1.2.2 for more background). The exchange-correlation potential is chosen as the spin-polarized generalized gradient approximation (SP-GGA) of PW91, to calculate geometry relaxation and surface energy. The representation of ion core-electron interactions is performed using the projector augmented wave method (PAW) [30]; the detailed implementation was that of Kresse and Joubert [31]. Automatically generated Monkhorst-Pack grids [32] are used to carry out Brillouin zone integrations. For each (1x1) unit cell, a 2x2x1 k-points mesh is used for geometrical relaxation and energy calculations, and energy cutoff of a plane wave basis set is set to be 450 eV. In geometrical relaxation, a Gaussian smearing finite temperature broadening method is used, with width $\sigma = 0.1$eV. For energy calculations, the tetrahedron method is adopted to perform Brillouin zone sampling. By making a series of calibration runs, the total energy is found to be converged within 0.03eV/unit cell (<0.01%).

Through bulk calculations, the lattice constants a = b = 9.42 Å and c = 6.87 Å are obtained, which are found to be within 0.15% of the experimental lattice values of a = b = 9.43 Å, and c = 6.88 Å [33]. The slabs with different configurations then are relaxed to determine the most stable termination; then, the surfaces without or with varying numbers of adsorbed H_2O are fully relaxed. The vacuum gap between two neighboring slabs is set to be around 13 Å, a distance large enough to avoid interference from each other.

4.2.2 Unit cell geometry

Hexagonal $Ca_{10}(PO_4)_6(OH)_2$ crystallizes in space group $P6_3/m$ [27]. A primitive unit cell contains 44 atoms (Figure 4.1; some side- and corner- atoms shown are shared by different unit cells).

Considering different sites which Ca and Oxygen ions occupy, the HAP molecular formula can be rewritten as $Ca(I)_4Ca(II)_6(PO_aO_b(O_c)_2)_6(O_HH)_2$. As shown in Figure 4.1, Ca ions are situated in two different sites, denoted as Ca(I), Ca(II), respectively. According to the definition that effective Ca-O bond lengths are less than 3 Å, Ca(I) is found to be coordinated to nine Oxygen ions ($3O_a$, $3O_b$, $3O_c$) from six different phosphate tetrahedral groups and Ca(II) is 7-fold coordinated by six Oxygen ions of five phosphate groups and one from Hydroxyl group ($1O_a$, $1O_b$, $4O_c$, $1O_H$). The $Ca(I)O_9$ polyhedron is much bigger than the $Ca(II)O_7$ polyhedron in volume (30 $Å^3$ to 22 $Å^3$) [34] (Figures 4.2a, 4.2b). The Ca(II) ions are distributed in a hexagonal fashion so that they form channels, with each centering an array of hydroxyl groups (Figure 4.2c).
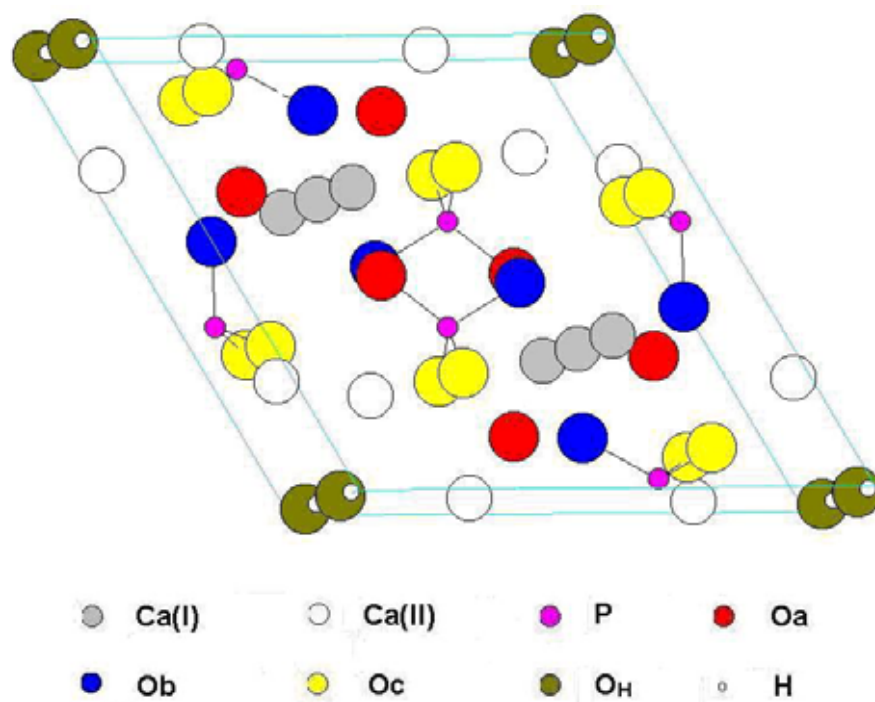
Figure 4.1 Hydroxyapatite (1x1) unit cell.

a

b

c
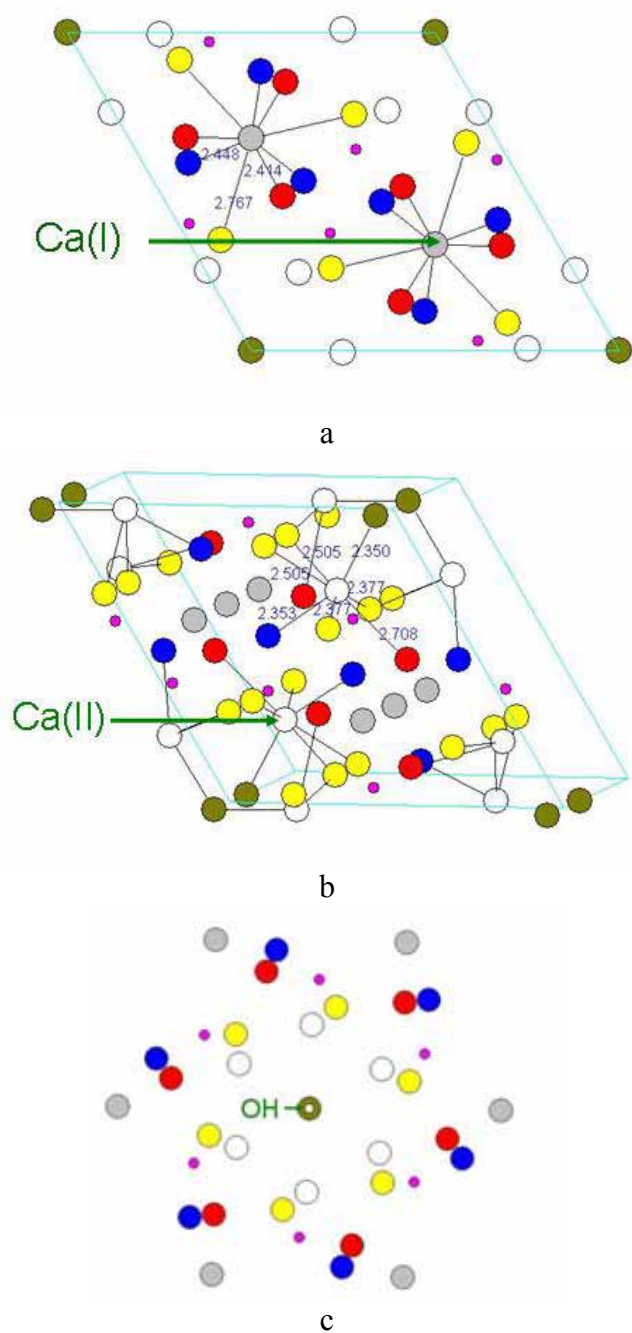
Figure 4.2 HAP molecular structure in detail.

(a) Ca(I) polyhedron; (b) Ca(II) polyhedron; (c) Hydroxyl hexagonal channel, looking along the c-axis.

4.3 Results and discussion

4.3.1 Clean dry surfaces

Compared with the (1000) crystallographic direction of HAP, the polarity at the (0001) direction is stronger, which could result in more structured-water layers [35]. Considering that the (0001) surfaces are the predominant form of interfaces of teeth to saliva [14], different terminated (0001) surfaces are relaxed as a pretreatment step to hydration. This relaxation is based on assumptions that there is only one kind of termination on the surface and the surface phosphate groups are kept intact. According to Posner, the numbers and orientations of the surface polar (P-O…H) groups will determine the adsorption strength on apatite surfaces and will be directly related to those of water molecules available through hydrogen bonding [36].

According to this just described assumption, three HAP (0001) terminations are taken into account. They are called zero-Ca(I) (Figure 4.3a), single-Ca(I) (Figure 4.3b) and double-Ca(I) (Figure 4.3c) terminations, respectively, for there are different numbers of Ca(I) ions exposed to the vacuum. The termination with a single Ca(I) ion on the top is found to be energetically most stable (with energy gain of 1.68 eV compared to zero-Ca(I) termination and a much larger value of 13.03 eV compared to double-Ca(I) termination), so it is selected as the substrate system for hydration.
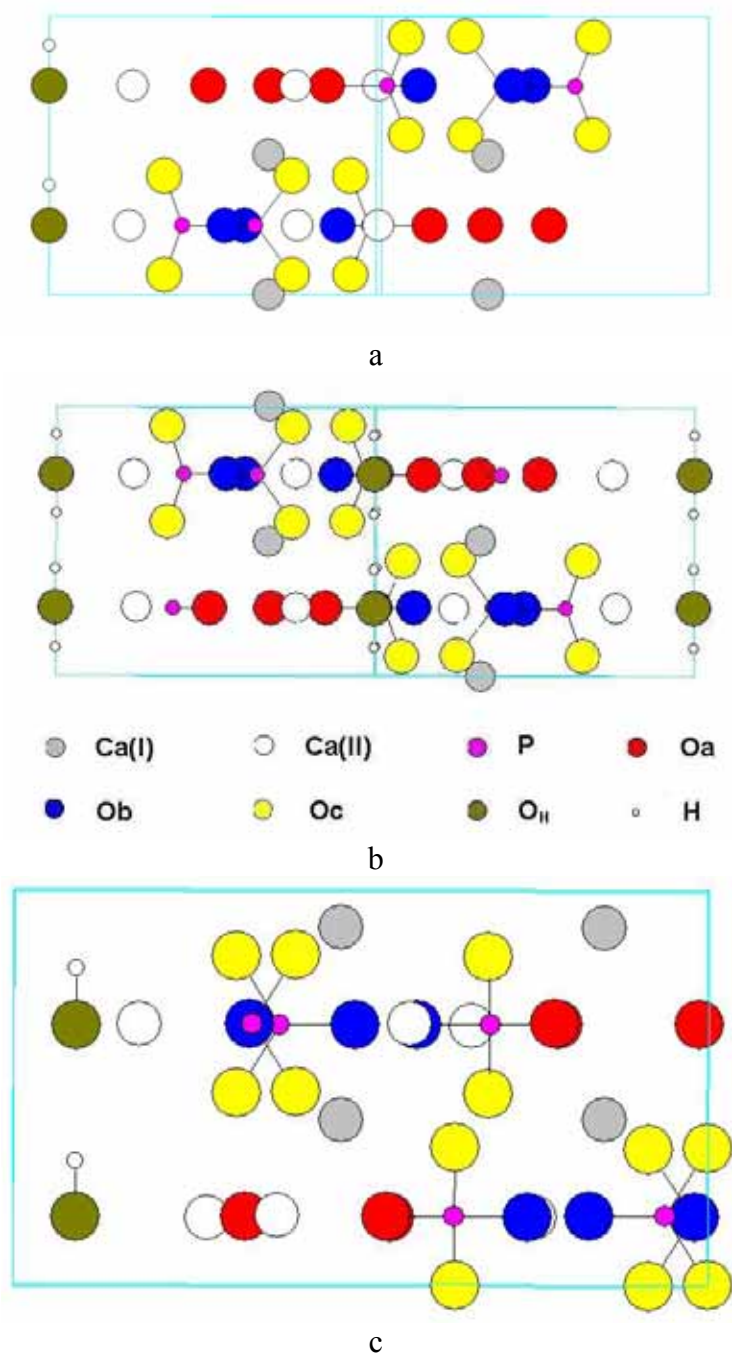
Figure 4.3 HAP typical terminations on (0001) surface.

(a) Zero-; (b) single-; (c) double- Ca (I) terminated surfaces.

4.3.2 Adsorption of water molecules

The relaxation of geometrical structure performed by VASP shows that for most atoms within the unit cell boundary, the interlayer distances don't noticeably change, and the shift of the positions of the ions within the plane parallel to the surface is hardly significant. The exceptions are that: (1) the surface Ca(I) is pulled down during the surface contraction, so the slab thickness (defined as the vertical distance within a 1x1x1 cell between two Ca(I) terminal ions, one on the top, the other at the bottom) is reduced by 11.2%; (2) the distance between the two hydroxyl groups is increased by 10.1% (Figure 4.4).

H_2O molecules are added to the single-Ca(I) terminated surface in a step-wise fashion to produce a hydrated HAP (0001) surface. Although a unit cell with surface area of 76.85 $Å^2$ (a parallelogram with sides of 9.42 Å) is relatively spacious, perhaps capable of holding 15 H_2O molecules, only 6 H_2O molecules are sequentially added to this surface as an initial probe to the comprehensive picture of hydration.
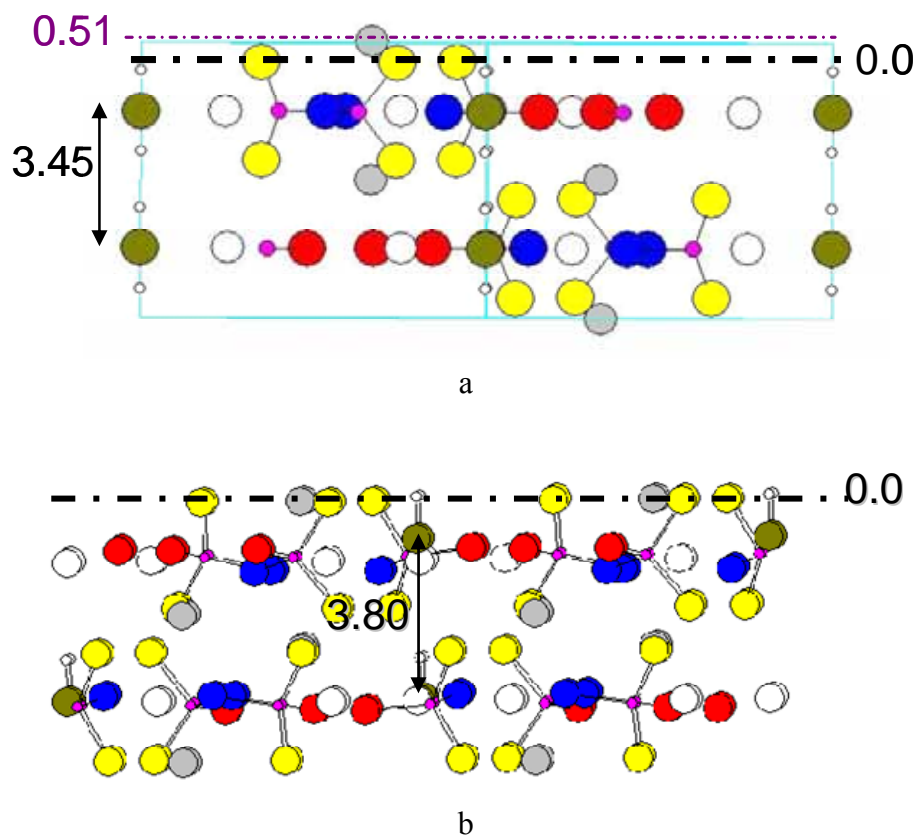
Figure 4.4 Surface relaxation of a single-Ca(I) terminated HAP.

(a) before relaxation; (b) after relaxation.
The "surface plane" labeled "0.0" above is defined by positions of terminal O_c atoms.

4.3.2.1 Geometry

Figure 4.5 gives the resulting configurations after adsorbing from one to six H_2O molecules on the HAP (0001) surface.

The adsorption of H_2O molecules is tried at different surface sites in order to find the energetically most favorable configuration. The relaxed structures and some critical bond lengths can be found in Figure 4.5. Here are some conclusions: First, H_2O has neither a tendency to fall into the hexagonal channel nor to form any hydrogen bonds (H-bonds) with the surface Hydroxyl group. This may be surprising since the (OH) channel is considered the principal route for ionic diffusion into the solid and the expulsion of water upon calcination. Second, the surface structure of HAP responds very little to the water adsorption, both horizontally and vertically, except that the terminal Ca(I) atom is pushed up by 6.1%, partially restoring its bulk position (Figure 4.6). Third, when H_2O coverage is low, say 1 or 2 H_2O molecules adsorbed per unit cell, O_{ad} in H_2O tends to form Ca-O bonds of 2.4 - 2.6 Å in length, but as coverage continues to increase, it becomes more difficult for additional H_2O to interact directly with surface Ca. These H_2O will loosely float on the surface, or begin to form an H_2O film. The exception to this "rule" is found in Figure 5e, where 3 H_2O forms only 2 O-Ca bonds, while in 5g, 5i, and 5k, three O-Ca bonds are formed. Fourth, some protons of the H_2O molecules form H-bonds with Oxygen in surface phosphate groups, showing that the phosphate groups are susceptible to protonation. This can be viewed as the initial step of acidic corrosion of Hydroxyapatite according to the equation,

$$Ca_{10}(PO_4)_6(OH)_2 + 8H^+ \rightarrow 10Ca^{2+} + 6(HPO_4)^{2-} + 2H_2O \qquad (4.1)$$

However, although incipient H-O$_{phosphate}$ bonds are seen, there is no sign of H-O bond dissociation in H$_2$O and P-O bonds weakening at such low coverage.

a

b

c

d

e

f
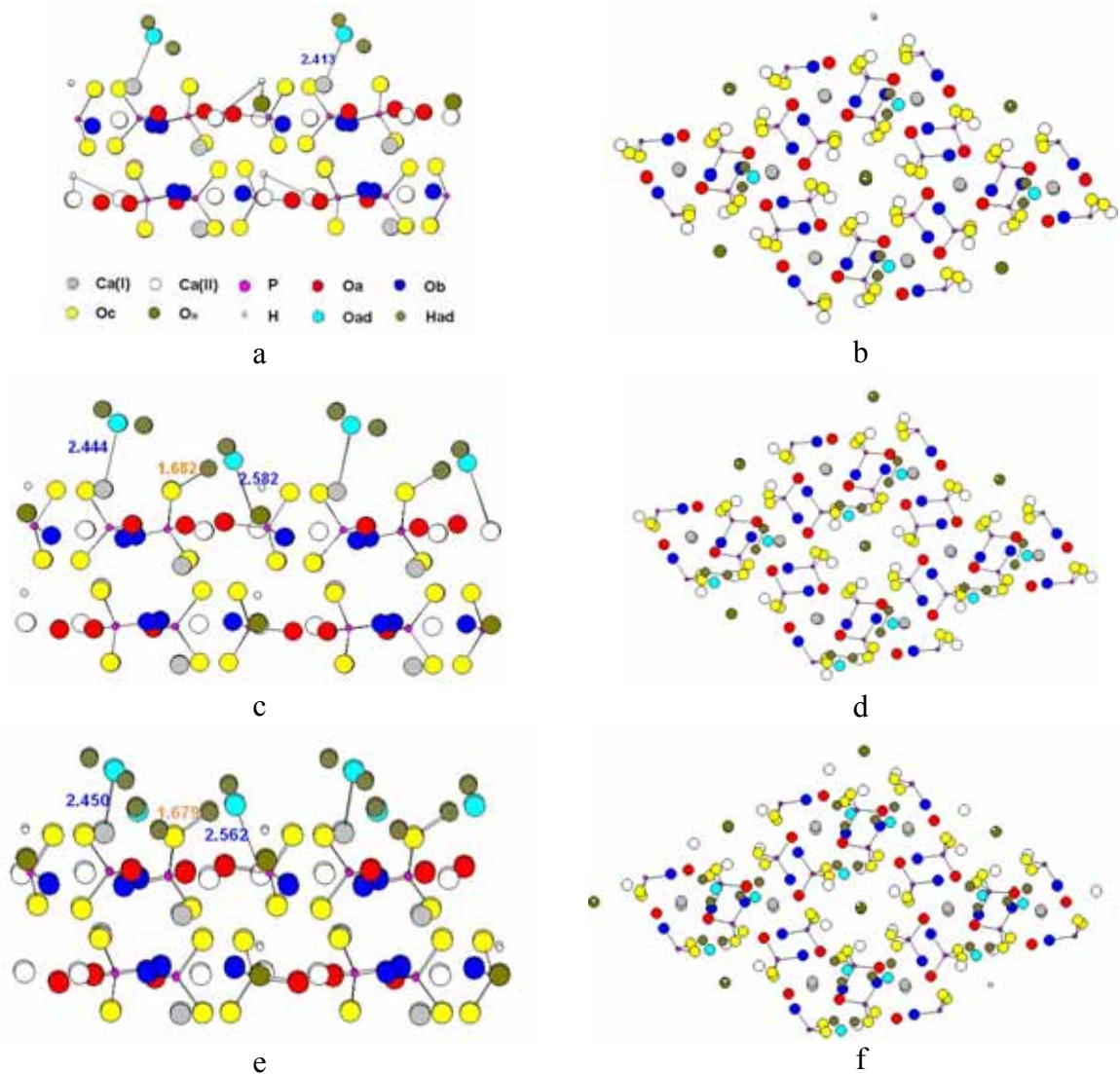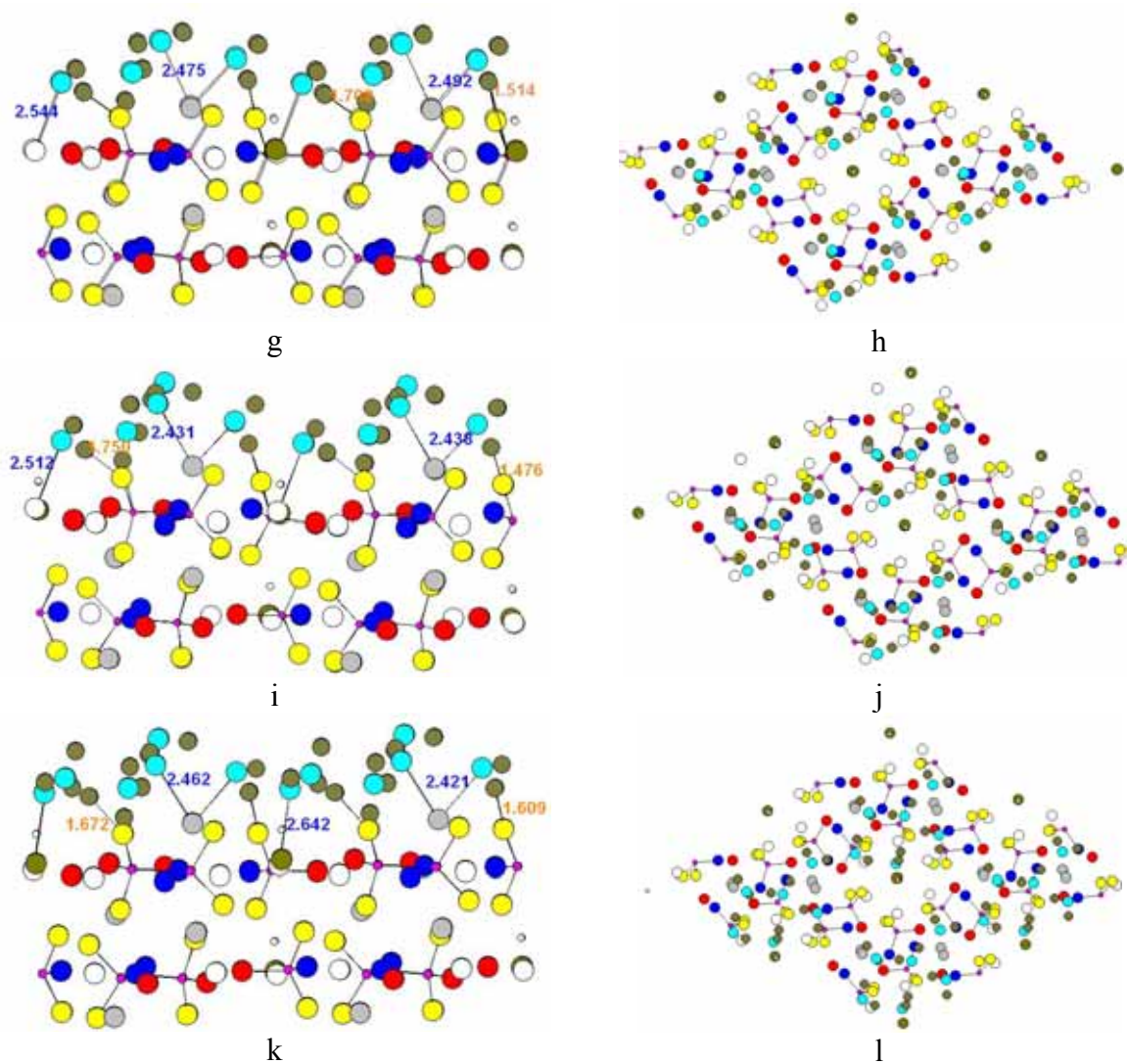
Figure 4.5 Hydration of (2x2x1) HAP single-Ca(I) (0001) surface.

(a) One H_2O (side view); (b) One H_2O (top view);
(c) Two H_2O (side view); (d) Two H_2O (top view);
(e) Three H_2O (side view); (f) Three H_2O (top view);
(g) Four H_2O (side view); (h) Four H_2O (top view);
(i) Five H_2O (side view); (j) Five H_2O (top view);
(k) Six H_2O (side view); (l) Six H_2O (top view).
The numbers in blue denote bond lengths of O_{ad} in the adsorbed H_2O with surface Ca ion;
the numbers in orange denote bond lengths of H_{ad} with surface O ion.

4.3.2.2 Adsorption energy

Adsorption energy is defined as $E_{ad} = E_{surface-nH_2O} - nE_{H_2O} - E_{surface}$, where n is the number of the adsorbed H_2O. A negative E_{ad} means adsorption is energetically favored. For better interpretation, "Adsorption Energy *per* H_2O (E_{perH_2O})" is also reported (Figure 4.7), which is defined as $E_{perH_2O} = E_{ad} / n$, see Table 4.1.

Table 4.1 The calculated adsorption energies of H_2O on a HAP (0001) surface

	Number of H_2O					
	1	2	3	4	5	6
E_{ad} (eV)	-0.78	-1.25	-2.16	-2.44	-3.27	-3.99
E_{perH_2O} (eV)	-0.78	-0.63	-0.72	-0.61	-0.65	-0.67

In Table 4.1, the average adsorption energy of ~0.7 eV/molecule demonstrates that the single-Ca(I) terminated HAP (0001) surface is a good substrate for H_2O adsorption. Although the curve in Figure 4.7 is zigzag when H_2O coverage is low, it becomes fairly "flat" as four more H_2O molecules are added to the surface. Figure 4.6 graphically depicts how H_2O molecules form layers over the HAP (0001) surface. Surface "0.0" is defined by the plane of O_c ions from the surface phosphate groups. Most H_2O molecules (5, in the figure) gather near the height of 1.6Å above this surface, while 1 H_2O floats as high as 3.2 Å from the surface plane. Figures 4.6 and 4.7 show when more water molecules are adsorbed, they will not interact directly with the HAP surface layer, but will lie on the already-formed water film and gain much more mobility. The results found here confirm

Zahn and Hochrein's semiempirical molecular dynamics study for the formation of H_2O

layers, showing decreasing of mobility in proximity of the apatite surface [14].
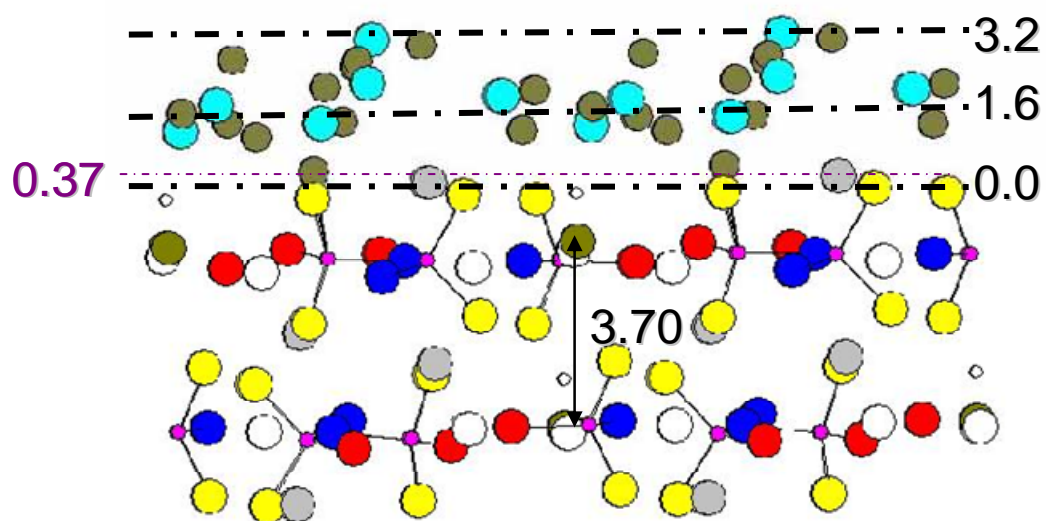
Figure 4.6 Water on the (0001) surface (six H_2O per unit cell); side view.
The first adsorption layer is seen at a height of ~1.6Å.
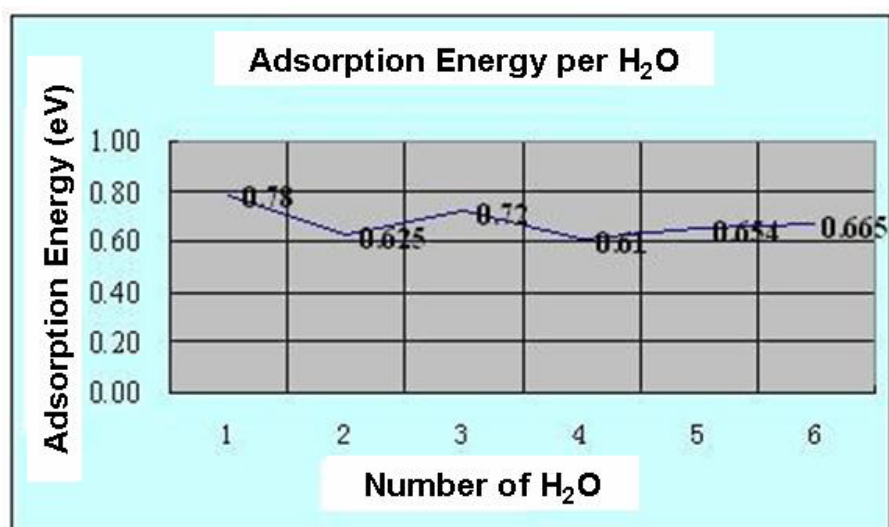
Figure 4.7 Adsorption energy per H_2O, on single-Ca(I) terminated HAP.

4.3.3 Substitution and occupation of Zn on metal sites

4.3.3.1 Zn on Ca sites

Substitution of surface cations is considered by placing Zn on the surface Ca site. Periodic slab DFT calculations are performed to determine the total energy change upon substitution. Figures 4.8a and 4.8b show the relaxed surface structure with some critical bond lengths denoted.

Since the Ca(I) at the bottom of the slab (pointed out by an arrow) is essentially in the symmetric position equivalent to Zn, its bond lengths with some neighbors are also measured. Figure 4.8a clearly shows that the Zn-X bonds shrink significantly compared with the corresponding Ca(I)-X bonds. The top view in Figure 4.8b graphically shows that after substitution, Zn basically stays at the position of the original Ca(I) site. The ratio of Zn-X bond lengths to the Ca(I)-X bond lengths, $R_{Zn-X}/R_{Ca(I)-X}$, is calculated according to the data in Figure 4.8a. The results fall into the range of 89.2% to 96.2% (Table 4.2). This nearly proportional change proves that the substitution of Zn on Ca(I) site causes the shrinkage of the $M(I)O_9$ polyhedron (M = Zn, Ca).

Table 4.2 Bond lengths and percentage for Zn substitution on a Ca(I) surface site

(Å)	Zn	Ca(I)	R_1 %
$M-O_b$	2.317	2.409	96.2
$M-O_c$	2.180	2.444	89.2
$O_b-Ca(I)$	2.515	2.666	94.3
$M-Ca(I)$	3.194	3.495	89.8

Note: $R_1 = 100 \times \dfrac{R(Zn-X)}{R(Ca(I)-X)}$.

a

b

c
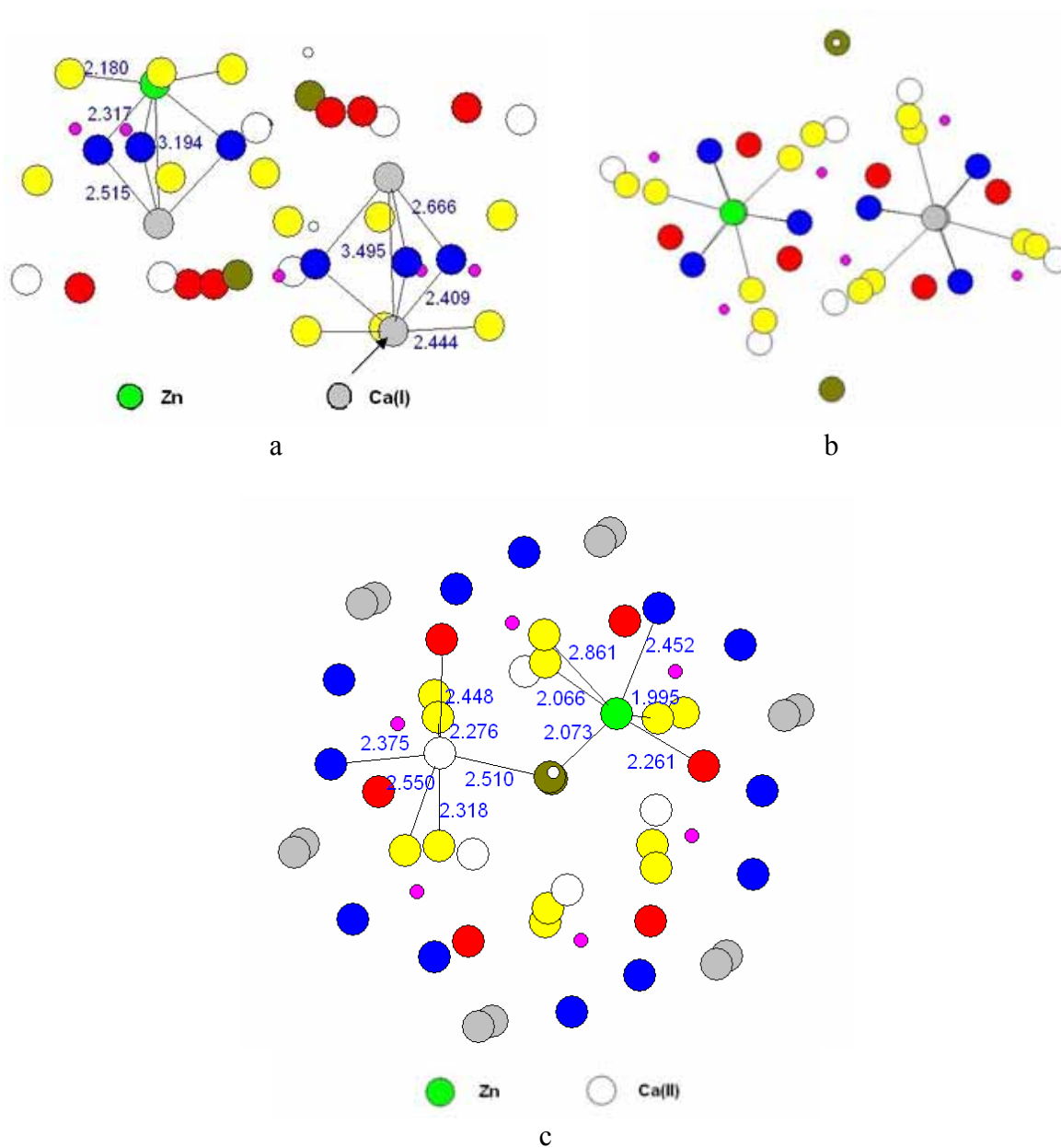
Figure 4.8 Zn substitution on Ca sites I and II of HAP (0001).

(a) Zn substitution on Ca(I) (side view); (b) Zn on Ca(I) (top view); (c) Zn on Ca(II) (top view). Some critical bond lengths are indicated.

Figure 4.8c presents Zn substitution for one of three surface Ca(II) cations. For better visualization, the hexagonal hydroxyl channel is also included.

In Figure 4.8c, the bond lengths associated with Zn and with one of the surface Ca(II) ions on the symmetric site are denoted. The Zn ion is observed to move toward the Hydroxyl group by about 0.5 Å, accompanied by changes in the bond lengths of the MO_7 polyhedron. Table 4.3 gives the bond lengths and calculated percentage changes.

Table 4.3 Bond lengths and percentage changes for Zn on a Ca(II) surface site

(Å)	Zn	Ca(II)	ΔR_2 %
M-O_a	2.261	2.448	-7.64
M-O_b	2.452	2.375	3.24
M-O_c	1.995	2.276	-12.34
	2.861	2.550	12.20
	2.066	2.318	-10.87
M-O_H	2.073	2.510	-17.41

Note: $\Delta R_2 = 100 \times \dfrac{R(Zn-X) - R(Ca(II)-X)}{R(Ca(II)-X)}$.

Different from Zn occupation on the Ca(I) site, substitution Zn at the Ca(II) site causes mainly a shift of the metal ion, but not the shrinkage of the polyhedron. This is probably because metal site (II) is at the edge of the (OH) channel, so having much more freedom to relocate from the original site, while site (I) is fairly compressed within the cluster. The metal ion at site (I) has to overcome a greater energy barrier to shift, so it prefers to stay at the symmetrical center and adjust bond lengths accordingly.

Electronic structure of Zn and Ca in both substitution sites (Table 4.4) is calculated by the cluster method (see Chapter 1.2.3 for program details).

Table 4.4 Charges and Mulliken populations for metal ions at Ca sites I and II

	Site I		Site II	
	Zn	Ca(I)	Zn	Ca(II)
Charge (*e*)	1.15	1.88	1.51	1.86
Mulliken Population	$3d^{9.99}4s^{0.83}4p^{0.04}$	$3s^{2.00}3p^{6.00}3d^{0.06}$	$3d^{9.97}4s^{0.45}4p^{0.07}$	$3s^{2.00}3p^{6.00}3d^{0.08}$

The most notable difference between the nominally divalent cations lies in the Mulliken charge: for site I, a 1.88*e* charge on Ca before substitution and a 1.15*e* on Zn after substitution are found; for site II, there remains 1.86*e* on Ca, but a lesser 1.51*e* on Zn. In both cases, Zn is less ionic than Ca, indicative of the expected more covalent character of the Zn-O bonding.

4.3.3.2 Energetics and site-preferential occupancy

Energies per unit cell regarding the unhydrated surface are displayed in Table 4.5, where

$$E_{total} = E_{system} - E_{isolated\_ions} \quad , \quad E_{sub} = E_{Zn-HAP}^{total} - E_{Ca-HAP}^{total} \quad \text{and} \quad E_{ad} = E_{Zn-HAP}^{total} - E_{vacancy-HAP}^{total} \quad ,$$

negative E_{total} refers to a stable cluster, and negative E_{sub} and E_{ad} indicate thermodynamic favorability.

Table 4.5 Total, substitution and adsorption energies for Zn on Ca ion sites (unhydrated surface)

Energy per cell (eV)	E_{total}	E_{sub}	E_{ad}
HAP-no vacancy	-307.78		
Ca(I) vacancy	-296.89		
Zn on Ca(I)	-302.25	+5.53	-5.36
Ca(II) vacancy	-296.08		

| Zn on Ca(II) | -302.32 | +5.46 | -6.24 |

Table 4.5 shows that ion substitution of Ca^{2+} by Zn^{2+} is endothermic on both types of Ca sites; but occupying both vacancy sites is highly exothermic. Various reports have been published on calcium deficiency in HAP [36,37]; calcium vacancies can be charge-compensated by creating OH^- vacancies, creating PO_4^{3-} vacancies, carbonate ions substituting for phosphate groups, $(HPO_4)^{2-}$ substituting for phosphate groups, and cation sites occupied by other metal cations. Due to the extensive existence of calcium vacancies in HAP surfaces and bulk, this variable stoichiometry will favor HAP as a Zn-releasing material for bones and teeth.

Table 4.6 provides the energies for the six-H_2O hydrated HAP (0001) surface.

Table 4.6 Total, substitution and adsorption energies for Zn on Ca ion sites (hydrated surface)

Energy per cell (eV)	E_{total}	E_{sub}	E_{ad}
HAP-no vacancy	-397.20		
Ca(I) vacancy	-385.47		
Zn on Ca(I)	-391.63	+5.57	-6.16
Ca(II) vacancy	-385.52		
Zn on Ca(II)	-391.89	+5.31	-6.37

Tables 4.5 and 4.6 indicate that Zn prefers to occupy the Ca(II) vacancy site over Ca(I) with an energy gain of 0.88 eV (unhydrated surface) and 0.21 eV (hydrated surface). This can be compared to $\Delta E = 0.05$ eV in bulk [38]. Less energy gain on a hydrated surface implies that the surface modified by adsorbed water seriously affects the potential of this termination. Earlier researchers studying divalent metal impurity occupations have

proposed some rules for preferential occupation sites. Urusov and Khudolozhkin [39] noted that divalent cations larger than Ca^{2+} preferentially occupy the smaller Ca(II) site, whereas divalent cations smaller than Ca^{2+} occupy the Ca(I) site, supposedly because the restricted alignment of the Ca(I) site causes a stronger repulsion. Badraoui et al. suggested judging the preferential occupation according to the electronegativity of the cations [40]. In their proposal, an increase in the electronegativity of the cation will lead to an increase in the covalent character of the bond between the cation and the carboxyl group in metal arachidates. Thus, previous theories tend to explain the preferential occupancy of divalent cations in HAP mainly by arguments based on ionic radius and electronegativity of the cations.

However, results from experiments and the present theoretical work challenge the above mentioned ideas. Table 4.7 summaries the results from experiments of Zhu et al. and this theoretical work.

Table 4.7 Preferential occupancy site for some divalent cations

	Sr^{2+}	Pb^{2+}	Cd^{2+}	Zn^{2+}
Ionic Radius (Å) (Ca^{2+}: 1.00)	1.12	1.19	0.97	0.74
Electronegativity (Ca^{2+}: 0.99)	0.95	2.33	1.69	1.65
Preferential site	II[a]	II[a]	II[a]	II[b]

Note: (a) Experiment [37]; (b) this calculation.

Table 4.7 lists preferential sites of four divalent cations. The proposed rules of ionic radius and electronegativity fail for Sr^{2+}, Cd^{2+} and Zn^{2+}, which uniformly prefer site II regardless of ion size and electronegativity, and only work for Pb^{2+}, which is bigger and more

electronegative than Ca^{2+}. According to the results given in Table 4.7, the site preference of cations is not decided solely by ionic radius or electronegativity, but is very possibly determined by the spatial constraints. Figure 4.8 shows the relaxed configuration after Zn occupies Ca vacancy sites. As mentioned earlier, the occupation on M(I) site causes the shrinkage of the MO_9 polyhedron to 89.2% - 96.2% of the original bond lengths, while the occupation on M(II) site mainly causes a shift of the cation toward the hydroxyl group; so the latter, requiring less energy compensation, is preferred for many divalent cations.

4.4 Conclusions

The initial stages of hydration have been simulated on a single-Ca(I) terminated Hydroxyapatite (0001) surface in step-by-step fashion using periodic slab density functional theory. The prerequisite assumption is that there is only one type of termination on the surface and the surface phosphate groups are kept intact so any dangling bonds on surface ion P can be ignored. Water adsorption is found to be energetically favored on the HAP (0001) surface. At low H_2O coverage, O_{ad} in H_2O prefers to form a Ca-O_{ad} bond with surface Ca cations, but as coverage increases, additional H_2O tends to loosely float on the already-formed water layer. The height of the first water layer is found around 1.6 Å relative to the relaxed surface plane defined by O_c in phosphate groups and a second layer of adsorbed water is found another 1.6 Å above the first layer. In Park's high-resolution X-ray reflectivity study on the structure of the Fluroapatite (1000)-water interface, a 2.65 Å height was found for the first layer, and 1.54 Å for the second layer [41]. As earlier mentioned, the polarity of the (0001) direction is stronger than that of the (1000) direction

[34]. This will explain the shorter water-HAP interlayer distance on the (0001) surface. Meanwhile, the water-water distancein in this work, 1.6 Å, is substantially less than the mean van der Waals diameter of water, 2.82 Å [42], which suggests a certain orientational configuration of the first layer water molecules, which is observed here. In this periodic slab model, there are roughly 5 H_2O molecules on per unit-cell area ($A_{uc} = 76.85$ Å^2) in the first layer of water, which is comparable to Park's result that the derived number of H_2O molecules is 3.5 per unit-cell area ($A_{uc} = 64.9$ Å^2) on the (1000) surface [41].

DFT surface relaxation results show that during the hydration process: (1) no H_2O dissociation is detected, (2) some O ions in surface phosphate groups are protonated by association with water, and (3) the surface (OH) group in the Hydroxyl channel remains immune to the H_2O molecules. Some literature suggests the formation of strong bonds between phosphate oxygen atoms and the hydrogen atoms of water [14]; however, this study does not support this idea, as there are no significant P-O bond length changes found upon forming of the P-O…H bonds. In an acidic medium, the result would probably be quite different. At the current stage of neutral H_2O adsorption, decomposition of the phosphate groups is not predicted. The conclusion that the Hydroxyl channel is immune to the H_2O overlayer agrees with Zahn and Hochrein's molecular dynamics study [14]. They suggest that the decomposition of the embedding Ca(II) triangles may be expected to be a prerequisite of such a process; Ca deficiency would thus be an important factor. Considering Ca-O bonds forming at low H_2O coverage, it is possible that the introduction of some basic groups may help to reduce the repulsion from Ca(II) ions which are at the

edge of the hydroxyl channel, so to facilitate the interaction of (OH) groups with adsorbates.

Zn substitution and occupation on Ca(I) and Ca(II) sites were also studied. The energetics results show that ion substitution is not favored, but Zn occupation on Ca vacancy sites is highly probable. The occupation energy differences for both metal sites are 0.88 eV for the unhydrated surface and 0.21 eV for the hydrated surface, with M(II) site favored in each case. The slab structure change is distinguished by an obvious shrinkage of the M(I) polyhedron and a shift of metal ion from original M(II) site toward the hydroxyl group. This difference in occupation mechanism is considered to be the main reason for the site preference. So the spatial constraint is suggested to be the more probable factor in the substitution mechanism than ionic radius and electronegativity of cations.

REFERENCES

Chapter 1

[1] Cox P.A., *Transition Metal Oxides. An Introduction to their Electronic Structure and Properties* (Oxford: Clarendon) **1992**.

[2] Hashimoto T., Yoki T., Sakka S., *Journal of the Ceramic Society of Japan* **1993**, *101*, 64.

[3] Weiss W., Schlogl R., *Topics in Catalysis* **2000**, *13*, 75.

[4] Johnson D.A., *Some Thermodynamic Aspects of Inorganic Chemistry* (Cambridge: Cambridge University Press) **1982**.

[5] Sorensen O.T., *Non-stoichiometric Oxides* (New York: Academic), **1981**.

[6] Hamnett A., Goodenough J.B., *Binary transition metal oxides Physics of Non-tetrahedrally Bonded, Compounds ed O Madelung, Landolt-B¨ornstein, New Series III, vol 17* (Berlin: Springer) **1984**.

[7] Owen J.F., Teegarden K.J., Shanks H.R., *Physics Review B* **1978**, *18*, 3827.

[8] Malinowski St., Szczepanska S., Bielanski A., Sloczynski J., *Journal of Catalysis* **1965**, *4*, 324.

[9] Miyamoto A., Yamazaki Y., Inomata M., Murakami Y., *Chemistry Letters* 1978, *12*, 1355.

[10] Schulthess C.P., Huang C.P., *Soil Science Society of America Journal* **1991**, *55*, 34.

[11] Mielczarski J.A., Atenas G.M., Mielczarski E., *Applied Catalysis B-Environmental* **2005**, *56*, 289.

[12] Henrich V.E., Cox P.A., *the Surface Science of Metal Oxides* **1994**.

[13] Papakondylis A., Sautet P., *Journal of Physical Chemistry* **1996**, *100*, 10681.

[14] Ji W.J., Chen Y., Shen S.K., Li S.B., Wang H.L., *Applied Surface Science* **1996**, *99*, 151.

[15] Vurens G.H., Salmeron M., Somorjai G.A., *Progress in Surface Science* **1989**, *32*, 333.

[16] Beitel G., Markert K., Wiechers J., Hrbek J., Behm R.J., *Adsorption on Ordered Surfaces of Ionic Solids and Thin Films* (Springer Series in Surface Sciences, vol. *33*) (ed) Freund H-J. and Umbach E. (Heidelberg: Springer), **1993**.

[17] Freund, H.J., Kuhlenbeck H., Staemmler V., *Reports on Progress in Physics* **1996**, *59*, 283.

[18] Liu L., *Ph.D. dissertation*, Northwestern University **2005**.

[19] Wandelt K., *Surface Science Reports* **1982**, *2*, 1.

[20] Antolin s., Nagelberg A.S., Creber D.K., *Journal of the America Ceramic Society* **1992**, *75*, 447.

[21] Fiermans L., Arijs E., Vennik J., Maenhout-Van Der Vorst W., *Surface Science* **1973**, *39*, 357.

[22] Hopkins B.J., Watts G.D., *Surface Science* **1974**, *44*, 237.

[23] Parp H., *Berichte Der Bunsen-Gesellschaft-Physical Chemistry Chemical Physics* **1982**, *86*, 555.

[24] Bertrand P., Delannay F., Streydio J.M., *Journal of Physics E-Scientific Instruments* **1977**, *10*, 403.

[25] Hochella M. F. Jr., *Review in Mineralogy* **1990**, *23*, 87.

[26] Johnsson P. A., Eggleston C. M. and Hochella M. F. Jr., *American Mineralogist* **1991**, *76*, 1442.

[27] Condon N.G., Leibsle F.M., Lennie A.R., Murray P.W., Parker T.M., Vaughan D.J., Thornton G., *Surface Science* **1998**, *397*, 278.

[28] Lad R.J., Henrich V.E., *Surface Science* **1988**, *193*, 81.

[29] Weiss W., Barbieri A., van Hove M.A., Somorjai G.A., *Physics Review Letters* **1993**, *71*, 1848.

[30] Barbieri A., Weiss W., van Hove M.A., Somorjai G.A., *Surface Science* **1994**, *302*, 259.

[31] Hind A. A., and Vicki H. G., Surface Science Reports **2003**, *52*, 63.

[32] Szabo A. and Ostlund N.S., *Modern Quantum Chemistry: Introduction to Advanced Electronic Structure Theory,* Dover Publications, New Ed edition, **1996**.

[33] Dronskowski R., Computational Chemistry of Solid State M*aterials*, Wiley-VCH, **2005**.

[34] Jensen F., *Introduction to Computational Chemistry* John Wiley & Sons, **1999.**

[35] Benjamin I., *Journal of Chemical Physics* **1992**, *97*, 1432.

[36] Lowdin P.O., *Physical Review* **1955**, *97*, 1490.

[37] Mclachlan A.D., Ball M.A., *Review of Modern Physics* **1964**, *36*, 844.

[38] Born M., Oppenheimer R., *Annalen der Physik* **1927**, *84*, 457.

[39] Slater, J.C., Frank N.H., *Introduction to Theoretical Physics* New York: McGraw-Hill, **1933**.

[40] Ebner C., Saam W.F., Stroud D., *Physical Review A* **1976**, *14*, 2264.

[41] Ying S.C., Smith J.R., Kohn W., *Physical Review B* **1975**, *11*, 1483.

[42] Perdew J.P., Mcmullen E.R., Zunger A., *Physical Review A* **1981**, *23*, 2785.

[43] Boguta J., Rafelski J., *Physics Letters B* **1977**, *71*, 22.

[44] Hohenberg P., Kohn W., *Physics Review* **1964**, *136*, B864.

[45] Kohn W., Sham L.J., *Physics Review* **1965**, *140*, A1133.

[46] Von Barth U., Hedin L., *Journal of Physical Chemistry* **1972**, *5*, 1629.

[47] Pant M.M., Rajagopal A.K., *Solid State Communication* **1972,** *5*, 1157.

[48] Gunnarson O., Lundqvist B.I., *Physics Review B* **1976**, *13*, 4274.

[49] Langreth D.C., Perdew J.P., *Physics Review B* **1980**, *21*, 5469.

[50] Langreth D.C., Mehl M.J., *Physics Review B* **1983**, *28*, 1809.

[51] Langreth D.C., Mehl M.J., *Physics Review B* **1983**, *29*, 2310.

[52] Robert G. Parr and Weitao Yang. *Density-Functional Theory of Atoms and Molecules*. Oxford Science Publications, **1989**.

[53] Stoll H., Pavlidou C.M.E., Preuss H., *Theoretica Chimica Acta* **1978**, *49*, 143.

[54] Perdew J.P., Kurth S., Zupan A., Blaha P., *Physics Review Letter* **1999**, *82*, 2544.

[55] Anisimov V.I., Zaanen J., Andersen O.K., *Physics Review B* **1991**, *44*, 943.

[56] Kresse G., Furthmuller J., *Computational Materials Science* **1996**, *6*, 15.

[57] Kresse G., Furthmuller J., *Physics Review B*, **1996**, *54*, 11169.

[58] Becke A.D*., Journal of Chemical Physics **1993***, 98*, 1372.

[59] Roundy D., *Presentation: Density Functional Theory, The plane wave pseudopotential method* October 10, **2005**.

[60] Friedrich C., *Presentation: Introduction to Density Functional Theory* (*and related stuff*).

[61] Kresse G., Furthmuller J., *VASP the guide*, http://cms.mpi.univie.ac.at/vasp/vasp/vasp.html.

[62] Vanderbilt D., *Physics Review B* **1990**, *41*, 7892.

[63] Kress G., Hafner J., *Physics Review B* **1993**, *47*, 558.

[64] Baerends E.J., Ellis D.E., Ros P., *Chemical Physics* **1973**, *2*, 41.

[65] Delley B., Ellis D.E., *Journal of Chemical Physics* **1982**, *76*, 1949.

[66] Vosko S.H., Wilk L., *Physics Review B* **1980**, *22*, 3812.

[67] Tosi M.P., *Solid State Physics, Academic,* New York **1964**.

[68] Ellis D.E., Painter G.S., *Physical Review B* **1970**, *2*, 2887.

[69] Bader R.F.W., *Accounts of Chemical Research* **1985**, *18*, 9.

[70] Cornell *R.M.*, Schwertmann *U.*, *The iron oxides: structure, properties, reactions, occurrences and uses*, *Wiley VCH*, **2003**.

[71] Paidassi J., *Acta Materialia* **1958**, *6*, 184.

[72] Condon N.G., Murray P.W., Leibsle F.M., Thornton G., Lennie A.R., Vaughan D.J., *Surface Science* **1994**, *310*, L609.

[73] Condon N.G., Leibsle F.M., Lennie A.R., Murray P.W., Vaughan D.J., Thornton G., *Physics Review Letters* **1995**, *75*, 1961.

[74] Condon N.G., Leibsle F.M., Lennie A.R., Murray P.W., Parker T.M., Vaughan D.J., Thornton G., *Surface Science* **1998**, *397*, 278.

[75] Barbieri A., Weiss W., Van Hove M.A., Somorjai G.A., *Surface Science* **1994**, *302*, 259.

[76] Spencer N.D., *Journal of Catalysis* **1988**, *109*, 187.

[77] Kasztelan S., Moffat J.B., *Journal of Catalysis* **1987**, *106*, 512.

[78] Smith M.R., Zhang L., Driscoll S.A., Ozkan U.S., *Catalysis Letters* **1993**, *19*, 1.

[79] Kurtz R.L., Henrich V.E., *Physics Review B* **1987**, *36*, 3413.

[80] Toledano D.S., Dufresne E.R., Henrich V.E., *the Journal of Vacuum Science and Technology A* **1998**, *16*, 1050.

[81] Weiss W., Ranke W., *Progress in Surface Science* **2002**, *70*, 1.

[82] Toledano D.S., Henrich V.E., *Journal of Physical Chemistry B* **2001**, *105*, 3872.

[83] Huang W.X., Ranke W., Scholgl R., *Journal of Physical Chemistry B* **2005**, *109*, 9202.

[84] Rim K.T., Muller T., Fitts J.P., Adib K., Camillone N. III, Osgood R.M., Batista E.R., Friesner R.A., Joyce S.A., Flynn G.W., *Journal of Physical Chemistry B* **2004**, *108*, 16753.

[85] Lemire C., Meyer R., Henrich V.E., Shaikhutdinov Sh., Freund H.-J., *Surface Science* **2004**, *572*, 103.

[86] Rohrbach A., Hafner J., Kresse G., *Physics Review B* **2004**, *70*, 125426.

[87] Wang X.G., Weiss W., Shaikhutdinov S.K., Ritter M., Petersen M., Wagner F., Schlogl R., Scheffler M., *Physical Review Letters* **1998**, *81*, 1038.

[88] Catti M., Valerio G., Dovesi R., *Physics Review B* **1995**, *51*, 7441.

[89] Guo Q., McBreen P.H., Moller P.J., *Surface Science* **1999**, *423*, 19.

[90] Jeon B.H., Dempsey B.A., Burgos W.D., Royer R.A., *Water Research* **2003**, *37*, 4135.

[91] Narasaraju T.S.B, Phebe D.E., *Journal of Materials Science* **1996**, *31*, 1.

[92] Reyes-Gasga J.G., Garcia R., Vargas-Ulloa L., *Philosophical Magazine A* **1997**, *75*, 1023.

[93] Ratner B.D., Hoffman A.S., Schoen F.J., Lemons J.E., *Biomaterials Science, Academic Press,* San Diego, CA, **1996**.

[94] Hench L.L., *Journal of American Ceramic Society* **1998**, *81*, 1705.

[95] Suzuki T., Hatsushika T., Hauakawa Y., *Journal of Chemical Society, Faraday Transactions 1* **1981**, *77*, 1059.

[96] Yasukawa A., Kamiuchi K., Yokoyama T., Ishikawa T., *Journal of Solid State Chemistry* **2002**, *163*, 27.

[97] Mkhonta D., de Leeuw N.H., *Journal of Materials Chemistry* **2002**, *12*, 2633.

[98] Lower S.K., Maurice P.A., Traina S.J., *Geochimica et Cosmochimica Acta* **1998**, *63*, 1773.

[99] Meis C., Gale J.D., Boer L., Carpean J., Gosset D., *Journal of Physical Chemistry A* **2000**, *104*, 5380.

[100] Nicolopolus S., Conzalez-Calbet J.M., Alonso M.P., Gutierrez-rios M.T., Frutos M.I., Vallet-Regi M., *Journal of solid State Chemistry* **1999**, *116*, 265.

[101] Par J.B., *Biomaterials Science and Engineering, Plenum Press,* New York, **1984**.

[102] Yubao L. Klein C.P.A.T., De Wijn J., Van de Meer S., Groot K., *Journal of Materials Science: Materials in Medicine* **1994**, *5*, 263.

[103] Peeters A., de Maeyer E.A.P., Van Alenoy C., Verbeeck R.M.H., *Journal of Physical Chemistry B* **1997**, *101*, 3995.

[104] Ferro-Flores G., Ramirez F.de M., Tendilla J.I., Pimentel-Gonzalez G., Murphy C.A., Melendez-Alafort L., Ascencio J.A., Croyft Y., *Bioconjugated Materials* **1999**, *10*, 726.

[105] Ascencio J.A., Perez-Marin L., Otazo-Sanchez E., Castro M., Contreras-Pulido D., Cisniega G.A., *Afinidad* **2001**, *43*, 2479.

[106] Steward J.J.P., *Journal of Computational Chemistry* **1989**, *10*, 209.

[107] Shah R., Gale J.D., Payne M.C., *Journal of Physical Chemistry B* **1997**, *101*, 4787.

[108] Zhu W., Wu P., *Chemical Physics Letters* **2004**, *296*, 38.

[109] Zahn D., Hochrein O., *Zeitscheift Fur Anorganische Und Allgemeine Chemie* **2006**, *632*, 79.

[110] De Leeuw N.H., *Chemical Communications* **2001**, *17*, 1646.

[111] Calderin L., Stott M.J., *Physical Review B* **2003**, *67*, 134106.

[112] Peroos S., Du Z., De Leeuw N.H., *Biomaterials* **2006**, *27*, 2150.

[113] Zahn D., Hochrein O., *Physical Chemistry Chemical Physics*, **2003**, *5*, 4004.

Chapter 2

[1] Peng X.D., Viswanathan R., Smudde G.H Jr., Stair P.C., *Review of Scientific Instruments* **1992**, *63*, 3930.

[2] Street S.C., Liu G., Goodman D.W., *Surface Science* **1997**, *385*, L971.

[3] Tamura H., Zhou H., Hirano Y., Takami S., Kubo M., Belosludov R.V., Miyamoto A., Imamura A., Gamo M.N., Ando T., *Physics Review B* **2000**, *62*, 16995.

[4] Keudell A.V., Schwarz-Selinger T., Jacob W., *Journal of Applied Physics* **2001**, *89*, 2979.

[5] Campbell K.D., Zhang H., Lunsford J.H., *Journal of Physical Chemistry* **1988**, *92*, 750.

[6] Tong Y., Lunsford J.H., *Journal of American Chemical Society* **1991**, *113*, 4741.

[7] Xu M.T., Ballinger T.H., Lunsford J.H., *Journal of Physical Chemistry* **1995**, *99*, 14494.

[8] Tjandra S., Zaera F., *Langmuir* **1992**, *8*, 2090.

[9] Zaera F., *Surface Science* **1992**, *262*, 335.

[10] Pak S., Smith C.E., Rosynek M.P., Lunsford J.H., *Journal of Catalysis* **1997**, *165*, 73.

[11] Michaelides A., Hu P., *Surface Science* **1999**, *437*, 362.

[12] Walter E.J., Rappe A.M., *Surface Science* **2004**, *549*, 265.

[13] Todnem K., Borve K.J., Nygren M., Surface Science **1999**, *421*, 296.

[14] Freitag J., Staemmler V., *Journal of Electron Spectroscopy and Related Phenomena* **1994**, *69*, 99.

[15] Hoeft J.-T., Kittel M., Polcik M., Bao S., Toomes R.L., Kang J.-H, Woodruff D.P., Pascal M., Lamont C.L.A., *Physics Review Letters* **2001**, *87*, 086101.

[16] Rohrbach A., Hafner J., Kresse G., *Physics Review B* **2004**, *69*, 075413.

[17] Rohrbach A., Hafner J., *Physics Review B* **2005**, *71*, 045405.

[18] Rodriguez J.A., Maiti A., *Journal of Physical Chemistry B* **2000**, *104*, 3630.

[19] Valentin C.D., Pacchioni G., Bredow T., Dominguez-Arize D., Illas F., *Journal of Chemical Physics* **2002**, *117*, 2299.

[20] Liu L., *Ph.D. thesis,* Department of Chemistry, Northwestern University **2005**.

[21] Wang Y., Perdew J.P., *Physical Review B* **1991**, *44*, 13298.

[22] Perdew J.P., Chevary J.A., Vosko S.H., Jackson K.A., Pederson M.R., Singh D.J., Fiolhais C., *Physical Review B* **1992**, *46*, 6671.

[23] Mermin N.D., *Physics Review* **1965**, *137*, A1441.

[24] Blochl P.E., Jepsen O., Andersen O.K., preprint, **1993**.

[25] Kresse G., Furthmuller J., *VASP the guide*, http://cms.mpi.univie.ac.at/vasp/vasp/vasp.html.

[26] Rohrbach A., Hafner J., Kresse G., *Physics Review B* **2004**, *70*, 125426.

[27] Condon N.G., Leibsle F.M., Lennie A.R., Murray P.W., Vaughan D.J., Thornton G., *Physics Review Letters* **1995**, *75*, 1961.

[28] Wang X.G., Weiss W., Shaikutdinov S.K., Ritter M., Petersen M., Wagner F., Schlogl R., Scheffler M., *Physics Review Letters* **1998**, *81*, 1038.

[29] Finger L.W., Hazen R.M., *Journal of Applied Physics* **1980**, *51*, 5362.

[30] Wolfgang B., Schwieger H., Wimmer E., *Physics Review B* **2004**, *69*, 195409.

[31] Addiego W.P., Estrada C.A., Godman D.W., Rosynek M.P., *Journal of Catalysis* **1994**, *146*, 407.

[32] Ma X.Y., Liu L., Jin J.J., Stair P.C., Ellis D.E., *Surface Science* **2006**, *600*, 2874.

[33] Stair P.C, *private communications*.

Chapter 3

[1] Brown G.E., Henrich V.E. Jr, Casey W.H., Clark D.L., Eggeston C, Felmy A., Goodman D.W., Gratzel M., Maciel G., McCarthy M.I., Nealson K.H., Sverjensky D.A., Toney M.F., Zachara J.M., *Chemical Review* **1999**, *99*, 77.

[2] Fujishima A., Honda K., *Nature* **1972**, *238*, 37.

[3] Bargar J.R., Trainor T.P., Fitts J.P., Chambers S.A., Brown G.E. Jr, *Langmuir* **2004**, *20*, 1667.

[4] Hass K.C., Schneider W.F., Curioni A., Andreoni W., *Journal of Physical Chemistry B* **2000**, *104*, 5527.

[5] Goniakowski J., Gillan M.J., *Surface Science* **1996**, *350*, 145.

[6] Scameborn C.A., Harrison N.M., Mccarthy M.I., *Journal of Chemical Physics* **1994,** *101,* 1547.

[7] Ma X.Y., Liu L., Jin J.J., Stair P.C., Ellis D.E., *Surface Science* **2006**, *600*, 2874.

[8] Lemire C., Bertarione S., Zecchina A., Scarano D., Chaka A., Shaikhutdinov S., Freund H.-J., *Physics Review Letters* **2005**, *94*, 166101.

[9] Bergermayer W., Schweiger H., Wimmer E., *Physics Review B* **2004**, *69*, 195409.

[10] Rohrbach A., Hafner J., Kresse G., *Physics Review B* **2004**, *70*, 125426.

[11] Wasserman E., Rustad J.R., Felmy A.R., Hay B.P., Halley J.W., *Surface Science* **1997**, *385*, 217.

[12] Jones F., Rohl A.L., Farrow J.B., Bronswijk W.V., *Physical Chemistry Chemical Physics* **2000**, *2*, 3209.

[13] Kresse G., Furthmuller J., *VASP the guide*, http://cms.mpi.univie.ac.at/vasp/vasp/vasp.html.

[14] Rollmann G., Pohrbach A., Entel P., Hafner J., *Physics Review B* **2004**, *69*, 165107.

[15] Bader R.F.W., *Accounts of Chemical Research* **1985**, *18*, 9.

[16] Yin S.X., Ma X.Y., Ellis D.E., *Surface Science* **2007**, *601*, 2426.

[17] Modig K., Pfrommer B.G., Halle B., *Physical Review Letters* **2003**, *90*, 075502.

[18] Becker U., Hochella M.F., Apra E. Jr., *American Mineralogist* **1996**, *81*, 1301.

[19] Jin J.J., *Ph.D. thesis*, Northwestern University, **2007,** unpublished.

[20] Rohrbach A., Hafner J., *Physics Review B* **2005**, *71*, 045405.

[21] Liu P., Kendelwicz T., Brown G.E. Jr, Nelson E.J., Chambers S.A., *Surface Science* **1998**, *417*, 53.

[22] Henrich V.E., Cox P.A., *The Surface of Metal Oxides* University Press, Cambridge, **1994**.

[23] Bond G.C., Tahir S.F., *Applied Catalysis* **1991**, *71*, 1.

[24] Wachs I.E., *Catalysis Today* **1996**, *27*, 437.

[25] Surnev S., Ramsey M.G., Netzer F.P., *Progress in Surface Science* **2003**, *73*, 117.

[26] Biener J., Bäumer M., Wang J., Madix R.J., *Surface Science* **2000**, *450*, 12.

[27] Biener J., Bäumer M., Madix R.J., Liu P., Nelson E., Kendelewisz T., Brown G. Jr., *Surface Science* **2000**, *449*, 50.

[28] Wang X.G., Weiss W., Shaikhutdinov S.K., Ritter M., Petersen M., Wagner F., Schlögl R., Scheffler M., *Physics Review Letters* **1998**, *81*, 1038.

[29] Greene M.E., Chiaramonti A.N., Christensen S.T., Cao L., Bedzyk M.J., Hersam M.C., *Advanced Material* **2005**, *17*, 1765.

[30] Kim C.-Y., Escuadro A.A., Stair P.C., Bedzyk M.J., *Journal of Physical Chemistry C* **2007,** *111,* 1874.

[31] Jin J.J., Ma X.Y., Kim C.-Y., Ellis D.E., Bedzyk M.J., *Surface Science* (in press)

Chapter 4

[1] Narasaraju T.S.B, Phebe D.E., *Journal of Materials Science* **1996**, *31*, 1.

[2] Reyes-Gasga J., Garcia R., Vargas-Ulloa L., *Philosophical Magazine A* **1997**, *75*, 1023.

[3] Ratner B.D., Hoffman A.S., Schoen F.J., Lemons J.E., *Biomaterials Science, Academic Press* San Diego, CA, **1996**.

[4] Hench L.L., *Journal of American Ceramic Society* **1998**, *81*, 1705.

[5] Suzuki T., Hatsushika T., Hauakawa Y., *Journal of the Chemical Society, Faraday Transactions 1* **1981**, *77*, 1059.

[6] Yasukawa A., Kamiuchi K., Yokoyama T., Ishikawa T., *Journal of Solid State Chemistry,* **2002**, *163,* 27.

[7] Mkhonto D., de Leeuw N.H., *Journal of Materials Chemistry* **2002**, *12*, 2633.

[8] Lower S.K., Maurice P.A., Traina S.J., *Geochim et Cosmochim Acta* **1998**, *63*, 1773.

[9] Meis C., Gale J.D., Boyer L., Carpena J., Gosset D., *Journal of Physical Chemistry A* **2000**, *104*, 5380.

[10] Nicolopoulos S., Gonzalez-Calbet J.M., Alonso M.P., Gutierrez-rios M.T., de Frutos M.I., Vallet-Regi M., *Journal of solid State Chemistry* **1999**, *116*, 265.

[11] Par J.B., *Biomaterials Science and Engineering, Plenum Press,* New York, **1984**.

[12] Yubao L., Klein C.P.A.T., de Wijn J., Van de Meer S., de Groot K., *Journal of Materials Science Materials in Medicine* **1994**, *5*, 263.

[13] Peeters A., de Maeyer E.A.P., Van Alsenoy C., Verbeeck R.M.H., *Journal of Physical Chemistry B* **1997**, *101*, 3995.

[14] Zahn D., Hochrein O., *Physical Chemistry Chemical Physics* **2003**, *5*, 4004.

[15] Stewart J.J.P., *Journal of Computational Chemistry* **1989**, *10*, 209.

[16] Kohn W., Sham L.J.*, Physics Review* **1965**, *140*, A1133.

[17] Shah R., Gale J.D., Payne M.C., *Journal of Physical Chemistry B* **1997**, *101*, 4787.

[18] Zhu W., Wu P., *Chemical Physics Letters* **2004**, *396*, 38.

[19] Zahn D., Hochrein O., *Zeitschrift fur Anorganische und Allgemeine Chemie* **2006**, *632*, 79.

[20] De Leeuw N.H., *Chemical Communications* **2001**, 1646.

[21] Lazic S., Vukovic Z., *Journal of Radioanalytical and Nuclear Chemistry, Articles* **1991**, *149*, 161.

[22] Cazalbou S., Eichert D., Ranz X., Drouet C., Combes C., Harmand M.F., Rey C., *Journal of Materials Science Materials in Medicine* **2005**, *16*, 405.

[23] Calderin L., Stott M.J., *Physical Review B* **2003**, *67*, 134106.

[24] Peroos S., Du Z., De Leeuw N.H., *Biomaterials* **2006**, *27*, 2150.

[25] Windisch W., *Trace Elements and Electrolytes* **2001**, *18*, 122.

[26] Kohsuke M., Yohei M., Takayoshi H., Tomoo M., Kohki E., Kiyotomi K., *Chemical Communications* **2005**, 3331.

[27] Terra J., Jiang M., Ellis D.E., *Philosophical Magazine A* **2002**, *82*, 2357.

[28] Kresse G., Furthmuller J., *VASP the guide*, http://cms.mpi.univie.ac.at/vasp/vasp/vasp.html.

[29] Kresse G., Furthmuller J., *Physical Review B* **1996**, *54,* 11169.

[30] Blochl P.E., *Physical Review B* **1994**, *50,* 17953.

[31] Kresse G., Joubert D., *Physical Review B* **1999**, *59,* 1758.

[32] Monkhorst H., Pack J.D., *Physical Review B* **1976**, *13,* 5188.

[33] Posner A.S., Perloff A., Diorio A.F., *Acta Crystallographica* **1958**, *11*, 308.

[34] Urusov V.S., Khudolozhin V.O., *Geochemistry International* 1**975**, *11*, 1048.

[35] Pan H.H., Tao J.H., Wu T., Tang R.K., *Chinese Journal of Inorganic Chemistry* **2006**, *8*, 1392.

[36] Posner A.S., *Journal of Biomedical Materials Research* **1985**, *19*, 241.

[37] De Leeuw N.H., Bowe J.R., Rabone J.A.L., *Faraday Discuss* **2007**, *134*, 195.

[38] Zhu K., Yanagisawa K., Shimanouchi R., Onda A., Kajiyoshi K., *Journal of the*

European Ceramic Society **2006**, *26*, 509.

[39] Ellis D.E., Terra J., 2007, unpublished.

[40] Badraoui B., Thouvenot R., Debbabi M., *Comptes Rendus de L Academie Des Sciences Serie II Fascicule C-Chimie* **2000**, *3*, 107.

[41] Park C., Fenter P., Zhang Z., Cheng L., Sturchio N.C., *American Mineralogist* **2004**, *89*, 1647.

[42] Franks F., *Water: A matrix of life, 2nd Edition* Royal Society of Chemistry, Cambridge, **2000**.

PUBLICATIONS

1. Ma X.Y., Ellis D.E., *Initial stages of hydration and Zn occupation on Hydroxyapatite (0001) surfaces*, (to be submitted).

2. Jin J.J., Ma X.Y., Kim C.-Y., Ellis D.E., Bedzyk M.J., *Adsorption of V on a Hematite (0001) surface and its oxidation: monolayer coverage*, (submitted).

3. Jin J.J., Ma X.Y., Kim C.-Y., Ellis D.E., Bedzyk M.J., *Adsorption of V on a Hematite (0001) surface and its oxidation: submonolayer coverage*, (in press).

4. Yin S.X., Ma X.Y., Ellis D.E., *Initial stages of H_2O adsorption and hydroxylation of Fe-terminated α-Fe_2O_3 (0001) surface, Surface Science* **2007**, *601*, 2426.

5. Ma X.Y., Liu L., Jin J.J., Stair P.C., Ellis D.E., *Experimental and theoretical studies of adsorption of $CH_3\bullet$ on α-Fe_2O_3 (0001) surfaces, Surface Science* **2006**, *600*, 2874.